Title
Controlling the Reactivity of Silicate and Aluminate Glasses in Aqueous Alkaline Environments

Author
Oey, Tandre Jean-Paul

Publication Date
2019

Peer reviewed|Thesis/dissertation

UNIVERSITY OF CALIFORNIA

Los Angeles

Controlling the Reactivity of Silicate and Aluminate Glasses in Aqueous Alkaline Environments

A dissertation submitted in partial satisfaction of the requirements for the degree Doctor of Philosophy in Civil Engineering

by

Tandre Oey

2019

ABSTRACT OF THE DISSERTATION

Controlling the Reactivity
of Silicate and Aluminate Glasses
in Aqueous Alkaline Environments

by

Tandre Oey
Doctor of Philosophy in Civil Engineering
University of California, Los Angeles, 2019
Professor Gaurav Sant, Chair

Production of cement, the binder component of concrete, accounts for an estimated 9% of global CO_2 emissions. To improve sustainability of cement and concrete use, two strategies have emerged: (1) to consume less cement by partially replacing it with supplementary cementing materials (SCMs), or (2) to consume less concrete by improving its durability (e.g., as hindered by reactive aggregates). Many such SCMs and reactive aggregates are well-represented as amorphous aluminosilicates. The current research investigates simplified metrics that reflect the composition and structure of these aluminosilicates while enabling prediction of their aqueous reactivity in alkaline environments, and the associated impact on cement paste and mortar properties. New means to control aluminosilicate reactivity are developed, alongside improved understandings that will aid in the future use of data-driven learning tools to study and solve similar material problems.

The dissertation of Tandre Oey is approved.

Richard B. Kaner

Sanjay K. Mohanty

Mathieu Bauchy

Jeffery W. Bullard

Gaurav Sant, Committee Chair

University of California, Los Angeles

2019

This work is dedicated to my mother, Pat Oey.

Table of Contents

List of Figures

Here and throughout the paper, the relative standard deviation in density and T_g is approximately 1 % and 5 %, respectively, based on three measurements of different samples of the same fly ash. In (a), (c), and all other plots showing a trend line, the lines were produced by ordinary linear regression merely to indicate the approximately linear trends. The equation for the lines shown in (a) and (c) are of the form:

$$\rho = 0.186 \cdot N_r + 2.344$$

and

$$T_g = -39.017 \cdot N_r + 902.339$$

Figure 5: The CaO/Al_2O_3 ratio (mole basis), R ("compensation ratio"), as a function of: **(a)** deviation from the T_g correlation of Figure 4(c), and **(b)** mass fraction of glassy phases present in each fly ash.

Figure 6: Representative micrographs for Class F fly ash F3 acquired using scanning electron microscopy (SEM) showing: **(a)** backscatter image, **(b)** X-ray dispersive spectroscopy element maps with color coded images overlaid where Ca is shown as red, Si as green, and Al as blue, and **(c)** the multispectral image segmentation mask, with the color codes shown below. Scale bars, indicated by white rectangles in the bottom right corner of each image, are 40 microns.

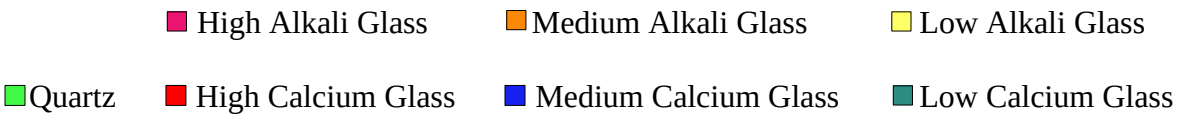

Figure 7: Representative ternary diagrams showing: **(a)** manually selected clusters from the elemental maps and **(b)** clusters identified by the automated GCD-kit algorithm. The red symbols

indicate calcium-rich phases, green indicates silicon-rich phases, and blue indicates aluminum-rich phases. **(c)** A ternary diagram showing compositional groupings of the glass phases across all the fly ashes, as defined from multispectral clustering.

Figure 8: The composition and abundance of fly ash glasses for **(a)** calcium aluminosilicate (CAS) glasses and **(b)** alkali aluminosilicate (AAS) glasses, as a percentage of total amorphous material, and **(c)** a comparison between the simplified network ratio calculated using the EDS composition segmented groupings and calculated from the XRF-XRD data. The relative standard deviation in glass contents for CAS glasses and AAS glasses are on the order of 8 % and 6 % respectively, based on analyses of at least three different SEM fields of view at the same magnification.

Figure 9: Representative isothermal calorimetry profiles for fly ash-cement blends for: **(a)** fly ash C2 and **(b)** fly ash F3. **(c)** The heat release rate at the main hydration peak as a function of the area multiplier (AM). The maximum range in the data for six replicates of plain Type I/II portland cement, at any time between 1 h and 72 h, was approximately ± 2 % of the signal.

Figure 10: (a) The BET surface area of the different fly ashes, listed from left to right in order of decreasing CaO content, and **(b)** the BET surface areas as a function of the LOI of the fly ashes. The relative standard deviation in surface area values by BET is approximately 5 % based on three replicate measurements of the same powder sample, and the uncertainty in LOI is ± 0.1%. The equation of the line in (b) is of the form:

$$SSA_{BET} = 0.827 \cdot LOI + 0.485$$

Figure 11: (a) Representative compressive strength-heat release correlations for a Class F (F1) and a Class C (C1) fly ash (± 10% uncertainty in compressive strength values based on measurement of three replicate samples); **(b)** the 7-d heat release as function of the network ratio (relative standard deviation is 2 % based on six replicates); and **(c)** The slope of the strength-heat correlation plot as a function of the network ratio (relative standard deviation based on three replicates is approximately 10.2 %). The equations in (b) and (c) are of the form:

$$Q_{7\ days} = 98.227 \cdot N_r + 360.050$$

and

$$S = -0.014 \cdot N_r + 0.070$$

Figure 12: The dissolution rates of the seven fly ashes as a function of: **(a)** solution pH, and **(b, c)** the number of constraints per atom (n_c, unitless) calculated by MD simulations. For consistent comparison between solids of different compositions, the dissolution rates are expressed as moles of O_2 dissolved per m^2 of surface area per second. The data in (b, c) is fitted using exponential functions. The color of datapoints in (b) correspond to the legend presented in (a) to indicate which fly ash each point represents, while the symbol shape corresponds to the solution pH, with squares, circles, diamonds, and crosses representing pH 10, 12, 13, and 14 respectively. The data in (c) includes dissolution rates for silica and quartz, as well as glassy equivalents of albite, jadeite, nepheline, and sodium silicate glass (see [23,101,103]). The exponential functions represent an Arrhenius-like expression of the form: $K = K_0 \exp(-n_c E_0 / k_B T)$, where: K is the dissolution rate in μmol/m^2•s, K_0 is the intrinsic dissolution rate constant in μmol/m^2•s, E_0 is the

energy required to break a unit atomic constraint (E_0 = 23.9 kJ/mole in Figure 1c), k_B is Boltzmann's constant in kJ/mol•K, and T is the thermodynamic temperature in degrees K.

Figure 13: (a) The amount of boron released from two representative alkaline earth aluminoborate glasses as a function of time. **(b)** The evolution of the instantaneous dissolution rate (i.e., estimated from the extent of boron release rate between two consecutive time points from Figure 13a) normalized by the *initial* dissolution rate. The highest uncertainty in the measured boron release is on the order of 3% based on triplicate measurements.

Figure 14: (a) The *initial* dissolution rate of the aluminoborate glasses as a function of the ionic radius of the network-modifying species. **(b)** The degree of congruence (i.e., with respect to the leaching rate of boron atoms; DOC) of aluminum atoms and alkaline earth network-modifying elements. The solid line defines congruent dissolution with respect to boron release rates. **(c)** The degree of congruence (i.e., with respect to the leaching rate of boron) of the alkaline earth network-modifying elements as a function of the average coordination number of aluminum species in the glass structure.

Figure 15: (a) The dissolution rate (i.e., boron release rate) of mixed Li-Mg aluminoborate glasses as a function of the molar ratio, Li/(Li+Mg). **(b)** The average coordination number of aluminum atoms as a function of the molar ratio, Li/(Li+Mg).

Figure 16: The dissolution rates of all aluminoborate glass compositions as a function of the number of topological constraints per atom while considering: **(a)** the whole atomic network

(i.e., all atoms including network formers and modifiers), and, **(b)** the aluminoborate skeleton network (i.e., only including the network forming species; Al and B). The data in (b) is fitted by a function of the form $K = K_0 \exp(n_c E_0/RT)$, where K is the boron release rate (initial dissolution rate), K_0 is an intrinsic dissolution rate constant, n_c is the number of constraints, E_0 is the rupture energy (here, E_0 = 6.9 kJ/mol) associated with a single skeletal constraint, R is the gas constant, and T is thermodynamic temperature.

Figure 17: Representative illustrations of: **(a)** a "fast dissolving" lithium aluminoborate glass, **(b)** the "mixed modifier effect" as previously conceived, i.e., with the less mobile Mg modifiers "blocking" release of dissolving elements, and **(c) "**constraint controlled" dissolution wherein the average number of constraints per atom offers an indication of the steric hindrance to element release (dissolution), herein due to the higher coordination number of Al units associated with the Mg modifiers. This clarifies the *indirect* role of modifiers in suppressing dissolution, as a function of induced changes to network topology and their effects on dissolution rate, as described in the text.

Figure 18: Characterization data for each of the six synthetic glasses showing (a) X-ray diffraction patterns, and (b) particle size distributions. Note that a particle size distribution characteristic of a typical fly ash is also shown for comparison.

Figure 19: Two parameters related to glass composition and structure: **(a)** XRD amorphous peak position, and **(b)** glass transition temperature plotted as a function of degree of de-polymerization (i.e. non-bonding oxygens per silicate tetrahedral unit, NBO/T), as well as **(c)** glass transition

temperature as a function of number of topological constraints per network atom (n_c). Each point is labeled with the index number of the corresponding glass as noted in Table 4. Dashed lines shown in parts (a) and (b) are provided to guide the eye, and do not represent physically meaningful correlations.

Figure 20: (a) Representative silicon release profiles of Glass 3 at pH 10, **(b)** a representative illustration of proportionality between "initial" and "steady-state" dissolution rates for all of the glass types at pH 10, and **(c)** an illustration of the relation between the average dissolution reduction factor, i.e., the ratio of "steady-state" to "initial" dissolution rate, and the aluminum content of each glass at each of the three solution pH values studied. Dashed lines in part (b) and (c) are provided to guide the eye for ease of comparison between data series.

Figure 21: (a) "Initial" dissolution rate of each aluminosilicate glass at pH 10 and room temperature, overlaid on previously acquired data from fly ash, [118] demonstrating an exponential dependence on number of topological constraints. **(b)** An illustration of an Arrhenius plot used to determine effective activation of dissolution from rate values determined at 5, 25, and 45° C. **(c)** A representative set of effective activation energies for the dissolution of each aluminosilicate glass at pH 10, compared against the topological prediction. It should be noted that experimental activation energies are similarly low at higher values of solution pH, though with some mild increases due to greater aluminum release (as measured, due to a general increase in dissolution rate of all elements at higher pH), consistent with the finding that Al inhibits silicate dissolution and increases activation energy accordingly.[150,156]

Figure 22: "Initial" dissolution rates plotted as a function of number of constraints for **(a)** dissolution occurring at pH 10 compared between 5, 25, and 45° C, and **(b)** dissolution occurring at 25° C compared between solution pH 10, 12, and 13.

Figure 23: Representative time-dependent profiles illustrating evolution of degree of congruence (DOC, Equation 1) for the dissolution of glass 3 at 25° C, over a range of solution pH values, with respect to **(a)** calcium, and **(b)** aluminum. **(c)** Inverse correlations between DOC for Al and Ca at 25° C for several glass types with varied aluminum content.

Figure 24: The **(a)** measured expansion, and **(b)** volume-fraction-normalized expansion of NBS glass-containing mortar bars at 25°C, for volume fractions, ϕ_a, ranging from 0.15 to 0.55.

Figure 25: (a) The 200 d expansion data, ε_{200}, plotted as a function of NBS glass volume fraction. A linear fit to strain for $\phi_a > \phi^*_a$ is also shown. **(b)** The initial expansion rate of NBS glass mortar bars, $R_{e,i}$, plotted as a function of the NBS glass volume fraction. The linear regressions suggest proportionality between ϕ_a and expansion rate. The data for quartz-substituted systems ($\phi_{a,total}$ = 0.55 consisting of 0.15 NBS glass and 0.40 quartz sand) are shown as solid symbols for comparison (on both plots).

Figure 26: (a) A comparison between the initial expansion rates of cementitious mortar bars over the first 20 days for conditions encompassing: different NBS glass volume fractions (ϕ_a), reaction temperature, and calcium nitrate (CN) dosage. **(b)** A comparison between expansion

profiles for the reference mortar bars and its $Ca(NO_3)_2$ containing counterparts, showing the progressive inhibition of expansion with increasing additive dosage.

Figure 27: (a) Representative silicon release as a function of time and temperature, for the dissolution of NBS glass (Size 3, d_{50} = 15.9 μm) in a pH 12 (10 mmol/L NaOH) solution. **(b)** A compositional line profile acquired using SEM-EDS transverse to the surface of a representative borosilicate glass particle embedded in 14 d mortar bar. It should be noted that the interaction volume associated with the SEM-EDS measurement is on the order of one cubic micron, limiting the use of this technique as applied to altered surface layers.

Figure 28: (a) The dissolution rates of NBS glass (Size 3, d_{50} = 15.9 μm) in a pH 12 (10 mmol/L NaOH) solution dosed with Al, Ca, and Li nitrate salts, as a function of salt concentration. **(b)** A representative Arrhenius plot that is used to estimate the activation energy of NBS glass dissolution. **(c)** The activation energy (E_a, kJ/mol) of NBS glass dissolution in selected solution compositions from 25 °C ≤ T ≤ 45 °C.

Figure 29: (a) The concentration of Ca-species in extracted cementitious pore solution as a function of time for both $Ca(NO_3)_2$-dosed and calcium nitrate free systems, and **(b)** The zeta potential of calcite and NBS-glass particles in contact with pH 12 (10 mmol/L NaOH) solutions containing different concentrations of calcium (and aluminum) nitrate. The shaded gray region shows the zeta potential that is measured under *additive-free* conditions (the width of the gray region shows the standard deviation of replicate measurements).

Figure 30: Representative SEM images of NBS glass particles exposed to pH 12 NaOH solutions for 7 days across varying concentrations of calcium nitrate (CN). The surface coverage of precipitates forming on the NBS-glass surfaces increases dramatically with CN concentration thus implicating the role of surficial barrier formation in dissolution inhibition. The image for 100 mmol/L CN has been republished with permission from.[172]

Figure 31: The results of a representative parameter tuning exercise for the extremely random forest estimators constructed to estimate initial setting time, showing: **(a)** A plateau in estimator performance with increasing number of trees (i.e., in each case using two attributes to determine each partitioning of the input space), and **(b)** A modest optimum of two splits is observed when using 1000 trees.

Figure 32: Representative evaluations of estimator performance shown for the extremely random forest estimators constructed to estimate 3 d compressive strength which highlight **(a)** Attribute importance as determined by an increase in MAPE upon omission of a given input attribute, and **(b)** so-called "learning curves" for the estimator showing the minimum number of input records required to construct an adequate estimator.

Figure 33. The prediction results of an optimized 500-tree extremely random forest regression estimator, shown as **(a)** predicted vs actual strength values with a dashed line of identity provided to guide the eye, and **(b)** the normalized cumulative probability distribution of a prediction by the estimator having a given error. Also shown for comparison are distributions for

a similar estimator applied to prediction of 3 d compressive strength of mortars (this study) and 28 d compressive strength of concretes (Young *et al.*[24]).

Figure 34. **(a)** The distribution of measured compressive strength values from the full dataset, with data that was used as input to train ML estimators, predictions to test ML estimators, and excluded data marked in green, blue, and red, respectively. **(b)** Prediction results of an optimized 500-tree extremely random forest regressor trained on an input set subject to under-sampling (as illustrated in part (a)), shown as predicted vs actual strength values with a dashed line of identity provided to guide the eye.

List of Tables

cements in the full dataset, and italicized entries are reported in at least 50 % of the records in the dataset. Other entries were not consistently reported and were excluded from inputs to ML estimators. All boldfaced and italicized entries listed under “Physical Tests,” with the exception of Blaine Fineness, were utilized as target attributes in this study, and as such were also excluded from inputs to ML estimators. All other entries that were excluded from inputs to ML estimators were verified to be of minimal importance to estimator performance, as outlined in Section 7.3.2.

Table 8: The results of 10-fold cross-validation using the following error metrics: root mean square error (RMSE), coefficient of determination (R^2), and mean absolute percentage error (MAPE). The input attributes were SiO_2 (mass %), Al_2O_3 (mass %), Fe_2O_3 (mass %), CaO (mass %), SO_3 (mass %), and Blaine fineness (m^2/kg), as determined by attribute importance in Section 7.3.2.

Table 9: Results of 10-fold cross-validation for the final machine learning estimators of secondary targets with partial data records, evaluated using the same error metrics given in Table 6. The best-performing estimator (lowest MAPE) is marked in bold. The number of available data points used in each estimator is also reported.

Acknowledgements

I would like to thank my advisor and my dissertation committee for their guidance and support.

I would also like to acknowledge the journals that made publication of my work possible:

- Chapter 2 is a version of: Oey, T.; Timmons, J.; Stutzman, P.; Bullard, J. W.; Balonis, M.; Bauchy, M.; Sant, G. An improved basis for characterizing the suitability of fly ash as a cement replacement agent. *Journal of the American Ceramic Society* **2017**, *100* (10), 4785–4800. DOI: 10.1111/jace.14974.

- Chapter 3 is a version of: Oey, T.; Pignatelli, I.; Yu, Y.; Neithalath, N.; Bullard, J. W.; Bauchy, M.; Sant, G. Topological controls on the dissolution kinetics of glassy aluminosilicates. *Journal of the American Ceramic Society* **2017**, *100* (12), 5521–5527. DOI: 10.1111/jace.15122.

- Chapter 4 is a version of: Oey, T.; Frederiksen, K.; Mascaraque, N.; Youngman, R.; Balonis, M.; Smedskjaer, M.; Bauchy, M.; Sant, G. The role of the network-modifier's field-strength in the chemical durability of aluminoborate glasses. *Journal of Non-Crystalline Solids* **2019**, *505*, 279–285. DOI: 10.1016/j.jnoncrysol.2018.11.019.

- Chapter 5 is a version of: Oey, T.; La Plante, E. C.; Falzone, G.; Yang, K.; Wada, A.; Bauchy, M.; Bullard, J. W.; Sant, G. Environmental sensitivity of the topological model for aluminosilicate glass dissolution. *Prepared for submission to Journal of the American Ceramic Society* (September **2019**).

- Chapter 6 is a version of: Oey, T.; La Plante, E. C.; Falzone, G.; Hsiao, Y-H.; Wada, A.; Monfardini, L.; Bauchy, M.; Bullard, J. W.; Sant G. Calcium nitrate: A chemical admixture to inhibit aggregate dissolution and mitigate expansion caused by alkali-silica reaction. *Submitted to Journal of Cement and Concrete Composites* (August **2019**).

- Chapter 7 is a version of: Oey, T.; Jones, S.; Bullard, J. W.; Sant, G. Machine learning can predict setting behavior and strength evolution of hydrating cement systems. *Accepted with minor revisions by Journal of the American Ceramic Society* (July **2019**).

Finally, I would like to acknowledge the funding sources that supported my graduate study:

- The COMAX Consortium

- The University of California, Los Angeles

- The Federal Highway Administration, Dwight D. Eisenhower Transportation Fellowship Program; Grant number: 693JJ31845049

Vita

Education

2014	B. S., Civil Engineering, University of California, Los Angeles
2015	M. S., Civil Engineering, University of California, Los Angeles

Awards

2012	Undergraduate Research Fellows Program Scholarship
2013	Dean's Prize Honoring Outstanding Undergraduate Researchers
2014	Harry M. Showman Prize for Engineering Research (Undergraduate)
2015	Outstanding Masters Student in Civil and Environmental Engineering
2016	Honorable Mention: NSF Graduate Research Fellowship Program
2017	Dwight D. Eisenhower Transportation Graduate Fellowship
2018	American Ceramic Society Best Paper Award (10.1111/jace.15122)
2019	Harry M. Showman Prize for Engineering Research (Graduate)

Publications

La Plante, E. C.; Oey, T.; Hsiao, Y-H.; Perry, L.; Bullard, J. W.; Sant, G. Enhancing Silicate Dissolution Kinetics in Hyperalkaline Environments. *Journal of Physical Chemistry C* **2019**, *123* (6), 3687–3695.

Oey, T.; Frederiksen, K.; Mascaraque, N.; Youngman, R.; Balonis, M.; Smedskjaer, M.; Bauchy, M.; Sant, G. The Role of the Network-Modifier's Field-Strength in the Chemical Durability of Aluminoborate Glasses. *Journal of Non-Crystalline Solids* **2019**, *505*, 279–285.

Wei, Z.; Wang, B.; Falzone, G.; La Plante, E. C.; Okoronkwo, M. U.; She, Z.; Oey, T.; Balonis, M.; Neithalath, N.; Pilon, L.; Sant, G. Clinkering-free cementation by fly ash carbonation. *Journal of CO2 Utilization* **2018**, *23*, 117–127.

Oey, T.; Hsiao, Y.; La Plante, E. C.; Wang, B.; Pignatelli, I.; Bauchy, M.; Sant, G. Rate Controls on Silicate Dissolution in Cementious Environments. *RILEM Technical Letters* **2017**, *2*, 67–73.

Oey, T.; Pignatelli, I.; Yu, Y.; Neithalath, N.; Bullard, J. W.; Bauchy, M.; Sant, G. Topological Controls on the Dissolution Kinetics of Glassy Aluminosilicates. *Journal of the American Ceramic Society* **2017**, *100* (12), 5521–5527.

Oey, T.; Timmons, J.; Stutzman, P.; Bullard, J. W.; Balonis, M.; Bauchy, M.; Sant, G. An Improved Basis for Characterizing the Suitability of Fly Ash as a Cement Replacement Agent. *Journal of the American Ceramic Society* **2017**, *100* (10), 4785–4800.

Kumar, A.; Oey, T.; Falzone, G.; Huang, J.; Bauchy, M.; Balonis, M.; Neithalath, N.; Bullard, J.; Sant, G. The Filler Effect: The Influence of Filler Content and Type on the Hydration Rate of Tricalcium Silicate. *Journal of the American Ceramic Society* **2017**, *100* (7), 3316–3328.

Oey, T.; Kumar, A.; Falzone, G.; Huang, J.; Kennison, S.; Bauchy, M.; Neithalath, N.; Bullard, J.; Sant, G. The Influence of Water Activity on the Hydration Rate of (Triclinic) Tricalcium Silicate. *Journal of the American Ceramic Society* **2016**, *99* (7), 2481–2492.

Stoian, J.; Oey, T.; Bullard, J. W.; Huang, J.; Kumar, A.; Balonis, M.; Terrill, J.; Neithalath, N.; Sant, G. New Insights into the Prehydration of Cement and its Mitigation. *Cement and Concrete Research* **2015**, *70*, 94–103.

Oey, T.; Stoian, J.; Li, J.; Vong, C.; Balonis, M.; Kumar, A.; Franke, W.; Sant, G. Comparison of $Ca(NO_3)_2$ and $CaCl_2$ Admixtures on Reaction, Setting, and Strength Evolutions in Plain and Blended Cementing Formulations. *ASCE Journal of Materials in Civil Engineering* **2014**, *27* (10), 04014267.

Fernandes, F.; Manari, S.; Aguayo, M.; Santos, K.; Oey, T.; Wei, Z.; Falzone, G.; Neithalath, N.; Sant, G. On the Feasibility of Using Phase Change Materials (PCMs) to Mitigate Thermal Cracking in Cementitious Materials. *Cement and Concrete Composites* **2014**, *51*, 14–26.

Kumar, A.; Ketel, S.; Vance, K.; Oey, T.; Neithalath, N.; Sant, G. Water Vapor Sorption in Cementitious Materials: Measurement, Modeling and Interpretation. *Transport in Porous Media* **2014**, *103* (1), 69–98.

Kumar, A.; Oey, T.; Kim, S.; Thomas, D.; Badran, S.; Li, J.; Fernandes, F.; Neithalath, N.; Sant, G. Simple Methods to Estimate the Influence of Limestone Fillers on Reaction and Property Evolution in Cementitious Materials. *Cement and Concrete Composites* **2013**, *42*, 20–29.

Kumar, A.; Oey, T.; Falla, G. P.; Henkensiefken, R.; Neithalath, N.; Sant, G. A Comparison of Intergrinding and Blending Limestone on Reaction and Strength Evolution in Cementitious Materials. *Construction and Building Materials* **2013**, *43*, 428–435.

Vance, K.; Aguayo, M.; Oey, T.; Sant, G.; Neithalath, N. Hydration and Strength Development in Ternary Portland Cement Blends Containing Limestone and Fly Ash or Metakaolin. *Cement and Concrete Composites* **2013**, *39*, 93–103.

Oey, T.; Kumar, A.; Bullard, J. W.; Neithalath, N.; Sant, G. The Filler Effect: The Influence of Filler Content and Surface Area on Cementitious Reaction Rates. *Journal of the American Ceramic Society* **2013**, *96* (6), 1978–1990.

Chapter 1: Introduction

1.1 Scope and objectives

Global climate change, one of the most daunting problems facing contemporary society, is caused by human-induced emissions of greenhouse gases.[1] Of the greenhouse gases produced, carbon dioxide (CO_2) is the majority contributor in exacerbating this problem.[2] Out of global anthropogenic CO_2 emissions, the cement industry accounts for an estimated 9% of the total.[3] Ordinary portland cement (OPC) plays a role as the binder component of concrete, reacting with water to bind together the aggregates, or crushed rocks, into a cohesive material, and thus is consumed in great quantities by the construction industry.[4] The source of CO_2 emissions from OPC production is twofold: (1) raw materials must be heated to about 1450°C, requiring substantial fuel combustion, and (2) upon heating limestone, one of the principal raw materials, it de-carbonates, releasing CO_2 in a process called calcination, to form calcium oxide, the key component that lends cement its ability to perform as a hydraulic binder (i.e., one which reacts with water to form hydrated reaction products that are not readily water-soluble). While the emissions from the former step may be reduced by employing renewable power or energy-efficient technologies for production processes, calcination of limestone accounts for roughly half of CO_2 release, and is an unavoidable consequence of cement production.[5,6]

As strategies for reduction in CO_2 emissions by cement production are limited, the focus has turned to reductions achievable through changes in cement use. To improve sustainability of cement and concrete use, two main strategies have emerged: (1) to consume less cement by replacing it in part or in whole with supplementary cementing materials (SCMs), or (2) to consume less concrete, either through more sparing use as prescribed by design, or through improved durability (i.e., by

mitigating the detrimental effects of reactive aggregates), enabling a longer service lifetime of concrete infrastructure.[7] This second approach, to improve the durability of concrete, is itself limited by drawbacks imposed by the nature of the aggregates required, which must be cost effective and locally available for use as aggregates in these low-CO_2 concretes.

Typical locally available aggregates can pose problems, given that they may occasionally contain reactive silicate phases that induce alkali-silica reaction (ASR), limiting infrastructure service life. ASR is characterized by the dissolution of reactive silicate materials and subsequent precipitation of expansive gel products, which induce volume change and cracking of concrete, and is noted to occur for several varied aggregate rock types, the reactive components of which are generally either sedimentary or amorphous.[8] High-quality aggregate, in this case that which does not contain reactive silicates, is becoming an increasingly scarce resource, and in many cases the identification of potentially reactive aggregates is either time-intensive or inaccurate.[9] Given this scarcity, much attention has been paid to ASR mechanisms and potential mitigation strategies, so that increasingly reactive aggregates may be safely used without detrimental effect.[10] As the reactive silicate component of many aggregates is natural glass inclusions (ASR has also been evidenced to occur readily in concretes containing waste glass), and standard testing procedures (e.g., ASTM C441) recognize the utility of employing borosilicate glass, as a "worst case" aggregate, to model ASR progression, there is a clear need for further study of similar glassy silicates in order to develop a consistent means of limiting their dissolution rates in alkaline environments to mitigate ASR.[8,11,12]

Locally available SCMs, while most often used as binding agents to partially replace cement, may also function to mitigate ASR. Many SCMs are aluminosilicate materials: blast furnace slag, fly

ash, natural pozzolans, and silica fume, to name a few of the most common. While the conditions of origin of these SCMs are similar (i.e., they are byproducts of either natural or industrial high-temperature processes), an important distinction should be made as to their role in cementitious systems: blast furnace slag and high-calcium fly ash fill the role of hydraulic binders, in that their constituent phases, both glassy and crystalline calcium aluminosilicates, incorporate sufficient calcium oxide to approach or resemble the behavior of cement; low-calcium fly ash, natural pozzolans, and silica fume, on the other hand, do not act independently as hydraulic binders, in that their constituent phases consist mainly of siliceous and aluminous material that requires either an external source of calcium to produce cementitious products via pozzolanic reaction, or alkali-activation to produce comparable products by geo-polymerization.[13,14] This distinction somewhat parallels trends in the current usage of these materials: blast furnace slag and high-calcium fly ash, as well as silica fume, are already heavily utilized due to their hydraulic properties or very fine particle sizes, which already enable the high-volume replacement of cement, or the production of high-performance concretes, respectively. Low calcium fly ash, however, is underutilized due to its potentially low reactivity relative to its high-calcium counterparts, typically attributed to its lower calcium content, though this is not always the case.[15] This problem is compounded by the difficulty in characterizing fly ash, due to its nature as a heterogeneous and largely amorphous coal-combustion byproduct with highly variable composition, and the potential deleterious effects that it may have on concrete property development, such as delayed setting and reductions in compressive strength.[16–19] As such, despite widespread availability of low-calcium fly ash (as compared to the rarity in occurrence of natural pozzolans), and its known effectiveness in mitigating ASR when used in conjunction with reactive aggregates,[10] much of it goes unused due

to insufficient understanding of the aqueous reactivity (i.e., dissolution rate) of its glassy silicate and aluminate components.[15]

Removing the barriers that ASR induced durability problems pose to further reductions in cement use, which are caused by reactive glass within aggregates and mitigated by glassy SCMs, thus requires an improved understanding of the dissolution of silicate and aluminate glasses. Such understandings would not only provide benefits in terms of improved utilization of waste byproduct materials such as fly ash, but also have cross-disciplinary impacts in other fields where glass reactivity holds importance, e.g., the study of more durable silicate glasses for nuclear waste containment, or the study of how enhanced weathering of natural silicates may accelerate long-term CO_2 uptake from the atmosphere.[20–22] The research described herein aims to fill the knowledge gaps that prevent optimal utilization of reactive aggregates, and associated utilization of SCMs. To do so, it focuses on the dissolution of glassy silicate and aluminate phases in alkaline aqueous environments, as would be encountered in a typical cement pore solution.

1.2 Organization

This document is divided into nine chapters, with the first serving to outline the background and motivations contributing to the research undertaken herein. In the context of cementitious systems, it is noted above that many cement-adjacent materials, i.e., fly ash and reactive aggregates, contribute to the properties of the resulting cement paste, mortar, or concrete by way of dissolution-precipitation processes. As the exact linkages between the chemical structure of these cement-adjacent materials and the resulting properties of the mixture of which they are a part remain poorly understood, the current research has focused primarily on the following two hypotheses, proposed

to gain better understanding of the *initial dissolution* of fly ash and reactive aggregates in cementitious systems:

- That dissolution rates of silicate and aluminate glasses, i.e., those representative of fly ash and/or reactive aggregates, may be described by simplified metrics derived from the composition and structure of the glass.
- That the dissolution rates of such glasses may be controlled by introducing solvated ions.

Chapter two introduces a new framework from which to consider low-reactivity silicates, i.e., fly ash, by calculating the average number of broken bonds per unit within the network-like structure of its majority phase: aluminosilicate glass. This metric, termed "network ratio" (N_r), is shown to roughly relate to the extent of reaction and the rate of strength gain for cementitious mixtures containing large quantities of fly ash. Such a result supports the idea that simplified, averaged metrics reflecting chemical composition and structure of a constituent aluminosilicate can prove successful in describing macroscopic properties, assumedly via their reflection in material reactivity, i.e., dissolution rate.

Chapter three further explores the relation between fly ash structure and dissolution rate by calculating the average number of topological constraints per atom (n_c) and linking it directly to fly ash dissolution rate. In considering rigidity alongside connectivity of glass networks, this link supports the idea that for fly ash, material structure can have a direct bearing on dissolution rate and, as outlined in chapter two, resulting cement paste properties. Beyond this, an Arrhenius-like approach to calculating constraint-dependent activation energy among aluminosilicate glasses, as proposed by previous studies,[23] enables a further distinction to be made with regard to the role of

network-forming atoms and network-modifying atoms within glass. Whereas the network-forming atoms, e.g., silicon (Si) and aluminum (Al), are evidenced to broadly dictate the "strength" (E_0, roughly 25 kJ/mol) of network constraints, the network-modifying atoms, e.g., sodium (Na) and calcium (Ca), are evidenced to mainly dictate connectivity (n_c) between network-forming atoms.

Chapter four takes up the specific influences of network-modifying atoms on structure and reactivity in the context of aluminoborate glass, which is well-known for the varied coordination state of its network forming atoms, boron (B) and aluminum (Al). While increasing abundance of network-modifying atoms causes proportional decreases in the number of inter-unit bonds formed in the glass network to satisfy charge balance, this research focused on the influence of varied modifier type (Li, Mg, Ca, Sr, Ba) at a fixed abundance. In doing so, the role of a modifier's charge-to-radius ratio is elucidated: beyond breaking inter-unit bonds as dictated by charge balance, relatively smaller and more highly charged modifiers (e.g., Mg^{2+}) also broadly *increase* the average coordination state of aluminum atoms, as reflected in the decreased reactivity of aluminoborate glass for such modifiers (Mg < Ca < Sr < Ba). Furthermore, the network structure consisting of relatively "weaker" boron-aluminum bonds (E_0, roughly 8 kJ/mol) is noted to benefit to a smaller degree from these increases or decreases in local network connectivity, than, as an example, an aluminosilicate network such as that in fly ash or reactive aggregates might.

Chapter five, returning to study of aluminosilicate glass, attempts to replicate results obtained for fly ash in chapter two by using synthetic glass targeted to similar compositions as the averages obtained from real fly ashes, though across a wider range of temperature and solution pH conditions. Interestingly, while the dependence of initial dissolution rate on number of constraints

is maintained at relatively lower solution pH values (pH 10), elevation of pH to 13 evidences dissolution rates entirely independent of the structure of the initial glass. This implies that in realistic cementitious systems, as cement hydration progresses and elevates solution pH, the role of fly ash glass's *initial* structure becomes less relevant to its dissolution behavior, i.e., implying further investigation is needed of the alteration of such glass over time. While the role of fly ash in replacing cement is still shown to depend on such reactivity in chapter 1, this calls into question another of the known functions of fly ash: suppression of alkali-silica reaction.

Chapter six turns to the role of silicate reactivity in alkali-silica reaction (ASR) progression, both in the presence and the absence of calcium (Ca) and aluminum (Al), known to be released during cement hydration as well as from fly ash. The dissolution rate of borosilicate glass, a common proxy for reactive aggregates in ASR mitigation tests, is shown to be suppressed by the presence of both Ca and Al. Furthermore, this suppression is shown to parallel decreases in the expansion of mortar specimens caused by added calcium (as a nitrate salt). While low levels of Ca and Al, on the order of those typical to a cement pore solution, produce elevations in the activation energy of dissolution, this is shown to be insufficient to achieve the expansion reductions indicative of effective ASR mitigation: surface area reductions (precipitate formation) achieved by yet higher concentrations of Ca are demonstrated to be necessary to enable ASR mitigation. This highlights a new class of methods for ASR mitigation: high-concentration alkaline earth nitrate admixtures.

Beyond the above, however, results of chapter 6 also lead to a critical qualification regarding the role played by fly ash in mitigating ASR: while it functions as a Ca and Al source, fly ash glass as used in chapter 5 may: (a) suppress its own dissolution upon release of sufficient concentrations

of said elements under laboratory conditions, and thus (b) depend more closely on its composition (as in chapter 2) than its structure (as in chapter 3) when used for ASR mitigation in realistic cement pastes, given the unexpected changes to its dissolution rate under hyper-alkaline conditions over a range of synthesized structures (as discussed in chapter 5). However, even utilizing the extensive characterization data of chapter 2, only weak correlations between simplified compositional descriptors (N_r) and expansion reductions induced by a given fly ash are obtained. Given the difficulty of simplifying the description of an extremely heterogeneous material such as fly ash to a single parameter (N_r, n_c), as well as that of simplifying description of a complex multi-part reaction such as cement hydration followed by ASR to a single process (initial dissolution), further work is likely to benefit from data-driven modeling, i.e., by utilizing machine learning estimators to test the validity of previously discussed results while obviating the need for detailed mechanistic understanding by merit of using a larger, more representative data set.

Chapter seven takes preliminary steps in extending existing machine learning (ML) models, developed for the estimation of concrete compressive strength,[24] to also estimate other properties, such as setting time, as a function of more varied cement compositions. In this regard, ML estimations are relatively successful in extending to both accommodating cement composition as an input and to estimating setting time in addition to compressive strength as an output, for surprisingly low quantities of input data (an approximate minimum of 200 data records). However, several key problems are highlighted that currently impede engineering application of ML methods, most significantly the way in which model accuracy is defined and the tendency toward biased estimations without proper pre-processing of the input data. As such, while ML methods do represent a promising new tool for future efforts to investigate fly ash reactivity and ASR

mitigation, extreme caution should be exercised prior to their application in wider engineering practice due to the need for more rigorous quantification of individual estimation errors.

Chapter eight summarizes conclusions of the research and recommends future work, namely by providing several qualifications to the two central hypotheses.

Chapter nine provides a list of references cited herein.

Chapter 2: An improved basis for characterizing suitability of fly ash as a cement replacement agent

2.1 Chapter scope

Environmental concerns related to the production of ordinary portland cement (OPC) are creating opportunities to partially replace it with increasing amounts of supplementary cementitious materials (SCMs) in the binder phase of concrete.[7,25] Fly ash, a byproduct of the combustion of coal, is an established SCM, which is abundant and has the potential to be used to replace OPC at levels up to 50 % (by mass),[26,27] as well as to mitigate common durability problems such as alkali-silica reaction.[28] However, the use of fly ash at high OPC replacement levels can retard cement hydration, delay setting, and reduce the rate of early age strength development.[29,30] As such, to consistently expand OPC replacement by fly ash, it is necessary to better understand its composition and structure to estimate the limiting level up to which a given fly ash can be used to replace OPC without detrimentally influencing binder (and concrete) performance.

Recent studies have recognized the need for improved characterization of both the crystalline and amorphous phases in fly ash, due to its heterogeneous nature as a coal combustion by-product.[31,32] Current standards (e.g., ASTM C618)[33] classify fly ashes as Class C or Class F, a discrimination that while quantitative, does not provide enough detail to permit estimation of reactivity of a fly ash or its suitability and synergy as a cement replacement agent. While several studies have investigated the performance of fly ash as an SCM,[34–39] fewer studies have elucidated the linkages among fly ash composition, reactivity, and binder performance,[40–42] (*e.g.*, by detailed analysis of its constituent phases).[31,32,41,43] The aim of this chapter is to formalize a comprehensive means for characterizing fly ashes. As such, seven U.S. fly ashes spanning Class C and Class F designations

are characterized to obtain their crystalline and amorphous compound contents and compositions. The reactivity of these fly ashes in cement-fly ash blends, and the evolutions of properties are linked to fly ash composition. A new parameter, the network ratio (N_r, unitless), is proposed as a figure of merit of fly ash performance as an SCM. The outcomes of this chapter provide an informed basis to enhance the use of fly ash as an SCM.

2.2 Materials

An ASTM C150 compliant Type I/II ordinary portland cement (OPC) was used.[33] The phase composition of the OPC, as determined by quantitative X-ray diffraction (QXRD) and Rietveld refinement.[44] was estimated as (by mass)[i]: (56.5 ± 2.3) % MIII-Ca_3SiO_5, (16.0 ± 1.4) % β-Ca_2SiO_4, (6.3 ± 0.8) % $Ca_3Al_2O_6$, (11.4 ± 1.0) % $Ca_4Al_2Fe_2O_{10}$, (1.1 ± 0.6) % $CaSO_4{\cdot}2H_2O$, (0.5 ± 0.8) % $CaSO_4{\cdot}0.5H_2O$, (1.2 ± 0.6) % $CaSO_4$, (1.2 ± 0.4) % $Ca(OH)_2$, (0.5 ± 0.4) % CaO and (4.6 ± 0.5) % $CaCO_3$. The seven fly ashes used are from commercially available sources in the U.S. and were selected to represent a range of compositions. This includes three Class C fly ashes and four Class F fly ashes, as specified by and compliant with ASTM C618.[33] The fly ash compositions, in terms of their crystalline and amorphous phases, and the methods for their analyses are detailed in Tables 1 and 2. Each fly ash is designated by a letter-number combination designating Class F or Class C, and an arbitrary index (C1, C2, etc.) as shown in the tables.

2.3 Characterization methods

2.3.1 *Physical properties*

[i] Unless stated otherwise, uncertainties are reported as one standard deviation.

Particle size distributions: The particle size distributions (PSD) of the OPC and the fly ashes were measured by laser scattering (Beckman Coulter light-scattering analyzer LS13-320[ii]) using IPA (isopropanol) and sonication for dispersing the powders to primary particles. The results of the measurement are shown in Figure 1. Assuming spherical particles, the surface area of the cement is estimated as 636 m^2/kg, which is in the range of the measured surface area of the fly ashes.

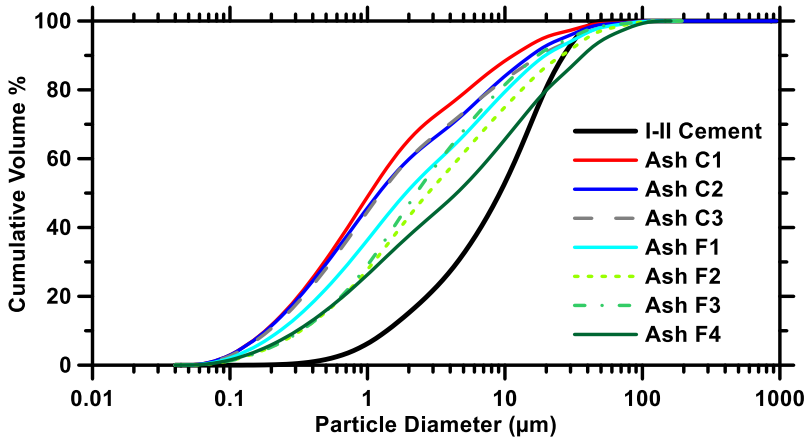

Figure 1: The particle size distributions of the cement and fly ashes. The relative standard deviation in the median particle size (d_{50}) is approximately 6 %, based on six replicates on the same sample and assuming a solid density of 3150 kg/m^3.

Surface area: Nitrogen multipoint adsorption and desorption isotherms (Micrometrics ASAP 2020 BET analyzer) were used to characterize the specific surface area of the powders. Prior to the measurements, the solid samples were evacuated for two hours at 300 ºC. The specific surface area was calculated using the BET equation. The N_2-BET surface areas of the solids are noted in Table 1.

[ii] Certain commercial materials and equipment are identified to adequately specify experimental procedures. In no case does such identification imply recommendation or endorsement by the University of California, Los Angeles, or the National Institute of Standards and Technology, nor does it imply that the items identified are necessarily the best available for the purpose.

Heat capacity: Quantitative isothermal conduction calorimetry, used in this study to monitor the overall reaction of fly ash with water, requires knowledge of the specific heat capacity of each component in the mixture. The heat capacities of the solids were measured using a hot disk thermal constants analyzer using the transient plane source method.[45] Approximately 1 g of powdered fly ash was used for each measurement, which consisted of a 1 h equilibration period followed by three repeat measurements. Each measurement consisted of applying a 0.1 W heat pulse for 80 s, with the temperature being maintained at 22 °C to 23 °C for the duration of the experiment.

Density: Fly ash densities were measured by a gas pycnometer (Micrometrics Accupyc II 1340), using helium as the purge gas. Around 3.5 g of fly ash were used for each measurement, with a cyclical helium flush procedure set to repeat until stable vacuum pressure (degas stage) is achieved, followed by the collection of ten data points obtained via additional helium purges.

Loss on ignition (LOI) and glass transition temperature (T_g): The loss on ignition (LOI) and the glass transition temperature of the amorphous compounds in a fly ash were determined by thermal analysis (TGA/DTG/DTA, TA Instruments SDT Q600 Thermal Analyzer) using pure alumina crucibles. The samples were equilibrated at 35 °C for one minute, and then heated in a single step from 35 °C to 980 °C at a heating rate of 10 °C/min. The LOI (g/g) of the fly ash is noted to be largely a result of unburnt carbon, details of which are further discussed in Section 1.5.3. The glass transition temperature (T_g) was measured by DTA (10 °C/min), using the slope-intercept method.[46] This method uses the intersections of linear fits to approximate the onset of the minor peak in heat flow, created due to the change in heat capacity of the glassy compounds. It should be noted

however, that T_g is known to depend on the glass structure, the measurement method, and the conditions under which the glass was formed (*e.g.*, the cooling rate).[47]

Bulk and mineralogical compositions: Each fly ash was characterized in terms of its crystalline and amorphous compound compositions. The bulk oxide composition of each fly ash was determined using X-ray fluorescence, using ASTM D4326[33] (XRF, Table 1). Quantitative X-ray diffraction (QXRD) analyses were carried out on powdered fly ash samples (Table 2). First, samples were ground in a micronising mill (McCrone)[ii], using approximately 4 g of powder and approximately 25 mL of ethanol as a grinding aid. Following grinding, the powders were vacuum filtered and oven dried at about 60 °C for 30 min. ZnO was added as an internal standard to make up about 20 % by mass of the final sample. This mixture of the fly ash solids and ZnO was hand ground in a mortar and pestle with ethanol for two minutes after which it was air dried. The powder samples were mounted in metallic (zero-background) holders, and the surface gently textured to minimize preferred orientation errors. An X-ray diffractometer (Bruker D-8 Advance)[ii] in a θ-θ configuration using Cu-Kα radiation (λ = 1.54 Å) was used for analysis. The samples were scanned on a rotating stage between 5° and 70° (2θ) in continuous mode with a six second step time. X-ray diffraction structure model information for relevant anhydrous and hydrated crystalline phases was sourced from the literature or standard databases and was used as a starting point for Rietveld refinement. The Rietveld refinement was carried out using the TOPAS software provided with the instrument, which was provided with a custom control file for quantitative analysis of X-ray patterns.

Table 1: The simple oxide compositions of fly ashes measured by X-ray fluorescence (mass %). The standard error (σ) given in the last column indicate typical values listed for the technique.[44]

	Class C			Class F				σ
	C1	C2	C3	F1	F2	F3	F4	(±)
SiO_2	35.44	36.08	40.08	50.75	53.97	60.48	57.98	0.40
Al_2O_3	17.40	18.03	20.44	15.77	20.45	22.85	27.71	0.20
Fe_2O_3	7.15	6.02	6.29	6.28	5.62	4.47	6.35	0.10
SO_3	2.34	2.91	1.62	0.79	0.52	0.46	0.25	0.10
CaO	26.45	25.90	21.35	15.05	12.71	5.20	1.64	0.40
Na_2O	1.90	1.86	1.46	3.29	0.57	2.14	0.50	0.03
MgO	5.73	5.24	4.56	4.57	2.84	1.19	1.07	0.10
K_2O	0.53	0.46	0.71	2.14	1.11	1.31	2.69	0.04
P_2O_5	0.95	1.03	1.23	0.24	0.30	0.14	0.17	0.01
TiO_2	1.19	1.34	1.42	0.61	1.29	1.16	1.38	0.01
Total	99.08	98.87	99.16	99.49	99.38	99.40	99.74	
Density (kg/m^3)	2760	2690	2650	2590	2470	2330	2360	
d_{50} value (μm)	0.95	1.15	1.15	2.21	1.83	2.66	4.24	
Surface area (m^2/kg)	4290	750	1720	570	620	1720	1990	

Table 2: The crystalline compound composition of the fly ashes measured by quantitative X-ray diffraction and Rietveld refinement (mass %), and the corresponding standard errors.[48]

	Class C			Class F				σ
	C1	C2	C3	F1	F2	F3	F4	(%)
Quartz	10.06	11.10	9.81	6.83	16.64	16.48	14.15	10
Mullite	0.86	0.90	1.14	-	5.08	10.17	20.01	10
Anhydrite	2.80	1.84	1.01	1.61	0.97	-	-	15
Lime	1.16	1.04	0.33	-	-	-	-	15
Periclase	3.81	2.17	2.50	1.70	0.30	0.19	-	20
Magnetite	1.66	2.36	1.64	2.08	1.76	2.03	1.96	15
Merwinite	6.98	4.19	3.98	3.66	-	-	-	25
Calcio-Olivine	0.43	1.34	1.57	-	-	-	-	-
Ilmenite	-	-	-	0.58	-	-	-	-
β-C_2S	4.50	6.30	5.75	-	-	-	-	1.4
C_2AS	4.45	3.27	3.76	-	-	-	-	-
C_3A (cubic)	5.90	5.06	6.14	-	-	-	-	25
C_3A (orthorhombic)	2.13	2.73	2.90	-	-	-	-	25
Amorphous	55.25	57.69	59.47	83.53	75.25	71.13	63.87	2
Total	100	100	100	100	100	100	100	

The elemental composition of each fly ash was assessed using carbon coated polished sections in an FEI Quanta 600 scanning electron microscope (SEM) in high vacuum mode. The analysis was carried out at a magnification of 750x, beam current of 2 nA, and filament voltage of 1.76 V. The fly ash embedded epoxy sections (Epotek 353ND, noted to be resistant to particle plucking as well as stable under electron beams) were polished using sequentially finer grades of SiC sandpaper (grit numbers 320, 400, 600, 800, and 1200) adhered to a spinning-disk sander, followed by sequentially finer grades of diamond paste (6 µm, 3 µm, 1 µm, and 0.5 µm) carried on single-use polishing cloths. The fly ash embedded epoxy sections were rinsed with ethanol intermittently between polishing steps and with acetone after final polishing.

Backscatter electron imaging, elemental maps, and point compositions were obtained using X-ray energy dispersive X-ray spectroscopy (EDS) at an accelerating voltage of 12 kV across multiple fields of view for each fly ash. Hyperspectral image analysis was performed in ImageJ[49] and Multispec,[50] with compositional clustering performed using the methodology of Chancey et al.[31,32] Automatic rather than manual clustering was used whenever possible to minimize operator bias in the results. The geochemical data (GCD) kit software was used to confirm the manual and multispectral clustering analyses, using the tabulated compositions from point map (atomic) data as an input.[51]

2.3.2 *Evaluation of fly ash reactivity and engineering performance*

Cementitious paste mixtures were prepared using deionized water at a w/s = 0.45 (water-to-solids ratio, mass basis) according to ASTM C305.[33] Fly ash replaced cement at levels of 10 %, 20 %,

and 50 % by mass.[iii] The influence of OPC replacement by fly ash on reactions was measured using isothermal calorimetry (TAM Air, TA Instruments)[ii] to track heat evolved during hydration. The thermal power and energy measured were used to assess the influence of fly ash additions on cumulative heat release and reaction kinetics of the cement-fly ash blends.

The compressive strength of cubic specimens, 50 mm on a side, cured at (25.0 ± 0.2) ºC was measured as per ASTM C109 at 1 d, 3 d, and 7 d.[33] The compressive strength value reported is the average of three specimens. The coefficient of variation (CoV) of measured compressive strengths was approximately 10 % for samples cast from the same batch.

2.4 The network ratio (N_r) as a descriptor of fly ash composition and structure

Fly ashes are composed primarily of aluminosilicate glasses, as evidenced by the amorphous content in Table 2. However, depending on the coal stream, fly ashes can contain substantial CaO; distinctions based on total CaO content led to the Class C and Class F fly ash designations which separate the two classifications based on the sum of SiO_2, Al_2O_3, and Fe_2O_3 percentages (i.e. closely approximated by CaO content making up most of the remainder of oxide phases as determined by X-ray fluorescence).[54] While early studies correlated fly ash properties with the bulk CaO content,[55] more recently the contents of the network-modifying elements have been identified as being critical variables that influence fly ash performance.[43,56] Aluminosilicate

[iii] It should be noted that replacement of cement by fly ash at a fixed water-to-solids ratio results in a changing water-to-cement ratio: 0.45, 0.5, 0.563, and 0.9 for the reference, 10%, 20%, and 50% systems, respectively. The effects of this change have been noted, and we refer readers to Ref. [52] in which it is illustrated that for this range of water-to-cement ratios, the reaction kinetics are independent of water content unless additional surface area is provided by fillers (i.e. fly ash in this case). Changing water content will impact the initial porosity of the system, however, and so compressive strength values reported here have been normalized by water content as suggested by Ref. [53] to reflect these changes.

glasses found in fly ash consist of a random network of silicate tetrahedra which may be linked at each corner to one other silicate tetrahedron.[47,57] This glass structure can incorporate metal oxides that contribute cations to the network. Low valence cations, such as calcium, potassium, magnesium, and sodium, are termed network modifiers, and exist in the interstitial volume, between the networked silicate tetrahedral.[58] These so-called *modifiers* destabilize the glass network by creating non-bridging oxygen (NBOs) atoms that balance excess charge, thereby disconnecting a number of silicate network units as shown in Figure 2(a).[59]

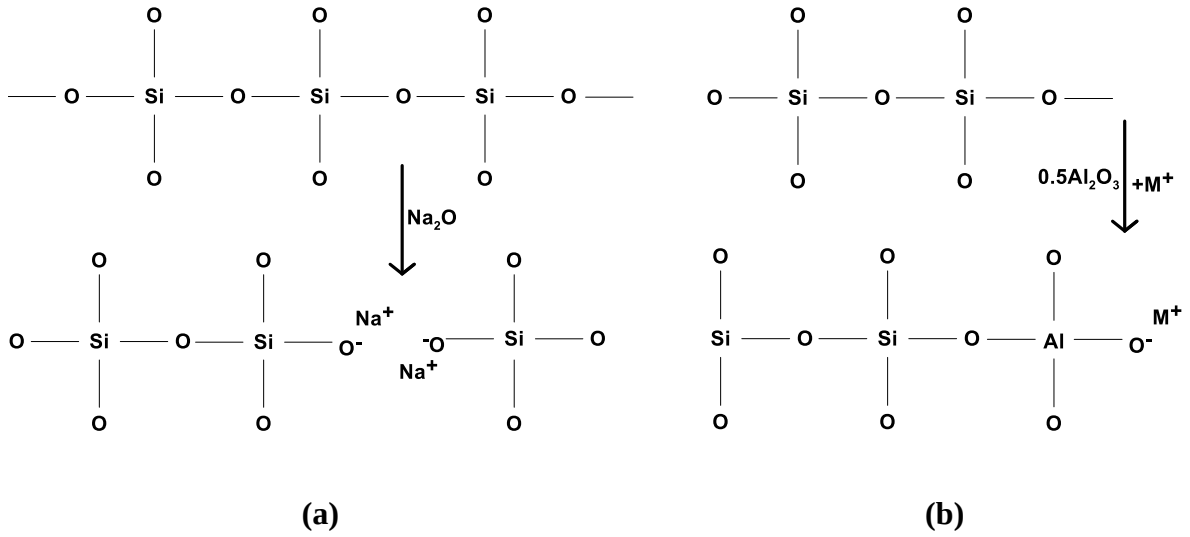

Figure 2: An illustration of: (a) how network modifiers create non-bridging oxygens, thus disconnecting silicate tetrahedra in the glass structure from each other, and (b) how aluminum incorporation in the network reduces non-bridging oxygens, increasing network connectivity.

Alkali ions are weakly bound to these NBOs, and the higher mobility of the alkalis combined with lowered network connectivity (due to the formation of NBOs) increases the extent of disorder of fly ash glasses. This is significant, as disorder may serve as an excellent indication of the reactivity of fly ashes in water.[23] In aluminosilicate glasses, aluminum functions as a network former, like

silicon, occupying tetrahedral sites that are linked at the corners.[57,59] Aluminum occupation of tetrahedral sites normally occupied by silicon creates an unbalanced charge of -1 unit (due to valence mismatch) that must be balanced by a cation in the interstices. This allows for incorporation of network modifiers into the glass without the creation of additional NBOs, thereby increasing network connectivity relative to silicate modified glasses, as shown in Figure 2(b).

The approach to characterize the amorphous compounds in a fly ash is to resolve a single parameter that provides meaningful indication of a fly ash's anticipated performance as a cement replacement agent. While the use of such a parameter is a simplification – since it does not account for the conditions under which the fly ash glassy phase formed, nor the crystalline phases present – it provides a functional means to reflect the structural/compositional effects of fly ash glass on its performance as an pozzolan.

For a single parameter to be descriptive of the wide range of glass compositions present in fly ash, it must account for both the network modifiers and network formers. For fly ash, a simple metric that provides a more encompassing description of glass composition and structure than the basic Class C/Class F designation is represented by a new parameter called the network ratio (N_r):

$$N_r = \frac{2\times(X_{Ca}+X_{Mg})+X_K+X_{Na}-X_{Al}}{X_{Si}+X_{Al}} \quad \text{for } \left[\frac{Al_2O_3}{M_2O+M'O}\right] < 1 \qquad \textbf{Equation (1a)}^{iv}$$

$$N_r = 0 \qquad \text{for } \left[\frac{Al_2O_3}{M_2O+M'O}\right] > 1 \qquad \textbf{Equation (1b)}$$

[iv] In the conditional second half of Equation 1a and Equation 1b, the quantities in square brackets represent mass fractions, *not* mole fractions.

where X_{Ca}, X_{Mg}, X_K, X_{Na}, X_{Al}, and X_{Si} are the mole fractions of calcium, magnesium, potassium, sodium, aluminum, and silicon in the glasses, respectively, and $M_2O + M'O$ represents the contents (mass fraction) of alkali (M) and alkaline earth (M') cations present in the interstices of the glass, which must be balanced by formation of aluminum tetrahedra or NBOs. The molar contents of the above noted elements in the fly ash glass are determined by simply subtracting the molar composition corresponding to the crystalline phases (from QXRD) from the molar composition corresponding to the bulk chemical composition (from Table 1). The construction of Equation (1) assumes full compensation of charge by aluminum tetrahedra prior to the formation of NBOs for aluminum-modifier ratios less than one, and the elimination of NBOs for aluminum-modifier ratios greater than unity.

The network ratio thus represents the number of NBOs per tetrahedral unit in the glass structure such that $N_r = 4$ implies tetrahedral monomers (*i.e.*, Q^0 units) while $N_r = 0$ implies complete connectivity (Q^4 units). Merely quantifying the number of NBOs would disregard the field strength and coordination state of ions, and the presence of network forming species such as calcium (a non-tetrahedral network former).[60] As a prominent example, aluminum can alter its coordination state to show octahedral coordination, or to act as a network modifier at high $[Al_2O_3/(M_2O+M'O)]$ ratios.[47,57] While parameters such as network ratio that quantify "the degree of network de-polymerization" for a glass, are well-established[57] and have been shown to be poorly related to reactivity in "fully compensated" glass systems (*i.e.*, $[Al_2O_3/(M_2O+M'O)] \geq 1$),[23] *in the specific case of high-modifier glass,* as is present in fly ash, the network ratio accurately embodies the compositional and structural characteristics of such materials.

It should be noted that N_r here represents "connectivity" averaged across all glassy compositions, though it is known that the connectivity of individual tetrahedral units may vary, along with local compositions. As such, network ratio as determined above ***does not*** encompass local heterogeneities and represents the "smeared material average" for the wide array of glassy compositions occurring in a single fly ash. This smeared treatment of both composition and structure, and by extension estimation of reactivity, arises out of simple expediency: network ratio represents a compromise between effective and efficient characterization, and the outstanding variability of fly ash as a material. As demonstrated below, N_r provides a physical basis – which the Class C and Class F designation lacks – to link composition to glass structure and to subsequently link to the performance of high volume fly ash-cement blends, thereby enabling a means to estimate the suitability of a given fly ash as a cement replacement agent.

2.5 Experimental results and discussion

2.5.1 *Bulk compositional characterization of fly ashes*

Figure 3(a) represents the content of total CaO in each fly ash based on XRF analyses only (*i.e.*, not corrected for crystalline phases), with the boundary between high and low calcium fly ashes demarcated at 20 % by mass (approximate) as stipulated by the ASTM C618 classification of Class C and Class F fly ashes. A reduction in CaO content also implies a reduction in network ratio (see Figure 3b). This is expected, as calcium is the primary network modifier in the glassy phase of fly ashes. Unlike the CaO content, which is but a *single indicator*, the network ratio accounts for other network modifiers and formers, while excluding any CaO contained in the crystalline phases.

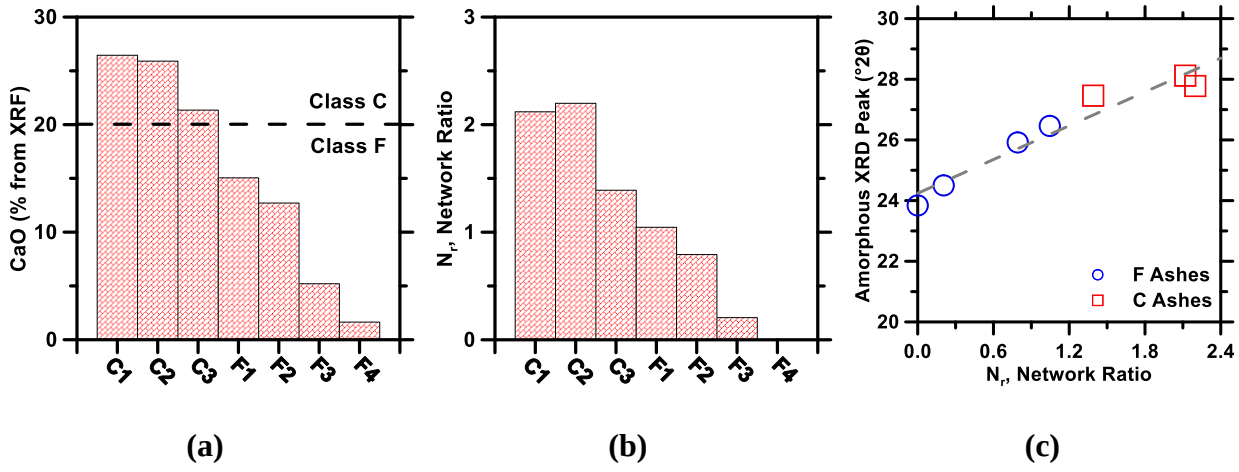

Figure 3: Fly ash features in terms of: (a) total CaO content, (b) N_r, and (c) the amorphous peak position as a function of N_r for the different fly ashes. Precision and bias in the data in (a) are reported in Reference [33]. Calculations in (b) have the uncertainty propagated from the uncertainty in composition shown in Table 1,[33] which is on the order of 5 %. In (c), the XRD peak values have a standard deviation of approximately 0.5° based on three replicate scans; in this and all other plots showing a trend line, the lines were produced by ordinary linear regression merely to indicate the approximately linear trends. The equation for the line shown in (c) is of the form:

$$(2\theta)_{peak} = 1.857 \cdot N_r + 24.241$$

To examine the validity of the network ratio as an atomic level descriptor of fly ash structure and performance, it is compared in Figures 3(c), and Figure 4 to the XRD peak ("hump") position, the density—as initially suggested by Diamond (see References [54,55])—and the glass transition temperature (T_g, °C) of the glassy phases in fly ash. The position of the amorphous hump is thought to be a good indicator of glass structure, as it represents short range order of the glass.[43] Higher 2θ angles represent a smaller (average) interatomic spacing suggestive of a denser atomic structure. This is especially noted for Class C fly ashes wherein the 2θ position of the hump increases with N_r – indicative of the glass structure being "stuffed" with network modifying calcium atoms. The idea of densification of the fly ash structure with increasing N_r is evidenced through the fly ash density. This can be caused by (a) the shrinkage of the atomic interstices during glass formation due to incorporation of network modifying cations, (b) the formation of partially ordered domains

near the modifier ions that improve packing density, or (c) a gain in molar mass associated with the "stuffing" of certain species (*e.g.*, calcium) into the glass structure. It should be noted that part of the power of using network ratio as a descriptive parameter lies in its ability to provide a continuous scale for differentiating fly ashes compared to the binary Class C and Class F designations.

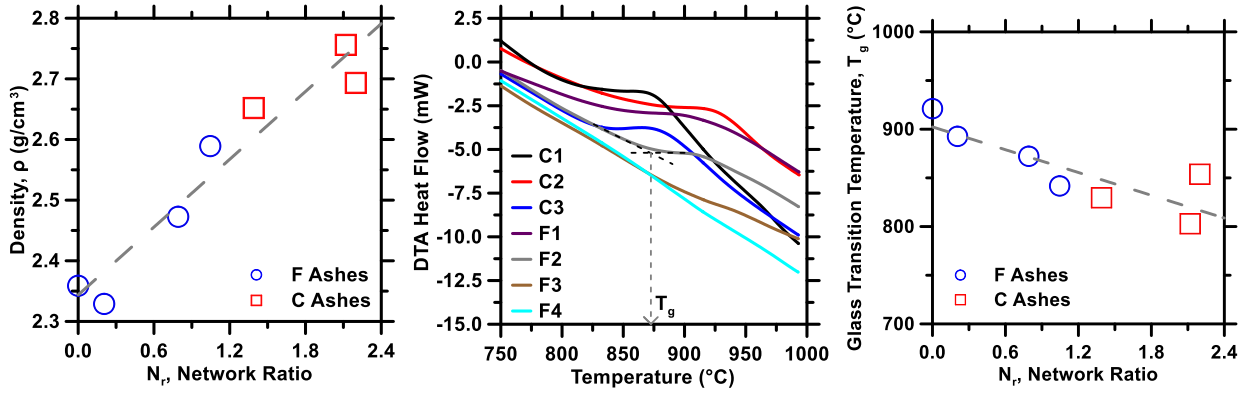

(a) **(b)** **(c)**

Figure 4: (a) The correlation of the network ratio (N_r) with fly ash density, (b) DTA heat flow profiles that are used to determine the glass transition temperature by the slope-intercept method,[47,57] and (c) the correlation of the glass transition temperature with the network ratio. Here and throughout the paper, the relative standard deviation in density and T_g is approximately 1 % and 5 %, respectively, based on three measurements of different samples of the same fly ash. In (a), (c), and all other plots showing a trend line, the lines were produced by ordinary linear regression merely to indicate the approximately linear trends. The equation for the lines shown in (a) and (c) are of the form:

$$\rho = 0.186 \cdot N_r + 2.344$$

and

$$T_g = -39.017 \cdot N_r + 902.339$$

The T_g indicates the temperature at which a glass transitions to its liquid state and exhibits a viscosity of 10^{12} Pa·s and a sharp change in heat capacity.[47,57] Glasses can be distinguished from other amorphous compounds in that they continuously convert to a liquid upon heating, rather than re-crystallizing and then melting.[47] Glass transitions can occur across a range of temperatures, and

thus, variations may emerge, depending on the heating rate and method of assessment. This is because, in glasses, the variation of interatomic potential energies causes "disordered melting" to occur during glass transitions. Analysis of T_g shown in Figure 4(b-c) suggests that, in general, T_g decreases with N_r. This is because the increasing abundance of network modifiers in the glass reduces its structural connectivity, facilitating its glass transition at reduced temperature.

Indeed, in alkali-aluminosilicate glasses that are present in fly ash, T_g decreases linearly with increasing network modifier content in the range $0.01 < M_2O/SiO_2 < 0.6$.[61] This results from the formation of a small fraction of Q_2 units (silicate tetrahedra with two non-bridging oxygens), which facilitate viscous flow via continuous breaking and reforming of Si-O-Si bonds and are "lubricated" by the alkali cations associated with each Q_2 group.[62] However, these effects also show a clear composition dependence as T_g (for a fixed modifier content, mole basis) increases with the ionic radius of the species that induces steric constraints to viscous flow.[63] A notable exception to the general trend of decreasing T_g with network modifier content is raised by the potential presence of high-calcium aluminosilicate glass, i.e., with low levels of silica.[64] Depolymerization of the 3D network of Ca-Si-Al ternary glasses is noted to lower glass transition in the range of intermediate silica contents for $CaO/Al_2O_3 \approx 1$ (mole basis), with a minimum of approximately 30 % SiO_2 content (mole basis). But, at higher CaO/Al_2O_3 ratios (R), the low levels of silica present in the glass act to increase the T_g. Such issues create irregularities in systems containing significant portions of "high-calcium" glass (*i.e.*, the Class C fly ashes).

To quantify these deviations from the trend in glass transition, the difference between the trend line and the glass transition temperature for each fly ash is plotted against the bulk CaO/Al_2O_3

ratio (R, mass ratio) of their glass phases in Figure 5(a). Fly ash glasses with bulk R values of less than about 2.5 fall approximately along a line, generally showing negative deviations for overcompensated glasses (R>1) and positive deviations for undercompensated glasses (R < 1)[v]. But the same behavior is not exhibited by several of the Class C fly ashes. This plot confirms the expected re-elevation of T_g reported for high R values at low silica contents,[64] and they also reveal a limitation of network ratio for predicting the properties of low-silica glasses.

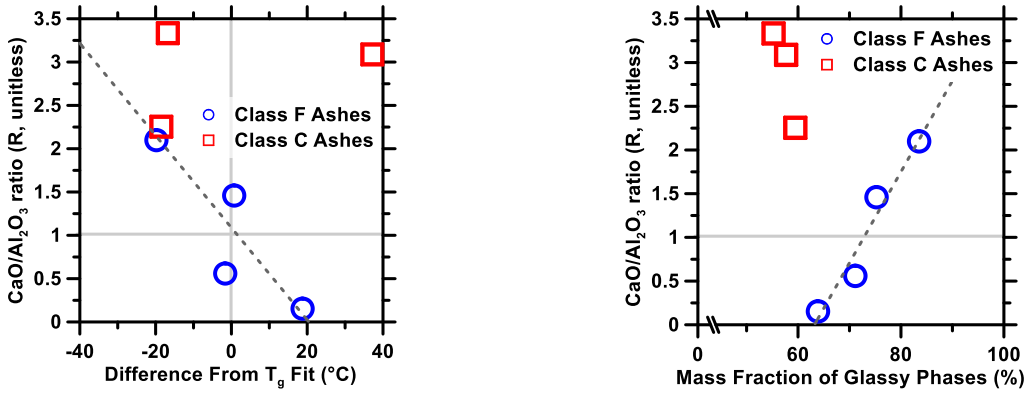

Figure 5: The CaO/Al_2O_3 ratio, R ("compensation ratio"), as a function of: **(a)** deviation from the T_g correlation of Figure 4(c), and **(b)** mass fraction of glassy phases present in each fly ash.

The R values are also strongly correlated with the mass fraction of glassy phases in the Class F fly ashes (Figure 5b). This appears to show a real distinction between Class F and Class C ashes. Furthermore, the observed correlations in Figure 4 are strongest for fly ashes in which the glass forming ability increases uniformly with R in Fig. 5(b) (*i.e.*, Class F ashes), as evidenced by increased abundance of glassy phases. As a general rule for fly ashes, alkaline-earth modifiers such as calcium should exert a weaker influence on T_g than alkalis such as sodium. Similarly, T_g should

[v] Due to the error accrued in measuring glass transition, and its deviation from the correlation obtained with network ratio in Figure 4(c), the line displayed in Figure 5(a) is a simplification for illustrative purposes only.

generally decrease with increasing modifier content (*i.e.*, increasing network ratio). These expectations are in fact confirmed by the monotonic decrease of T_g with network ratio for fly ashes spanning the range of Class F and Class C classifications in Figure 4(c).

2.5.2 *Spatially resolved compositional characterization of fly ashes*

SEM-EDS techniques have been used to provide quantitative insights into the distribution of amorphous phases in fly ash.[31,32,65] This has been achieved by clustering methods, whereby compositional maps are segmented into manually and automatically defined groups. Groups observed to have compositions corresponding to well-defined crystalline phases are assigned as such, while the remaining groups represent broad groupings of glassy phases. Following this approach, the overlaid elemental maps of Ca, Si, and Al (see Figure 6b) were used to assign clusters manually (*e.g.*, a green cluster for high Si phases, and a blue cluster for high Al phases). Furthermore, multispectral image segmentation, using both the backscatter images and element maps, was performed as in Reference [[32]], using automated clustering to minimize operator bias; the results are shown in Figure 6(c). These clusters were assigned compositions based on their coincident point map data. The geochemical data (GCD) kit was applied to compare the outcomes of an alternative algorithm for automated clustering that used only compositional point map data.[51]

Figure 7 shows a side-by-side comparison of manually constructed clusters (Fig. 7(a)) with those generated by automated grouping using the GCD kit algorithm (Fig. 7(b)). Both methods generally produce similar groupings for a given fly ash. Quartz was the only crystalline phase resolved by either the automated multispectral method or the automated GCD kit algorithm. EDS point compositions also indicated the presence of compositions corresponding to crystalline phases such

as anhydrite, periclase, and tricalcium aluminate, but neither of the automated methods were able to separate these. This difference may be caused by limitations in spot size, which precludes the accurate detection of sub-micrometer phase boundaries. This would make it difficult to detect phases, such as mullite, that may be microcrystalline, cryptocrystalline, or partially or wholly embedded in otherwise amorphous particles.[66] These issues especially confounded the analysis of three of the seven fly ashes (C1, C2, and F1) where high levels of heterogeneity within particles did not permit a direct comparison between the point mapped composition and cluster grouping.

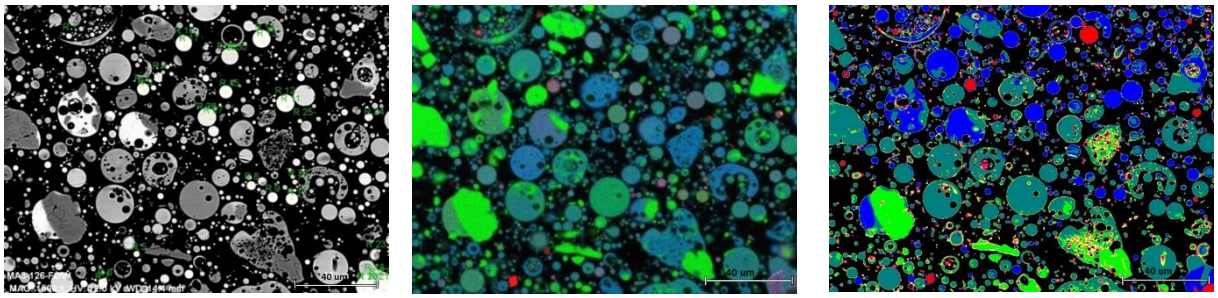

(a) **(b)** **(c)**

Figure 6: Representative micrographs for Class F fly ash F3 acquired using scanning electron microscopy (SEM) showing: (a) backscatter image, (b) X-ray dispersive spectroscopy element maps with color coded images overlaid where Ca is shown as red, Si as green, and Al as blue, and (c) the multispectral image segmentation mask, with the color codes shown below.

High Alkali Glass | Medium Alkali Glass | Low Alkali Glass
Quartz | High Calcium Glass | Medium Calcium Glass | Low Calcium Glass

For the fly ashes F4, F3, and C3, the point-mapped compositions of amorphous phases could be partitioned among five distinct compositional ranges, three of which correspond to aluminosilicate glasses differentiated by calcium content: “Low Ca Glass” (< 15 % CaO on a mole basis), “Medium Ca Glass” (15 % to 35 %), and “High Ca Glass” (35 % to 60 %). Two other glass categories, labeled as “Amorphous Silica” and “Low Al Glass” in Fig. 7(c), contained low concentrations of non-silicate components. The compositional groups are arbitrarily defined here,

as they were in a study by Durdzinski et al.,[65] and were selected to illustrate trends across a range of modifier contents in a simple manner (*i.e.*, corresponding to three calcium aluminosilicates and two high-silica glasses), as shown in Figure 7(c).

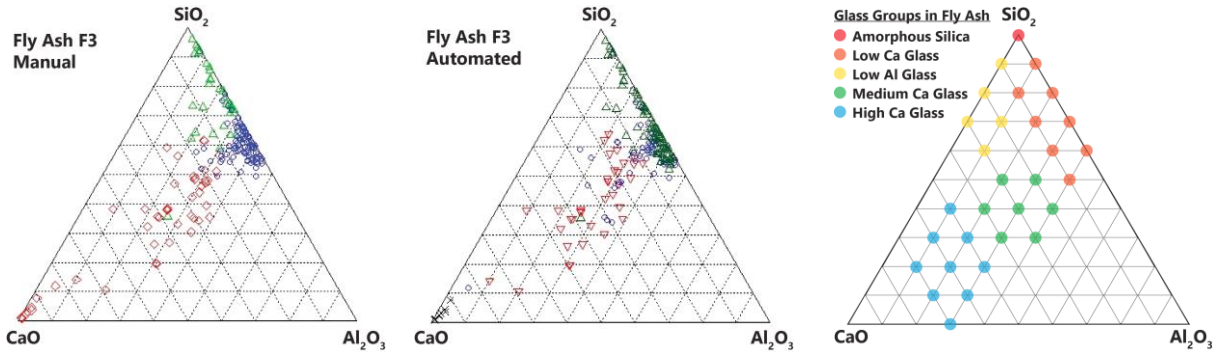

(a) **(b)** **(c)**

Figure 7: Representative ternary diagrams showing: **(a)** manually selected clusters from the elemental maps and **(b)** clusters identified by the automated GCD-kit algorithm. The red symbols indicate calcium-rich phases, green indicates silicon-rich phases, and blue indicates aluminum-rich phases. **(c)** A ternary diagram showing compositional groupings of the glass phases across all the fly ashes, as defined from multispectral clustering.

The relative abundances of these amorphous phases are shown for all the fly ashes in Figure 8. The main difference between Class F and Class C fly ashes is the partitioning between low and high calcium aluminosilicate glasses. In a typical Class F fly ash, most of the calcium aluminosilicate (CAS) glass has a low Ca content. The Class C fly ash has equally distributed proportions of the low, medium, and high calcium glass compositions. Figure 8(b) reclassifies the combination of thetwo high-silica glasses into three categories based on their total alkali concentration. The notable increase in alkali-aluminosilicate glass in the ash C2 (Figure 8(b)) reflects the concentration of calcium in the high-Ca CAS glass. These trends suggest a compositional threshold that may be related to the glass forming ability of the low and high calcium

mineral-glass assemblages in these fly ashes (see also Figure 5(b)). Such thresholds are worthy of further study due to their implications on glass structure in the CAS ternary system.[64]

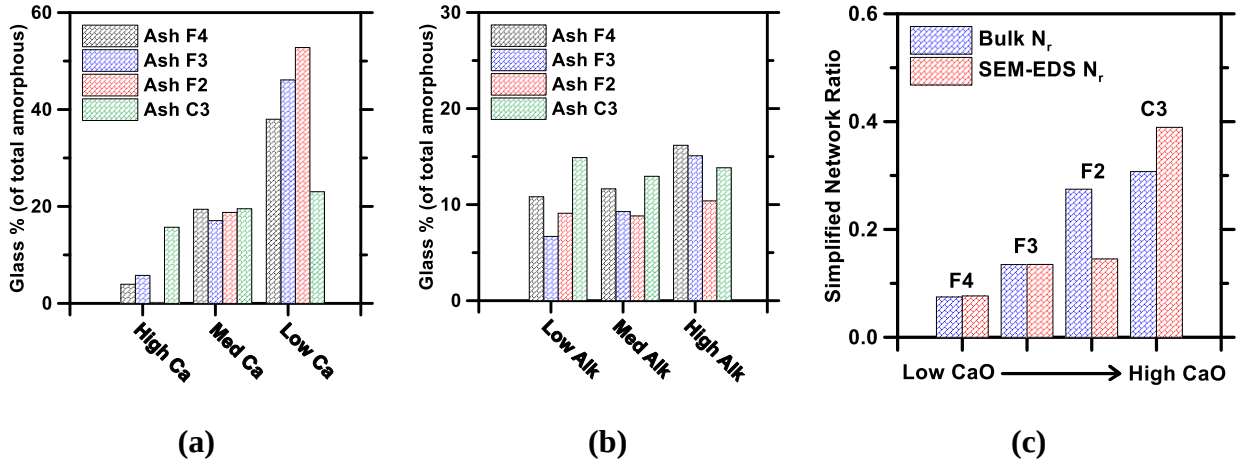

Figure 8: The composition and abundance of fly ash glasses for (a) calcium aluminosilicate (CAS) glasses and (b) alkali aluminosilicate (AAS) glasses, as a percentage of total amorphous material, and (c) a comparison between the simplified network ratio calculated using the EDS composition segmented groupings and calculated from the XRF-XRD data. The relative standard deviation in glass contents for CAS glasses and AAS glasses are on the order of 8 % and 6 % respectively, based on analyses of at least three different SEM fields of view at the same magnification.

To avoid underestimating the influence of modifier ions in glass fractions associated with the low silica calcium aluminate glass, as discussed in Section 1.5.1, considerations of charge compensation by aluminum cation association are excluded to define a simpler network ratio, which is the ratio of network modifier ions to network forming ions,

$$\text{Simplified } N_r = \frac{X_{Ca} + X_{Mg} + X_K + X_{Na}}{X_{Si} + X_{Al}} \qquad \textbf{Equation (2)}$$

This formula is only useful for comparisons between local and bulk network ratio trends and cannot be used in the predictive capacity of the network ratio as outlined by Equation (1). For

comparison to simplified network ratios calculated from the bulk XRF-XRD data, the average of the simplified network ratios of the individual glass fractions, weighted by the mass fraction of each glass, was calculated by applying a linear rule of mixtures approach. The network ratio calculated in this manner shows good agreement, to within 5 %, with that calculated from bulk XRF-XRD results for low calcium fly ashes F3 and F4 (see Figure 8(c)), but the agreement diminishes with increasing Ca-content. This is mostly due to the inability of the SEM-EDS method to accurately resolve all crystalline phases present, especially in Class C fly ashes, as well as the inability of the network ratio to account for aluminum as a modifier ion in the case of calcium aluminate glass. However, the reasonable match between the full and simplified network ratios for the low-Ca glasses supports the use of this kind of averaged N_r for fly ashes. A remaining question is how accurately the network ratio of the combined glassy phases in a fly ash may reflect the behavior of each individual glassy compound. This is a complex issue, particularly between CAS and AAS glasses, but glasses with a high N_r should have the greatest influence on reactivity and performance metrics relative to the other glassy phases (see Section 1.5.3).

2.5.3 *Relating fly ash composition to reactivity and engineering performance*

The network ratio (N_r) was related to the reactivity and development of engineering properties by monitoring heat release during hydration and strength development.

Kinetics of early hydration: Figure 9(a-b) shows heat flow profiles for representative fly ash-cement blends. Reaction rates proceed similarly for all fly ashes at low OPC replacement levels. Significant differences begin to emerge, however, at higher replacement levels (> 20 % fly ash by mass), more so for the Class C than Class F ashes, assumed to be due to the disruption of the

aluminate-sulfate balance of the binder. Disruptions of this nature can be caused, for example, by additional C_3A and/or anhydrite contained in the fly ashes, and are known to impact set time.[30] As such, issues arise from the crystalline compounds in the fly ash and may be addressable via mixture proportioning;[67] discussion here is limited to assessing the reactivity of the glassy phases.

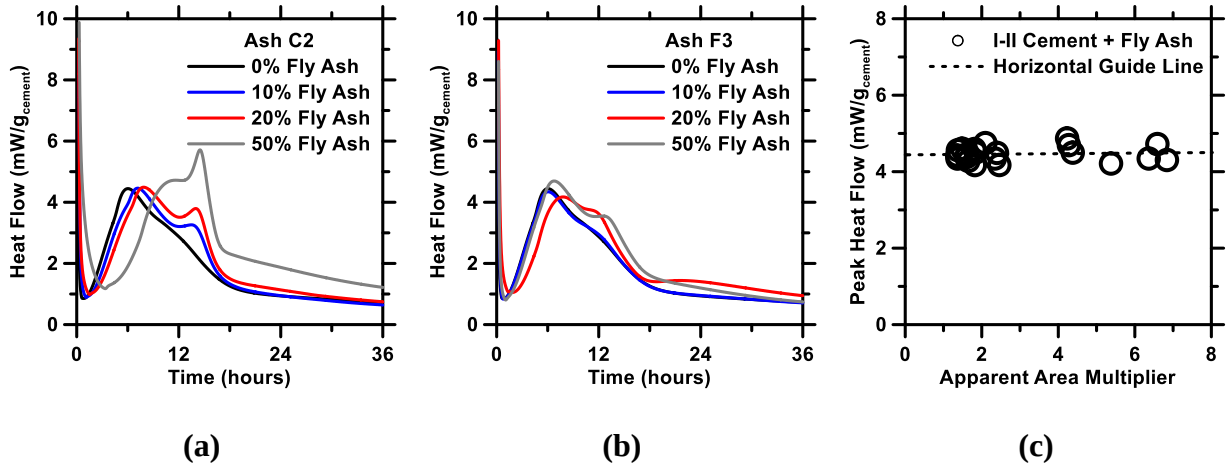

Figure 9: Representative isothermal calorimetry profiles for fly ash-cement blends for: (a) fly ash C2 and (b) fly ash F3. (c) The heat release rate at the main hydration peak as a function of the area multiplier (AM). The maximum range in the data for six replicates of plain Type I/II portland cement, at any time between 1 h and 72 h, was approximately ± 2 % of the signal.

For fly ash replacement levels ≤ 20 % by mass, the reaction rate is altered only slightly if at all, with no filler effect being noted.[52] Typical enhancements in reaction rates caused by fine fillers can be correlated to the area multiplier, *AM*, a parameter that accounts for the increase in surface area according to

$$AM = 1 + \frac{r \cdot SSA_{filler}}{(100 - r) \cdot SSA_{cement}}$$ **Equation (3)**[52]

where r is cement replacement level (mass %), and SSA_{filler} and SSA_{cement} are the specific surface areas of the filler (fly ash) and cement respectively (m^2/kg). Despite a small delay in hydration (see right-shift with increasing fly ash dosage, Figure 9(a-b)), the heat release rate at the main hydration peak is essentially independent of the additional surface area (Figure 9(c)) provided by the fly ash. This suggests that these fly ashes do not produce a surface area increase induced filler effect.

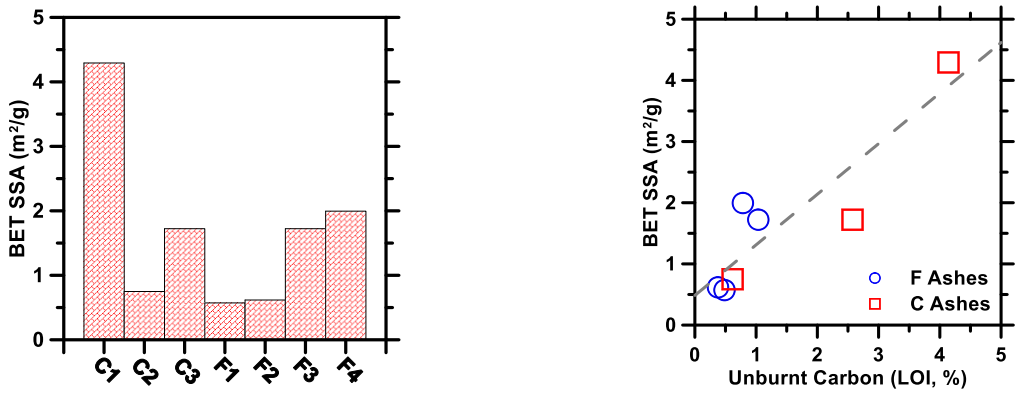

(a) **(b)**

Figure 10: (a) The BET surface area of the different fly ashes, listed from left to right in order of decreasing CaO content, and (b) the BET surface areas as a function of the LOI of the fly ashes. The relative standard deviation in surface area values by BET is approximately 5 % based on three replicate measurements of the same powder sample, and the uncertainty in LOI is ± 0.1%. The equation of the line in (b) is of the form:

$$SSA_{BET} = 0.827 \cdot LOI + 0.485$$

Indeed, fly ash surface area assessed by N_2 sorption shows little dependence on fly ash composition (Figure 10(a)); although it shows correlation with the loss on ignition (LOI) of the fly ash assessed by thermogravimetric analysis (Figure 10b). Thus, fly ash surface area is likely most influenced by unburnt carbon content, especially since thermogravimetry (not shown) indicates significant decomposition between 500 °C and 850 °C,[68] and since calcite, which also would decompose in

this temperature range, was not detected by XRD. Indeed, the literature discloses that the surface area associated with only the inorganic constituents in fly ash is on the order of 700 m^2/kg, as assessed by N_2 sorption and BET analyses.[69] This specific surface area is similar to the surface area of OPC measured under the same conditions, which explains the lack of a fly ash-induced filler effect.

The attribution of excess surface area to unburnt carbon has two implications. The first is that fly ashes with high specific surface area may be relatively less compatible with chemical admixtures, since the adsorption capacity of unburnt carbon is known to affect air entraining admixtures.[69] The second implication relates to fly ash's capacity to function as a mineral filler.[52] The "true" surface area of inorganic particles in the fly ashes is approximately 650 m^2/kg, as estimated from the fly ashes C2, F1, and F2, which exhibited no decomposition between 500 °C and 850 °C and hence likely do not contain appreciable unburnt carbon. This surface area is approximately the surface area of the OPC, approximately 640 m^2/kg. The similarity in surface area explains why fly ash replacements of OPC result in minimal changes in OPC reaction rates.

The absence of a filler effect could be due to the fly ash particles not providing preferential nucleation sites for cement hydrates, but microscopy data in the literature suggest hydrates on fly ash surfaces.[31,70] As no filler effect is expected for these ashes, neither a retardation nor an acceleration of hydration seems to be linked to phase chemistry or amorphous content of the ash itself. This suggests that fly ash and its glassy phases, apart from issues of sulfate-aluminate compatibility, probably act as chemically inert filler during early hydration.

Heat release and strength development: Numerous studies have shown that heat release during hydration is strongly correlated to strength development.[52,53] In agreement with this concept, Figure 11(a) shows so-called strength-heat correlations from 1 d to 28 d for two fly ashes. The measured heat is normalized by a mixture's water content (mass or volume basis, assuming the density of water, ρ_w =1000 kg/m^3), as the initial water content is a measure of the initial porosity of the system (i.e., the space that can be progressively filled by the reaction products to achieve better properties).[53,71,72] However, ranking a given fly ash's suitability as a cement replacement agent must be done under conditions that can distinguish fly ash performance. To do so, it is necessary to consider mixtures in which the behavior is not dominated by the OPC fraction. I light of that, a 50 % by mass fly ash replacement for OPC is used in the following analysis to permit suitable clarification of fly ash behavior. The network ratio is first compared to cumulative heat release at 7 d for mixtures with 50 % fly ash replacement. The 7 d interval is used because the glassy compounds in a fly ash typically only begin to react after extended exposure (> 3 d) to alkaline environments.[50] The heat release at 7 d correlates well with the network ratio (N_r, see Figure 11(b)), providing a direct link between glass structure and reactivity of the fly ashes. Again, we emphasize that this correlation is not as evident either at lower fly ash dosages or at earlier ages of hydration due to the superimposed/transitional kinetic response of mixtures in which the reaction and strength development are dominated by the OPC fraction.

Returning to trends in the strength-heat correlation of Figure 11(a), the rate of strength gain, once it begins, varies among the different fly ashes. This is significant as it permits the slope of this correlation trend line to be used as a metric of a fly ash's performance. In fact, the slope of the strength-heat correlation, which is a measure of the strength contribution of a unit reaction of the

fly ash, is inversely correlated with the network ratio, as is shown in Figure 11(c). This inverse correlation is significant as it implies that, on average, low-Ca glasses (*i.e.*, silicon rich glasses like those in Class F fly ashes) contribute more effectively to strength gain for a unit level of chemical reaction. This is postulated to be caused by the formation of C-S-H with lower Ca/Si (molar ratio),[73] since the mechanical properties of the C-S-H compounds improve with decreasing Ca/Si. Compressive strength generally decreases with increasing cement replacement by fly ash, but the data in Figure 11(c) suggest that Class F ashes would be a superior OPC replacement compared to Class C fly ashes if the reactivity of the former could be improved. Taken together, the correlations of the network ratio to measures of fly ash glass structure and to cementitious binder performance support its use as a figure of merit to rank a fly ash's suitability as a partial replacement for OPC in concrete binders.

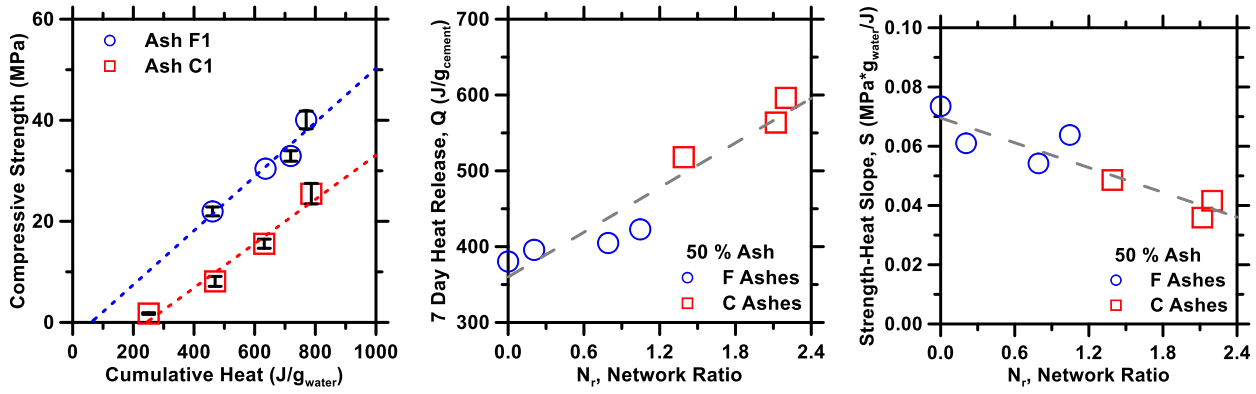

(a) **(b)** **(c)**

Figure 11: (a) Representative compressive strength-heat release correlations for a Class F (F1) and a Class C (C1) fly ash (± 10% uncertainty in compressive strength values based on measurement of three replicate samples); (b) the 7-d heat release as function of the network ratio (relative standard deviation is 2 % based on six replicates); and (c) The slope of the strength-heat correlation plot as a function of the network ratio (relative standard deviation based on three replicates is approximately 10.2 %). The equations in (b) and (c) are of the form:

$$Q_{7\ days} = 98.227 \cdot N_r + 360.050$$

and

$$S = -0.014 \cdot N_r + 0.070$$

2.6 Chapter summary and Conclusions

This chapter describes an approach to link the composition of a fly ash to its structure, reactivity, and performance as a cement replacement agent. Detailed characterizations of fly ash composition are used to assess a new parameter known as the network ratio (N_r, unitless), which is based on the atomic and structural features of aluminosilicate glasses. The network ratio, a self-consistent parameter that can be calculated by multiple means, is correlated to well-recognized indicators of glass structure, such as density and T_g, across a range of fly ashes. Contrary to expectation, the fly ashes examined here do not induce a filler effect because their specific surface areas are approximately equal to that of the cement used herein. For mixtures containing sufficient fly ash, at least 50 % by mass herein, the heat release after 7 d of hydration is linearly (positively) correlated to the network ratio. For the same mixtures, the slope of the strength-heat correlation also is linearly (negatively) correlated to the network ratio. Significantly, Ca-poor fly ashes are more effective, for a given amount of reaction, at contributing to strength gain than their Ca-rich (Class C) counterparts. The network ratio is therefore a robust parameter that links the composition, structure, reactivity of fly ashes across Class C and Class F designations. This provides an improved physical basis to understand the reactivity of fly ashes as potential cement replacement agents.

Chapter 3: Topological controls on the dissolution kinetics of glassy aluminosilicates

3.1 Chapter scope

At current levels of global production, the manufacture of ordinary portland cement (OPC) is responsible for nearly 9% of anthropogenic CO_2 emissions.[3] To mitigate the impacts of such CO_2 emissions, it is common to replace OPC with supplementary cementitious materials (SCMs) such as fly ash in the binder fraction in concrete, a process commonly known as "dilution".[74,75] Substantial efforts have been made to characterize fly ash compositions, and their potential impacts on the engineering properties of cementitious formulations,[76–78] but far fewer studies have attempted to establish the origins of, and to quantify fly ash reactivity.[79–81] Establishing the origin of and controls on fly ash reactivity is prerequisite knowledge, needed to rank different fly ashes in terms of their suitability as an OPC replacement agent.[82] Towards this end, we provide new insights into the atomistic origins of fly ash reactivity so as to place its use, on an informed scientific basis. The outcomes of this chapter are applicable not only to fly ash, but more generally to other amorphous/glassy SCM's including slags, clays, and natural pozzolans.

3.2 Materials and methods

Seven commercially available fly ashes were chosen to encompass representative yet abundant U.S. fly ashes (and coal streams) with a range of glassy compositions. This includes three Class C ("CaO-enriched") fly ashes, and four Class F ("SiO_2-enriched") fly ashes, as classified by ASTM C618.[33] The fly ash compositions are detailed below (see Tables 1-2). The bulk oxide composition of each fly ash was determined using X-ray fluorescence as per ASTM D4326[33] (XRF, see Table 1 in Chapter 2). To establish the fly ash mineralogy, quantitative X-ray diffraction (QXRD, see

Table 2 in Chapter 2) analyses were carried out on powdered fly ash samples, using ZnO (about 20 mass %) as an internal standard. The samples were mounted in metallic (zero-background) holders, and the surface gently textured to minimize preferred orientation errors. A Bruker D8 Advance diffractometer in a θ-θ configuration using Cu-Kα radiation (λ = 1.54 Å) was used to scan the powder samples on a rotating stage between 5° and 70° (2θ) in continuous mode with a six second step time. X-ray structure information for relevant anhydrous and hydrated crystalline phases was sourced from the literature or standard databases to provision a custom *control-file* for Rietveld refinement that was carried out using TOPAS©.

The *average* dissolution rate of each fly ash was measured at (25 ± 3 ºC, i.e., based on the maximum temperature variation over a 24 hours period) using vertical scanning interferometry (VSI).[83] By directly tracking the evolution of the surface topography with time, VSI accesses the true dissolution rate of a dissolving solid.[23,83–85] The technique features significant advantages over methodologies that are based on analysis of solution compositions because it is unaffected by complexities including: 1) inaccurate knowledge of the solid's surface area,[85] 2) metastable barrier formation that may be relevant to glassy systems,[86] 3) incongruent dissolution,[87] and/or 4) ion adsorption on dissolving or reacting surfaces.[88–90]

The dissolution rates were quantified using a so-called raindrop procedure,[vi,83] by which the solution's pH and composition remain essentially constant over the course of the experiment. The

[vi] It should be noted that in the rain-drop procedure, while the "bulk" undersaturation of the solution with respect to the dissolving solids will change negligibly, the reduction in undersaturation of the solution may be more substantial in close proximity (i.e., within the first 10 nm) of the solid surface. While this may result in undersaturation gradients within a "static" water-drop; i.e., close-to, and further away from the dissolving solid surface. While artifacts of this nature are indeed unavoidable, they are expected to be more important for solids that dissolve under transport control (i.e., when the rate of transport of ions away from the particle surface is rate-controlling; i.e., for faster dissolving solids) than interface control (i.e., when the transport of ions is not rate limiting in dissolution; i.e., for slower dissolving solids such as silicates).

typical l/s (liquid-to-solid mass ratio) used was on the order of 50,000 for a contact time of approximately 5 min per raindrop cycle for a minimum of 15 cycles. The solvent was evacuated using a compressed N_2 stream between raindrop cycles. Solution pH values[vii] of 10, 12, 13, and 14.3 were achieved using reagent grade sodium hydroxide (NaOH), dissolved in 18 MΩ ("MilliQ") water.

Since the dissolution studies were carried out on technical fly ashes, i.e., those containing both glassy and crystalline compounds (see Table 2 in Chapter 2), data collection was initiated after the first 15 minutes of "contact time" (dissolution period). This was necessary to permit dissolution and exhaustion of the fast dissolving crystalline compounds such as C_3A whose dissolution, if it were to occur simultaneously, may have interfered with observations of dissolution of the glassy compounds. It should be noted that the dissolution of compounds such as quartz, which is often present in the highest abundance amongst crystalline compounds (e.g., see Table 2 in Chapter 2), is not a concern as quartz dissolves three orders of magnitude more slowly than the glassy phases present in fly ash,[23] and hence will not impact the results. The average composition of each ash's glassy components was established by subtracting the XRD-based compositions of crystalline compounds from the XRF-based total (simple) oxide compositions.

[vii] Solution pH values have been verified by experiments measuring the extent of carbonation (via pH) over time. Over the duration of experiments conducted herein, no appreciable carbonation (within error) was observed.

The structure of the glassy phase, assumed homogeneous,[viii] was then assessed via molecular dynamics (MD) simulations. Due to the limited availability of realistic inter-atomic potentials (that can encompass any combination of elements), the compositions of the simulated systems were restricted to the following oxides: SiO_2 and Al_2O_3 (network forming species), and CaO, MgO, Na_2O, K_2O (network modifying species), while maintaining the molar ratios among these oxides as equivalent to the native fly ashes. The glasses were created using the conventional quenching method at zero pressure in the *NPT* ensemble as follows: (1) heating the system at 4000 K to lose the memory of its initial configuration, (2) cooling to 300 K at a cooling rate of 1 K/ps, (3) relaxing the structure at 300 K for an additional 100 ps, and (4) equilibrating the structure for an additional 100 ps in the *NVT* ensemble for statistical averaging.[91] The simulations were performed with a timestep of 1 fs using the interatomic potential parametrized by Teter.[92] This potential has been extensively studied and has been shown to predict realistic glass structures.[93–95] The simulations agree broadly with previous simulations studies[91,96] on three main points. First, Si is four-fold coordinated by oxygen atoms. Second, alkali and alkaline-earth cations tend depolymerize the network by forming non-bridging oxygen (NBO) species. Third, Al is four- or (rarely) five-fold coordinated and tends to repolymerize the network by consuming the NBOs, or by creating three-fold "tri-cluster" oxygen (TO) species.

The structure of the simulated glasses is analyzed within the framework of topological constraint theory (TCT).[97,98] TCT captures the relevant features of the atomic topology which have an

[viii] It is well known that the glassy phase of fly ash is not homogenous. This assumption excludes any effects which may arise from a heterogeneous mixture of glassy and crystalline phases as is present in fly ash. However, the glass is assumed homogeneous because (a) it has been shown that an average homogeneous glass provides an accurate representation of the physical response of fly ash materials during dissolution occurring during cement hydration[10], and (b) such an assumption is necessary to facilitate characterization of fly ash in a manner which is both feasible and relevant (i.e. characterization which may be conducted on an as-received fly ash, and reflect said ash's behavior) .

important influence on the kinetics of dissolution,[23] while filtering out less relevant structural details. This is achieved by simplifying complex atomic networks into simple mechanical trusses, wherein the nodes (the atoms) are connected to each other through constraints (i.e., the chemical bonds): the radial bond-stretching (BS) and angular bond-bending (BB) constraints. Rather than relying on unproven guesses regarding the connectivity of the atoms, the total number of constraints per atom (n_c) was directly determined from the MD simulations by following an established methodology,[96,99] wherein the radial and angular excursions of the neighbors of each atom are computed to enumerate the BS and BB constraints, respectively.

In agreement with previous studies,[96,99] the following observations are made: (1) Si atoms create four BS constraints with the neighboring O atoms and five BB constraints (to define the tetrahedral environment); (2) Al atoms create four or five BS constraints, but do not possess any BB constraints; (3) alkali and alkaline-earth species create a composition-dependent number of BS constraints with the surrounding NBOs, but do not show any BB constraints; and (4) bridging oxygen (BO) atoms form one BB constraint (three in the case of TOs). Finally, in accordance with previous observations,[23] charge-compensating alkali or alkaline-earth cations (i.e., those in the vicinity of Al, which do not create any NBOs) are excluded from this enumeration as they do not contribute to the rigidity of the network.

3.3 Results and discussion

Figure 12(a) shows the measured dissolution rates of all the different fly ashes as a function of the solution pH. As expected, the dissolution rate increases with pH because greater hydroxyl concentrations (activities) facilitate hydrolysis of silicate networks.[100] Surface speciation induced

by the presence of sodium (i.e., from NaOH which exchanges with the protons of terminal silanol groups[89]) may somewhat enhance fly ash dissolution rates,[89] but this effect should be relatively constant across all fly ash compositions because it is related solely to the concentration of added sodium. In the high pH range used in this study, the dominant driving force for dissolution arises from the elevated activity of $[OH]^-$ ions, which induces nucleophilic attack of tetrahedral $[SiO_4]^{4-}$ or $[AlO_4]^{5-}$ units present in the glassy compounds in fly ashes.[101] The plot also shows that the dissolution rates of the lower-calcium Class F fly ashes (F1 through F4) are lower than those of the higher-calcium C ashes (C1 through C3) across the entire range of caustic pH's considered.

Figure 12(b) shows that the measured dissolution rate of all the fly ashes in this study decreases exponentially with the number of constraints, n_c, for a given pH. The same behavior was observed recently for a range of silicate-solids by Pignatelli et al.[23]. Indeed, for a given pH the dissolution rates of all fly ashes lie along the same line. It should be noted that decreases in dissolution rate generally correspond to lower concentrations of calcium in the fly ash, but this is not a strong correlation. For example, fly ashes F2 and F3 both have lower CaO content and greater dissolution rates than F1, as shown in Figure 12(a). The lack of a stronger correlation between calcium content and dissolution rate strongly suggests that the predominant C and F classifications of fly ashes as established by ASTM C618 are insufficient to predict or rank an ash's relative reactivity. Rather, a "network ratio" parameter, as described in Chapter 2,[82] or the number of topological constraints per atom as shown in this study, are more reliable indicators of ash reactivity. Apart from the ASTM C618 based "C or F" classification of fly ash, the glass science community has often expressed the properties of glasses in terms of their degree of depolymerization, NBO/T, which represents the number of non-bridging oxygens per tetrahedral unit.[82,102] However, Pignatelli et

al. have recently shown that even NBO/T is not always reliable indicator of glass dissolution behavior.[23]

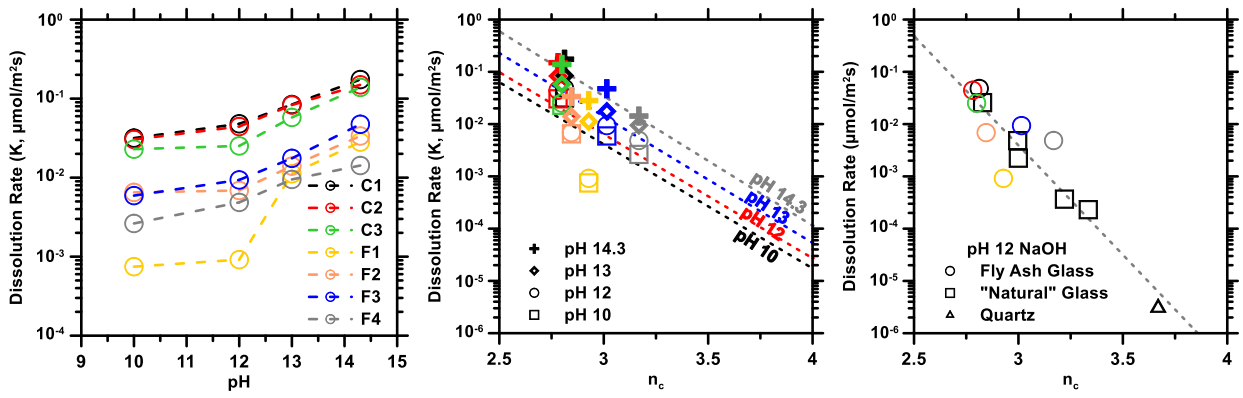

Figure 12: The dissolution rates of the seven fly ashes as a function of: (a) solution pH, and (b, c) the number of constraints per atom (n_c, unitless) calculated by MD simulations. For consistent comparison between solids of different compositions, the dissolution rates are expressed as moles of O_2 dissolved per m^2 of surface area per second. The data in (b, c) is fitted using exponential functions. The color of datapoints in (b) correspond to the legend presented in (a) to indicate which fly ash each point represents, while the symbol shape corresponds to the solution pH, with squares, circles, diamonds, and crosses representing pH 10, 12, 13, and 14 respectively. The data in (c) includes dissolution rates for silica and quartz, as well as glassy equivalents of albite, jadeite, nepheline, and sodium silicate glass (see [23,101,103]). The exponential functions represent an Arrhenius-like expression of the form: $K = K_0 \exp(-n_c E_0/k_B T)$, where: K is the dissolution rate in µmol/m^2•s, K_0 is the intrinsic dissolution rate constant in µmol/m^2•s, E_0 is the energy required to break a unit atomic constraint (E_0 = 23.9 kJ/mole in Figure 1c), k_B is Boltzmann's constant in kJ/mol•K, and T is the thermodynamic temperature in degrees K.

The dissolution rate is shown to be correlated to the rigidity (n_c) of the whole network, including the alkali and alkaline-earth cations, rather than the rigidity of only the aluminosilicate "skeleton" network. This suggests that while dissolution kinetics are dominated (rate-limited) by the rate of breakage of the higher energy Si/Al–O bonds, the rate of breakage of the lower energy bonds that are created due to the presence of the network modifiers is also relevant; albeit to a smaller extent.

This is in agreement with the observations of Boolchand et al. who noted that glass hardness was correlated with the rigidity of the overall network, including the contributions of modifier atoms.[104] A significant observation in Figure 12(b) is that, in spite of being composed of a myriad of glassy compounds of disparate compositions, the "average" dissolution rate of the glassy fly ash solids, and the associated number of atomic constraints, reliably represent fly ash behavior. As remarked earlier, this observation supports the work of Chapter 2, wherein a network ratio parameter was formulated to demonstrate that relative fly ash reactivities can be ranked based on knowledge of their average glassy compositions.[80,82,105]

When the fly ash dissolution rates shown in Figure 12(b) are plotted along with additional dissolution rate data for glassy silica, quartz, and several aluminosilicate glasses including albite, jadeite, nepheline and sodium silicate glass (denoted as "Natural" glass; see Figure 12c[23,103,106]) – the exponential dependence of dissolution rate on n_c is preserved[ix]. Significantly, the regression of these data using an exponential function of the form $K = K_0 \exp(-n_c E_0/RT)$ reveals that the averaged, or apparent, activation energy needed to break a unit atomic constraint is $E_0 \approx 23.9$ kJ/mol. This assessment of E_0 for heterogeneous fly ash glasses that are produced during an uncontrolled, complex quenching process is similar to that observed for stoichiometric and fully-compensated aluminosilicate glasses and pure silicate solids ($E_0 = 25.5$ kJ/mol).[23] In support of the commentary above, the small difference in magnitudes suggests that the constraint rupture energy is largely controlled by the network formers (e.g., $[SiO_4]^{4-}$ and/or $[AlO_4]^{5-}$ species); albeit with smaller but relevant contributions that arise from the presence and distributions of modifier atoms.

[ix] To reiterate, the assumption that the glass in fly ash consists of a single homogeneous phase is at the root of poor quality of this exponential dependence among the seven fly ashes. Interferences from either (a) uniquely reactive or unreactive glasses from among the heterogeneous distribution present, and/or (b) uniquely reactive or unreactive crystalline phases may both result in higher or lower dissolution rates (measured on the bulk fly ash, not the isolated glass) than those predicted by number of atomic constraints calculated for an assumed homogeneous glass.

This indicates that, to a first approximation, fly ash dissolution rates are primarily dictated by the activation energy for bond rupture amongst $[SiO_4]^{4-}$ or $[AlO_4]^{5-}$ units;[106] wherein the activation energy is described as $E_a = n_c E_0$.[23] This dependence of dissolution rates on the number of atomic constraints is shared by other rate processes in glasses, including ion diffusion and conduction, and suggests that the three typical mechanisms involved in glass dissolution, namely hydration, hydrolysis, and ion exchange, can be formalized within a consistent thermodynamic framework which encompasses the material's atomic architecture/topology.[23]

3.4 Summary and conclusions

Across a wide range of commercially available fly ashes, the dissolution rates of the glassy constituents are shown to depend on the number of atomic constraints placed on a given atom in the glass network. This constraint dependence of dissolution rates is described by an Arrhenius-like expression that permits determination of the average energy needed to rupture a unit atomic constraint. This rupture energy is on the order of 25 kJ/mole across a range of silicate solids including fully compensated and highly modified glasses, as well as pure silicates (i.e., glassy silica and quartz). Such a dependence of dissolution rates on the number of constraints suggests that rate processes including dissolution, diffusion, and ion conduction all are similarly predicated on the topology of the atomic network. This allows for rationalizing rate phenomena such as dissolution within a consistent thermodynamic framework based on the energy required for bond rupture. This framework also enables a robust way to measure, analyze, and rank fly ash reaction rates as a function of their average glassy compound composition and the atomic topology of the glassy compounds in fly ash. Such understanding is needed to better inform and enhance the use

of fly ash as a supplementary cementitious material (SCM) without sacrificing concrete performance.

Chapter 4: The role of the network-modifier's field-strength in the chemical durability of aluminoborate glasses

4.1 Chapter scope

Aluminoborate glasses are often used as low-temperature specialty sealing materials,[107] and have also been considered for the immobilization of radioactive waste.[108] Alkaline earth aluminoborates have been developed specifically for use in energy storage systems or biomedical devices on account of their insulating and corrosion-resistant properties.[109–112] Of primary concern in such applications is the chemical durability of the glass, which may dictate the practical lifetime of these products. Although the dissolution rate of borate glasses is known to strongly depend on the B_2O_3 mole fraction, the addition of Al_2O_3 usually results in an increase in glass durability, while increasing the melting point of such glasses, thereby reducing their processability.[113]

Studies of the local structure of aluminoborate glasses have indicated that boron atoms may exist in either 3- or 4-fold coordinated states, and aluminum atoms in 4-, 5-, or 6-fold coordinated states.[114,115] In such glasses, whose network structure is comprised of more than one type of network forming element, it has been suggested by Brow and Tallant that the structure of the atomic network is sensitive not only to the amount of network-modifying elements (i.e., which may result in a greater degree of de-polymerization) but also on the field strength of the network modifiers (i.e., valence-to-radius ratio), which may result in the formation of highly-coordinated boron and aluminum units.[116] As such, it is anticipated that network-modifying atoms can impact glass durability: (i) directly, i.e., by depolymerizing the network, and/or, (ii) indirectly, i.e., by affecting the coordination number of the network-forming atoms.

The present study elucidates the role of network-modifying cations in altering the structure and chemical durability of aluminoborate glasses, which has remained relatively unexplored thus far. To this end, the structure and aqueous dissolution rates are assessed across ten aluminoborate glasses presenting a fixed nominal composition but with varying network-modifying elements (i.e., Mg, Ca, Sr, and Ba to span a range of modifier sizes and field strengths, as well as mixtures of Li-and-Mg to consider ions having similar size but different field strengths). The architecture of the atomic network of these glasses is described within the framework of topological constraint theory (TCT) which characterizes disordered structures of glasses in terms of the "number of constraints placed on an atom in the network" (n_c) – a metric that has been shown to capture the effect of the atomic structure on the chemical durability of glasses.[23,85,98,117–121] It is demonstrated that changes in the field strength of network-modifying atoms affect the glasses' atomic topology, and hence their chemical durability (i.e., proxied by aqueous dissolution rates).

4.2 Materials and methods

The glasses were synthesized by preparing stoichiometric proportions of powdered raw materials, following oven drying at 110°C for 25 hours to remove any water. The raw materials consisted of aluminum oxide (Sigma Aldrich, 99.5%), boric acid (Prolabo, 100%), magnesium carbonate (Acros Organics, 95%), calcium carbonate (Prolabo, 95%), strontium carbonate (Sigma Aldrich, 99%), barium carbonate (Sigma Aldrich, 99%), and lithium carbonate (Merck, 98.5%). The homogenized powder mixtures were gradually added to a platinum crucible maintained at 1000 to 1400 °C until fully melted, after which they were held at this temperature for approximately one and a half to two hours depending upon the melt viscosity. The melts were quenched by pouring onto a metal plate and compressed into uniform slabs with a piston. The glass sections were then

annealed for 20 minutes at their glass transition temperatures (T_g[122]), followed by gradual cooling at 2 °C/min. The density of each glass was measured by a buoyancy method, i.e., by weighing each coupon in air and ethanol for ten repetitions. The composition of each glass was verified by acid digestion followed by inductively coupled plasma optical emission spectroscopy (ICP-OES, see Table 3).

The particle size distributions (PSD) of the glass powders were measured using laser diffraction spectroscopy carried out on suspensions of the powders in isopropyl alcohol. The suspensions were sonicated prior to measurement to disperse powders to primary particles. The uncertainty in the light-scattering analysis was determined to be approximately ±3% based on triplicate samples. The glass powders are similar in terms of their specific surface area, as determined from their particle size distributions assuming spherical particles (see Table 3).

Finally, to evaluate changes in the bonding environment of network-forming elements, Magic Angle Spinning Nuclear Magnetic Resonance (MAS-NMR) was used to calculate the average coordination numbers of aluminum and boron species (see Table 3).[122–124] ^{27}Al MAS NMR measurements were made using a commercial spectrometer (Agilent DD2), with a 16.4 T narrow-bore superconducting magnet, and a 3.2 mm Agilent MAS NMR probe for a sample spinning at 20 kHz. The ^{27}Al resonance frequency was 182.34 MHz, and the radiofrequency pulse width was 0.6 microseconds, equivalent to a $\pi/12$ tip angle. The recycle delay between each of 400 acquisitions was four seconds. The data was processed without any extra line broadening, and the ^{27}Al shift was referenced to aqueous aluminum nitrate at 0.0 ppm. ^{11}B MAS NMR measurements were made using a commercial spectrometer (Agilent VNMRs), with a 11.7 T wide-bore

superconducting magnet, and a 3.2 mm Varian T3 MAS NMR probe. The glass samples were powdered and packed into 3.2 mm zirconia rotors, for a sample spinning at 20 kHz. The ^{11}B resonance frequency was 160.34 MHz, and the radiofrequency pulse width was 0.6 microseconds, equivalent to a $\pi/12$ tip angle. The recycle delay between each of 400 acquisitions was four seconds. The data was processed using commercial software (VnmrJ), without apodization, and with frequencies referenced to aqueous boric acid at 19.6 ppm.

Table 3: The molar composition, surface area, density, the average coordination numbers (CN) of Al and B, and the number of constraints per atom (n_c) for the ten aluminoborate glasses synthesized herein.

Glass ID	**1**	**2**	**3**	**4**	**5**	**6**	**7**	**8**	**9**	**10**
B_2O_3 (mol %)	56.0	55.0	55.0	55.8	54.4	55.9	53.2	52.7	53.4	52.6
Al_2O_3 (mol %)	20.1	19.9	19.7	19.3	20.0	19.3	19.3	21.5	19.6	19.9
Li_2O (mol %)	0	4.9	9.9	12.3	14.8	19.7	27.4	0	0	0
MgO (mol %)	23.9	20.2	15.3	12.8	10.8	5.0	0	0	0	0
CaO (mol %)	0	0	0	0	0	0	0	25.8	0	0
SrO (mol %)	0	0	0	0	0	0	0	0	27.0	0
BaO (mol %)	0	0	0	0	0	0	0	0	0	27.5
Surface area (m^2/g)	0.14	0.09	0.12	0.13	0.11	0.12	0.12	0.10	0.11	0.14
Density (g/cm^3)	2.45	2.41	2.38	2.34	2.33	2.29	2.23	2.48	2.82	3.10
CN of Al [122–124]	4.84	4.81	4.73	4.68	4.60	4.46	4.33	4.49	4.26	4.14
CN of B [122–124]	3.16	3.17	3.18	3.19	3.18	3.19	3.18	3.16	3.20	3.18
constraints (n_c) [122–124]	3.25	3.20	3.15	3.12	3.11	3.04	2.98	3.19	3.04	3.02

To assess chemical durability, the dissolution of each glass was followed in a pH 12 NaOH solution maintained at 25 ºC at a surface area to solution volume ratio (SA/V) of approximately 1000 m^{-1}. The suspensions were gently agitated over the course of the experiments. The far-from-equilibrium conditions utilized are designed to preclude an approach to saturation and formation of precipitates, i.e., to measure dissolution rates that reflect the composition and structure of the glass surface along. The solvent was sampled after 0.5, 1, 2, 6, 24, and 168 hours by extracting 6 mL of

solution by syringe, filtering it through a 200 nm filter, and diluting the solution by a factor of three times in a 5% (by volume) HNO_3 matrix.

The diluted and acidified samples were stored at 5 ºC for several hours (i.e., in general < 6 hours) until the time of measurement. Before analysis, the solutions were homogenized by agitation. The abundances of B, Al, Li, Mg, Ca, Sr, and Ba were measured using inductively coupled plasma optical emission spectroscopy (ICP-OES, Avio 200, Perkin Elmer). Each element was measured sequentially, with the majority of the elements being measured using axial view, followed by Li, Mg, and Sr being measured using radial view. Argon was used as a purge gas, with a sample flow rate of 1 mL/min with three replicate measurements being carried out per solution. The *initial* dissolution rate for a given element was determined from the slope of a concentration-time curve from zero to two hours, normalized by the initial surface area of the glass. Since Mg release was not observed from the glasses, the residual solids were analyzed for the presence of magnesium hydroxides or carbonates using simultaneous thermal analysis (STA 6000, Perkin Elmer), wherein the mass loss of the sample contained in an alumina crucible was measured during heating from 35 ºC to 980 ºC at a heating rate of 10 ºC/min in the presence of a ultra-high purity (UHP) nitrogen stream. The absence of characteristic decomposition peaks for both magnesium bearing, and any other phases, confirmed that the absence of magnesium in solution was not due to the precipitation of Mg-bearing solids, but rather due to its retention within the glass structure.

Following previous studies wherein the dissolution rate was correlated to the number of topological constraints per atom,[23,85,98,117–121,125,126] the effect of the atomic topology on the dissolution kinetics for the aforementioned glasses was quantified by hand calculation from

available coordination state data. Topological constraints comprise (i) the radial bond-stretching (BS) constraints and (ii) angular bond-bending (BB) constraints that maintain bonds and angles fixed around their average value, respectively.[96] Here, the following assumptions were used to compute the number of topological constraints per atom (n_c): (i) in order of decreasing preference, the network-modifying cations tend to charge-compensate the aluminum species, charge-compensate the boron species, and create some non-bridging oxygen atoms,[127] (ii) for the covalent bonds of the network-forming atoms, the number of BS and BB constraints is given by $r/2$ and $2r-3$, respectively, where r is the coordination number of the atom,[97] and (iii) due to their largely ionic bonds (i.e. non-directional character), the network-modifying species do not experience any BB constraints.[96] Besides these assumptions, two constraints enumeration schemes were tested, namely, by considering (i) the rigidity of the whole network and (ii) the rigidity of the skeleton aluminoborate network (i.e., wherein network-modifying species are not considered).[104]

4.3 Results and discussion

4.3.1 *Dissolution kinetics*

Figure 13(a) shows the release of boron – i.e., the primary network-forming element in the glasses studied herein (see Table 3) – from two representative alkaline earth aluminoborate glasses upon dissolution. Fast initial dissolution is observed, followed by a slowdown over time (see Figure 13a). This decay in the dissolution kinetics is not expected to originate from a feedback from the solution (i.e., approach to equilibrium).

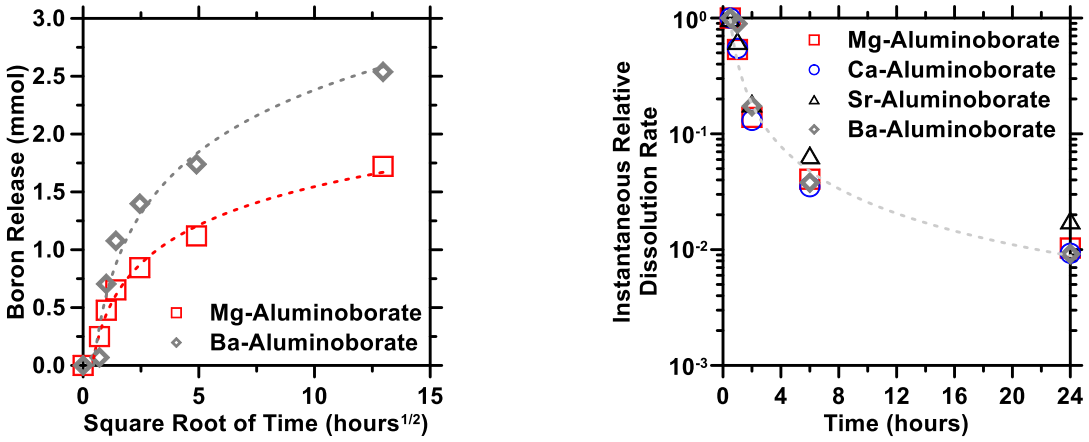

(a) **(b)**

Figure 13: (a) The amount of boron released from two representative alkaline earth aluminoborate glasses as a function of time. **(b)** The evolution of the instantaneous dissolution rate (i.e., estimated from the extent of boron release rate between two consecutive time points from Figure 13a) normalized by the *initial* dissolution rate. The highest uncertainty in the measured boron release is on the order of 3% based on triplicate measurements.

Rather, it is postulated that this slowdown in dissolution is produced due to formation of an *alteration layer* (i.e., depleted in network-modifying ions and/or containing molecular water).[128] Such alteration layers, while widely known to form on silicate glass, have also recently been observed at the surface of aluminoborate glass by Kim *et al.*, even in the case of congruent dissolution.[129] Figure 13(b) shows the normalized instantaneous dissolution rate of each alkaline earth aluminoborate glass normalized by the initial dissolution rate. Significantly, it is noted that the relative slowdown in dissolution is similar across all glass compositions. This suggests that the kinetics of dissolution retardation, in time, are unaffected by the type of network-modifying species, but rather, depends on the network formers (Al, B) which are similar across all glass compositions. This suggests that the glass structure may undergo facilitated re-structuring, e.g., as reported by Cailleteau *et al.*[130,131] – although further study regarding the existence and nature of alteration layers in these glasses is yet needed. From a practical standpoint, the fact that all glasses

exhibit a similar decay in dissolution kinetics allows use of the initial dissolution rate as a means of capturing the far-from-equilibrium dissolution kinetics – and allows for a rapid means to characterize and rank the chemical durability of all the glasses examined herein.

4.3.2 *Incongruence of dissolution*

Furthermore, it is observed that the initial dissolution rate increases with the ionic radius of the alkaline earth network-modifying element (see Figure 14a). This suggests that the dissolution rate decreases with increasing field strength of the network-modifying ions (i.e., inversely with their ionic radii).[116,132,133] The nature of the dissolution mechanism can be further examined by determining the degree of congruence (DOC) associated with the release of any element M where, $DOC(M) = K_M/K_B$, where K_M is the normalized release rate of element M (i.e., where M = Mg, Ca, Sr, Ba, and Al, normalized relative to the glass composition) and K_B is the release rate of boron into solution, i.e., a reference state associated with being the primary network-forming element in the glass structure. Expectedly, DOC = 1 indicates congruent dissolution, that is, wherein all the elements leach out a rate equivalent to that of boron; the primary network former.

As shown in Figure 14(b), first, it is noted that aluminum is released from the glass structure at a rate approaching that of boron atoms (i.e., $0.8 < DOC(Al) < 1.4$). This implicitly suggests that aluminum, similarly to boron, serves as a network-former in the glass structure. In the case of the network modifiers, broadly, dissolution remains incongruent such that low field strength species (i.e., having a larger ionic radius) release faster than boron, whereas high field strength modifiers (i.e., with a smaller ionic radius) release slower than boron species. As such, while magnesium species are retained within the glass network, calcium and strontium ions dissolve nearly

congruently relative to boron, while barium is released substantially faster than boron atoms. This scaling between network modifier release rates and field strength is in agreement with the observations of Casey *et al.* wherein the dissolution behavior of alkaline earth orthosilicates was linked to the nature of divalent metal-oxygen bonds.[132] This scaling was found to control the weathering rates of minerals, and to be related with the coordination number of the aluminum atoms therein.[133]

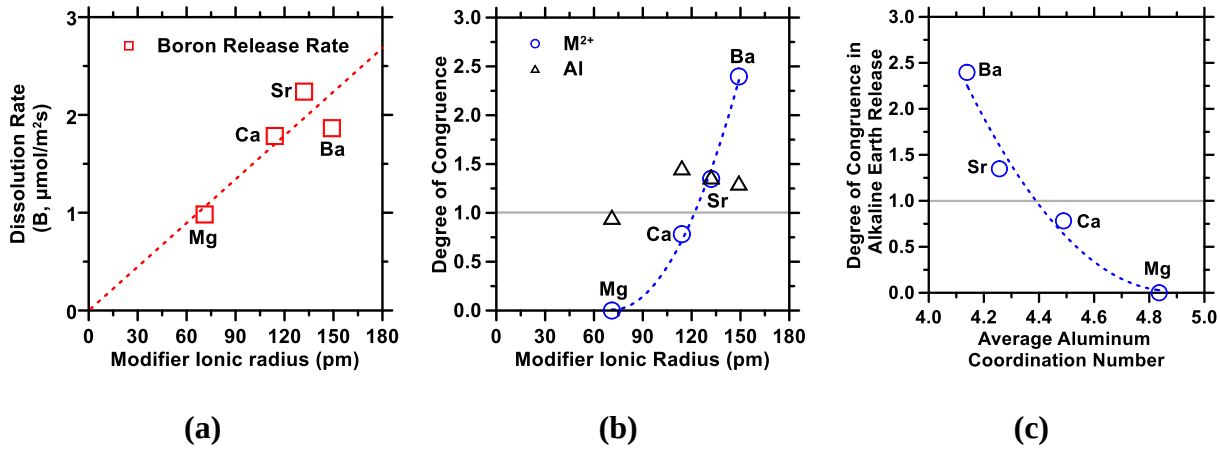

Figure 14: (a) The *initial* dissolution rate of the aluminoborate glasses as a function of the ionic radius of the network-modifying species. **(b)** The degree of congruence (i.e., with respect to the leaching rate of boron atoms; DOC) of aluminum atoms and alkaline earth network-modifying elements. The solid line defines congruent dissolution with respect to boron release rates. **(c)** The degree of congruence (i.e., with respect to the leaching rate of boron) of the alkaline earth network-modifying elements as a function of the average coordination number of aluminum species in the glass structure.

Indeed, as shown in Figure 14(c), the decrease in the degree of congruence of the network-modifiers is closely associated with an increase in the average coordination number of aluminum, i.e., through the transformation of 4-fold coordinated into 5- and 6-fold coordinated Al atoms.[122] These structural changes reflect local-charge models for aluminoborate glass network.[114,115] According to these models, the alkaline earth network-modifiers are expected to preferentially

associate with aluminum network units, with cations exhibiting high field strength tending to result in formation of 5- and 6-fold coordinated aluminum. This suggests that the alkaline earth cations that charge-compensate 5- and 6-fold coordinated aluminum species exhibit lower mobility – i.e., as reflected by their lower aqueous release rates – due to their *more rigid integration* into the glass structure.

4.3.3 *Mixed modifier effects*

The mixed cation Li-Mg glasses considered herein offer a basis to compare chemical durability as a function of the proportion of high field strength modifiers (e.g., Mg) present in a glass composition. As shown in Figure 15(a), first, the dissolution rate (i.e., boron release rate) increases with the fraction of Li cations. A negative deviation from linearity is observed, wherein the dissolution rate remains near-constant at low Li concentrations, and then suddenly increases (see Figure 15a); this appears initially to be a manifestation of the so called "mixed-modifier effect." This response is often noted in glasses comprising mixed modifiers which exhibit properties that are non-additive (i.e., do not follow a rule of mixture type scaling) as a function of their composition, e.g., especially in regards to mechanical behavior and ionic conduction.[134–136]

Once again, these observations can be rationalized by considering the evolution of the average coordination number of aluminum. Indeed, similar to the non-mixed alkaline earth compositions presented above, it is observed that the higher the fraction of 5- and 6-fold coordinated aluminum atoms (i.e., the higher the average aluminum coordination number), the lower the dissolution rate (see Figures 15a and 15b). These observations strongly support the premise that chemical durability (i.e., dissolution rates) could be altered – within limits, e.g., herein the dissolution rates

vary by a factor of ≈2-to-4 times across all compositions (see Figures 14a and 15a) – by adjusting the coordination state of aluminum and exploiting mixed-modifier effects.[116] It is also interesting to note that the presence of highly-coordinated aluminum atoms results in a decrease in the dissolution rate, which may explain the gradual slowdown of the dissolution kinetics over time, since over-coordinated aluminum species are expected, in some cases, to form *in situ* at the glass surface upon the leaching of the network-modifying atoms.[137,138]

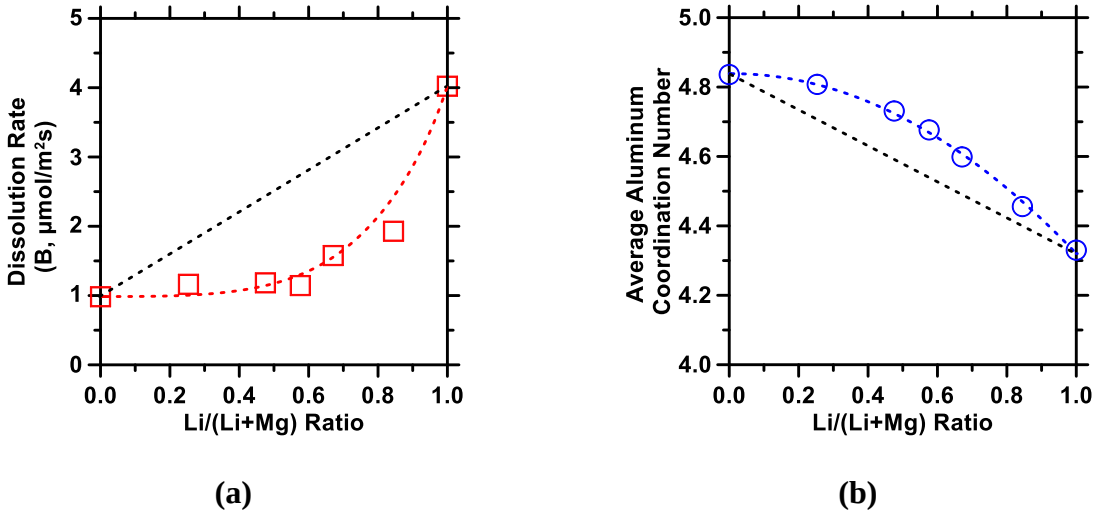

Figure 15: (a) The dissolution rate (i.e., boron release rate) of mixed Li-Mg aluminoborate glasses as a function of the molar ratio, Li/(Li+Mg). **(b)** The average coordination number of aluminum atoms as a function of the molar ratio, Li/(Li+Mg).

4.3.4 *Local atomic topology controls dissolution kinetics*

Figures 16(a-b) show the dissolution rates of all the glasses considered herein (i.e., mixed and non-mixed) as a function of: (i) the number of constraints per atom within the whole network (i.e., by explicitly accounting for the constraints created by the network-modifying cations) and (ii) the number of constraints per atom within the skeleton aluminoborate network (i.e., by only accounting for the dominant constraints created by the network-forming atoms). In both cases, it

is observed that the dissolution rate decreases with an increasing number of topological constraints per atom, in agreement with previous studies.[23,85,98,117–121,125,126] This correlation is explained by the fact that each topological constraint contributes to increasing the local stiffness of the network, which, in turn, results in an increase in the activation energy associated with the hydrolysis of the network-forming atoms (or ion exchange of the network-modifying cations in acidic regimes).[23]

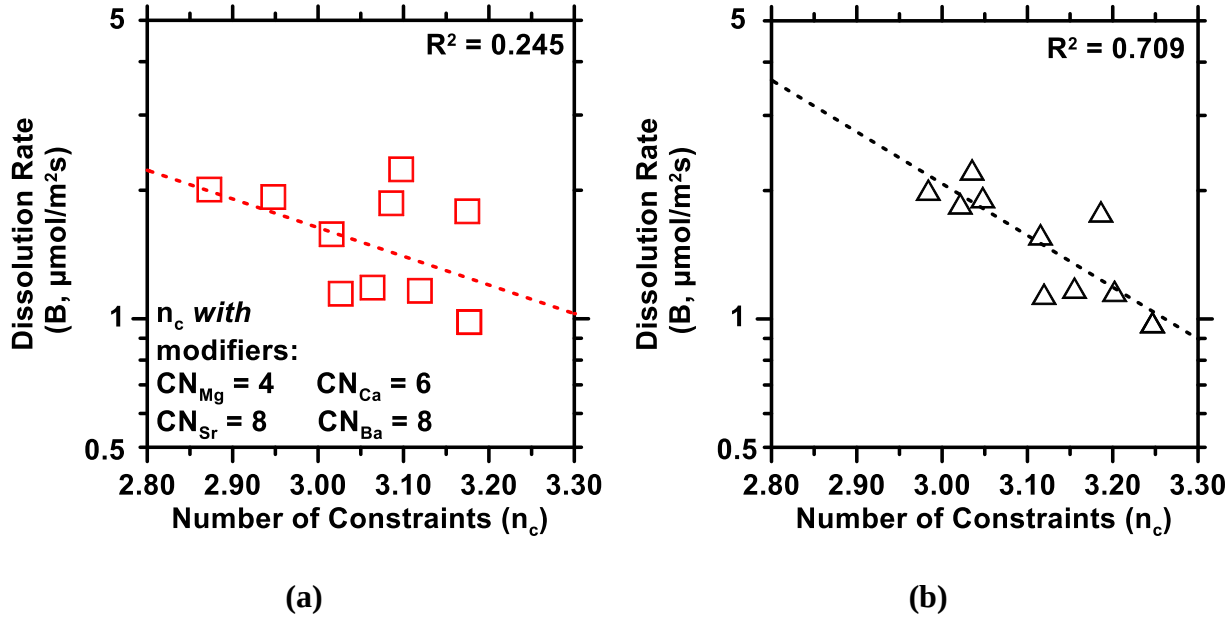

Figure 16: The dissolution rates of all aluminoborate glass compositions as a function of the number of topological constraints per atom while considering: **(a)** the whole atomic network (i.e., all atoms including network formers and modifiers), and, **(b)** the aluminoborate skeleton network (i.e., only including the network forming species; Al and B). The data in (b) is fitted by a function of the form $K = K_0 \exp(n_c E_0/RT)$, where K is the boron release rate (initial dissolution rate), K_0 is an intrinsic dissolution rate constant, n_c is the number of constraints, E_0 is the rupture energy (here, E_0 = 6.9 kJ/mol) associated with a single skeletal constraint, R is the gas constant, and T is thermodynamic temperature.

However, a much stronger correlation is observed between the dissolution rate and the number of constraints per atom by considering the rigidity of the aluminoborate skeleton network rather than that of the whole network (Figure 16b). This suggests that, in the present case, the leaching rate of

elements from the glass is controlled by the topology of skeleton network and remains relatively unaffected by the constraints created by the network-modifying species. This can be understood from the fact that, although topological constraint theory typically attributes an equal weight to all constraints,[139] the constraints created by the modifiers are substantially less significant than those created by the network formers and, therefore, have a lesser effect on the dissolution kinetics.

Finally, it is also worthwhile to note that, when described in terms of the number of constraints per atom, all glasses behave in the similar fashion as their dissolution rate map onto a single "master curve." It should be noted that the slope of this master curve reveals the effective activation energy (i.e., since $E_a = n_c E_0$ as defined within the topological model, while assuming release of the primary network forming element corresponds with the net forward progress of dissolution reactions)[23] required to break a unit constraint, as outlined elsewhere.[23,118] Previously this effective activation energy has been used to demonstrate that the rupture energy per unit constraint depends largely on the network forming elements (i.e., in support of the "skeleton network" constraint calculation), over a wide range of modifier contents. In the current case of the aluminoborate glasses, $E_0 = 6.9$ kJ/mol, a value that is roughly one fourth of that reported for silicate glasses. This is on account of the substantially weaker bonds that form when boron serves as the primary network forming element. This highlights a significant limitation to any approach which seeks to improve glass durability for a fixed nominal composition, i.e., simply by changing the modifier's field strength: benefits achieved by increasing the number of such relatively weak skeleton network bonds via coordination changes are slight.

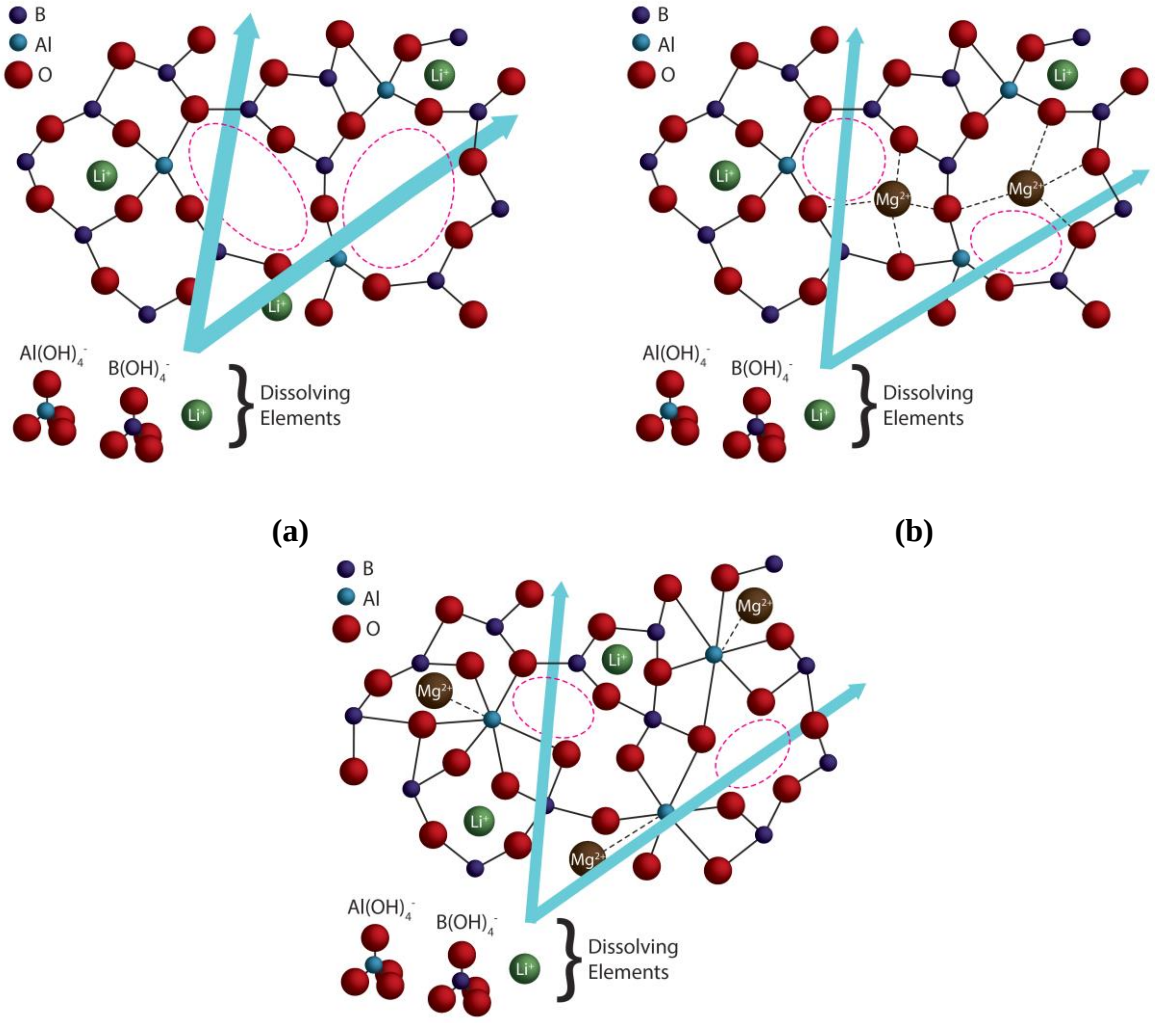

Figure 17: Representative illustrations of: **(a)** a "fast dissolving" lithium aluminoborate glass, **(b)** the "mixed modifier effect" as previously conceived, i.e., with the less mobile Mg modifiers "blocking" release of dissolving elements, and **(c) "**constraint controlled" dissolution wherein the average number of constraints per atom offers an indication of the steric hindrance to element release (dissolution), herein due to the higher coordination number of Al units associated with the Mg modifiers. This clarifies the *indirect* role of modifiers in suppressing dissolution, as a function of induced changes to network topology and their effects on dissolution rate, as described in the text.

The description of dissolution rates using a single "master curve" is significant nonetheless as, in the present case, the network topology allows us to explain the origin of differences in the

dissolution kinetics of mixed and non-mixed aluminoborate glasses within a self-consistent framework, i.e., the number of topological constraints per atom. This also suggests that, in the present case, the mixed modifier effect on dissolution (i.e., the deviation from linearity in the dissolution rate of the mixed Li/Mg glasses; Figure 15a) is an indirect effect, as it arises from a non-linear evolution of the network topology, i.e., a direct function of composition, rather than a change in the dissolution mechanism itself (e.g., see Figure 17).

4.4 Chapter summary and conclusions

This study highlights that network-modifying elements have an indirect, yet crucial effect on the dissolution rate of aluminoborate glasses. Although the chemical bonds created by the network-modifiers do not appear to directly control the dissolution kinetics, the field strength of the modifiers influences the topology of the network-forming atoms (here, primarily the aluminum coordination number), by affecting the average coordination state of aluminum species, which affects the dissolution kinetics. Furthermore, while network modifiers are only able to somewhat improve the durability of *easily hydrolysable* compositions such as aluminoborate glasses, this study provokes more wide-ranging applications wherein coordination changes of the network forming species may be manipulated and controlled to improve chemical durability.[140] This has implications on understanding, explaining and altering glass durability in the case of: (a) exposure to radiation,[141] (b) pressure,[126,142] or (c) post-leaching restructuring of the glass surface.[143]

Chapter 5: Environmental sensitivity of the topological model for aluminosilicate glass dissolution

5.1 Chapter scope

At current levels of global production, the manufacture of ordinary portland cement (OPC) is responsible for nearly 9% of anthropogenic CO_2 emissions.[3] To mitigate the impacts of such CO_2 emissions, it is common to replace OPC with supplementary cementitious materials (SCMs) such as fly ash in the binder fraction in concrete.[74,75] Substantial efforts have been made to characterize fly ash compositions, and their potential impacts on the engineering properties of cementitious formulations,[76–78] but far fewer studies have attempted to establish the origins of, and to quantify fly ash reactivity.[79–81,118] Establishing the origin of and controls on fly ash reactivity is prerequisite knowledge needed to rank different fly ashes in terms of their suitability as an OPC replacement agent.[82] Towards this end, the current study provides new insights into the atomistic origins of fly ash reactivity by extending the topological description of dissolution[23] to synthetic "mimic fly ash glasses" so as to clarify the influences of composition and structure on dissolution of a well characterized and homogeneous equivalent to the often heterogeneous real fly ash materials for which the topological approach was previously investigated.[118] An increased focus is also placed on the potential response of topological constraints, specifically their potential evolution over time, due to relevant environmental conditions such as elevated solution pH and temperature in systems subject to evolving solution compositions (i.e., a distinct step toward a more realistic dissolution environment from previous fixed-composition experiments).[118] The outcomes of this work are applicable not only to fly ash, but more generally to other amorphous/glassy SCM's including slags, clays, and natural pozzolans.

5.2 Materials and methods

Six synthetic sodium aluminosilicate glasses, labeled here as glass #1 through glass #6, were prepared to mimic the composition of the amorphous material found in a representative set of seven U.S. fly ashes used in previous studies.[118,144] The levels of aluminum and calcium in these glasses were varied, respectively, to provide two series of glasses. The first series of glasses, containing varied levels of aluminum (glasses #1-3, Table 4), is intended to approximate high-silica phases most prominent as constituents within typical Class F fly ashes. The second series of glasses, containing varied levels of calcium (glasses #3-6, Table 4), is intended to approximate the overall average composition of several Class F and Class C fly ashes.[144,145]

Reagent grade oxides of silicon and aluminum, and carbonates of calcium and sodium were used as starting materials for the preparation of these glasses. Appropriate quantities of these powdered materials for the specified compositions (Table 4) were weighed on an analytical balance prior to homogenization by grinding for 10 minutes in a planetary ball mill using alumina containers and grinding media. Homogenized powders were heated within platinum-rhodium crucibles in a muffle furnace at a rate of 10ºC/min to a temperature of 1000ºC for de-carbonation, followed by melting at 1400ºC for two hours, excepting glass #6, which required melting at 1600ºC to ensure a fully homogeneous melt. Following melting, the crucibles containing each glass were removed from the muffle furnace and dipped in a container of room temperature water for 30 seconds to ensure rapid quenching, followed by air cooling to room temperature.

Table 4: Proportioning of initial oxide and carbonate materials for glass synthesis, and material properties measured and calculated for each of the six finished synthetic glasses.

	Glass Identification Number					
	1	**2**	**3**	**4**	**5**	**6**
SiO_2 Content (g)	35.57	35.60	35.64	30.04	25.90	19.38
Al_2O_3 Content (g)	0.00	3.78	8.64	8.50	8.79	8.22
$CaCO_3$ Content (g)	3.69	4.15	4.75	9.35	14.5	18.09
Na_2CO_3 Content (g)	6.84	5.19	3.05	3.33	2.76	3.87
Specific Surface Area (SSA, cm^2/g)	3612	3611	3372	3987	4004	3964
Glass Transition Temperature (T_g, ºC)	643	707	847	777	753	682
X-ray Diffraction Peak Position (º2θ)	23.6	22.7	22.5	26.9	29.0	31.0
Number of Topological Constraints (n_c)	2.910	3.129	3.526	3.328	3.299	3.096

After cooling, a small portion of each glass was ground by hand in an agate mortar and pestle and its glass transition temperature was measured using differential thermal analysis, wherein heat flow from the sample contained in an alumina crucible was measured during heating from 35ºC to 980ºC at a heating rate of 10ºC/min. The remainder of each glass was heated within a zirconia container in a tube furnace at a rate of 10ºC/min to its measured glass transition temperature (reported in Table 4) and annealed at that temperature for 30 minutes prior to cooling to room temperature at a rate of 1ºC/min. The glass was then ground to a fine powder in a planetary ball mill for 30 minutes, using alumina containers and grinding media.

To ensure each glass was fully amorphous, X-ray diffraction (XRD) measurements from 5º to 70º 2θ using a Cu K-α source were carried out. Diffraction patterns as presented in Figure 18(a) demonstrate a diffuse peak near 25º 2θ similar to other silicate glasses, showing no characteristic sharp peaks that would evidence crystallization. While nano-crystalline materials may also exhibit

a single diffuse peak, it has been noted that emergence of sharper peaks is to be expected after their annealing, should nano-crystalline materials be present,[146] which was not observed herein.

Particle size distributions (PSD) of each glass powder were obtained by conducting light-scattering measurements on suspensions of a portion of each glass powder in isopropanol. Suspensions were sonicated prior to measurement to disperse powders to primary particles. The uncertainty in the light-scattering analysis was determined to be approximately 6% based on multiple measurements performed on six replicate samples, and assuming the density of the glass to be 2.45 g/cm^3. Cumulative size distributions are presented in Figure 18(b), and demonstrate the similarity in specific surface area (reported in Table 4) between the synthetic ground glasses. Composition and homogeneity of the finished glasses were verified using scanning electron microscopy energy dispersive spectroscopy (SEM-EDS) to measure point compositions across several particles.

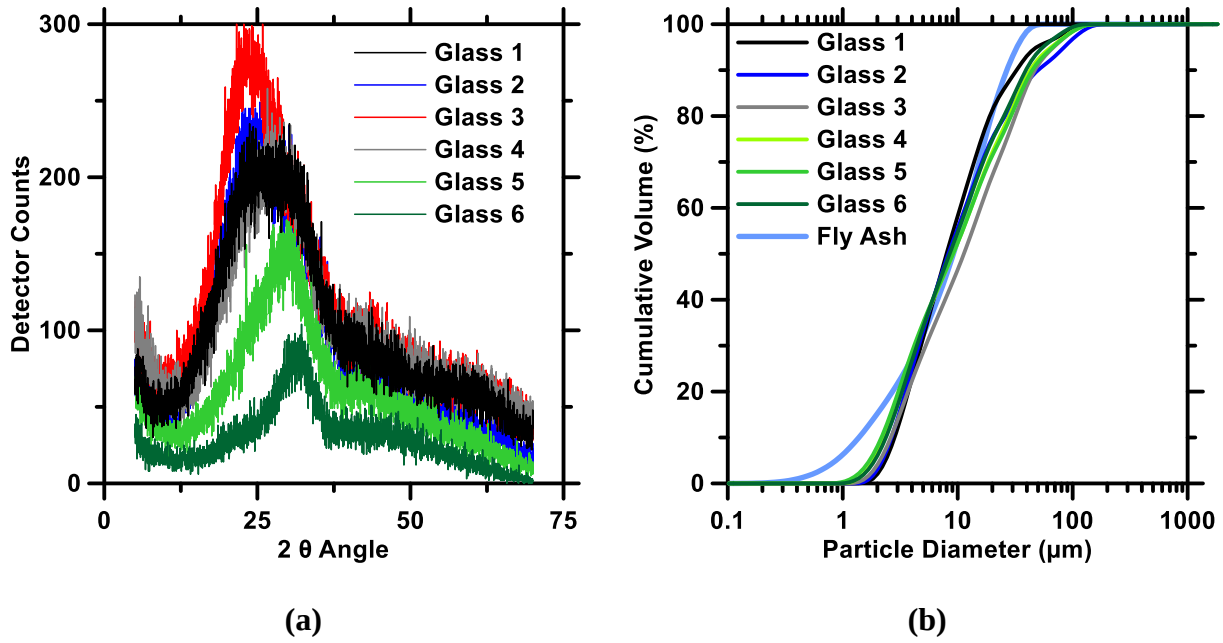

Figure 18: Characterization data for each of the six synthetic glasses showing (a) X-ray diffraction patterns, and (b) particle size distributions. Note that a particle size distribution characteristic of a typical fly ash is also shown for comparison.

Each synthetic glass was dissolved in aqueous solution under a range of pH and temperature conditions. Solutions used were pH 10, 12, and 13 solutions of sodium hydroxide, maintained at 5ºC, 25ºC, or 45ºC. One gram of ground glass was added to 400 mL of the appropriate solution at the given temperature, and agitated gently to ensure homogeneity directly after addition and periodically throughout the course of the experiment. Solutions were stored in temperature-controlled chambers for the duration. Sampling of solutions was conducted prior to addition of the glass, and after 2, 6, 24, 72, 168, and 840 hours, and consisted of extraction of 6 mL of solution by syringe, filtration through a 0.2 micron filter, and dilution by a factor of three times in 5% nitric acid.

Diluted and acidified samples were stored at 5ºC until measurement (no longer than several hours) at which point they were inverted several times to ensure homogeneity of the solution prior to sample loading. Element concentrations of Si, Al, and Ca were measured using inductively coupled plasma optical emission spectroscopy (ICP-OES) in axial view. Testing was conducted using argon purge gas, with a sample flow rate of 1 mL/min on three replicates drawn from the same sample.

The structure of the glassy phase, assumed homogeneous, was assessed via molecular dynamics (MD) simulations. The compositions of the simulated systems were restricted to the following oxides: SiO_2 and Al_2O_3 (network forming species), and CaO, Na_2O, (network modifying species), while maintaining the molar ratios among these oxides as proportionate to the original glasses. MD simulations of the glasses were then created utilizing the conventional quenching method at zero pressure in the *NPT* ensemble as follows: (1) heating the system at 4000 K to lose the memory of its initial configuration, (2) cooling to 300 K at a cooling rate of 1 K/ps, (3) relaxing the structure at 300 K for an additional 100 ps, and (4) equilibrating the structure for an additional 100 ps in the *NVT* ensemble for statistical averaging.[91] The simulations were performed with a timestep of 1 fs using the interatomic potential parametrized by Teter.[92] This potential has been extensively studied and has been shown to predict realistic glass structures.[93–95] The simulations agree broadly with previously published simulation studies[91,96] on three main points. First, Si has a four-fold coordination with oxygen atoms (tetrahedral coordination). Second, alkali and alkaline-earth cations tend to depolymerize the network as a result of forming non-bridging oxygen (NBO) species. Third, Al has four- or (rarely) five-fold coordination (trigonal bipyramidal coordination)

and tends to repolymerize the network by consuming the NBOs, or by creating three-fold "tri-cluster" oxygen (TO) species.

The structure of the simulated glasses is analyzed within the framework of topological constraint theory (TCT).[97,98] TCT captures the relevant features of the atomic topology which has an important influence on the kinetics of dissolution,[23] while filtering out less relevant structural details. This is achieved by simplifying complex atomic networks into simple mechanical "trusses," wherein the nodes (the atoms) are connected to each other through constraints (i.e., chemical bonds): the radial bond-stretching (BS) and angular bond-bending (BB) constraints. Rather than relying on simplifying assumptions regarding the connectivity of the atoms, the total number of constraints per atom (n_c) was directly determined utilizing the MD simulations by following an established methodology,[96,99] wherein the radial and angular excursions of the neighbors of each atom are computed to enumerate the BS and BB constraints, respectively.

In agreement with previous studies,[96,99] the following observations are made: (1) Si atoms create four BS constraints with neighboring O atoms and five BB constraints (the tetrahedral environment); (2) Al atoms create four or five BS constraints, but do not possess any BB constraints; (3) alkali and alkaline-earth species create BS constraints with the surrounding NBOs, but do not show any BB constraints; and (4) bridging oxygen (BO) atoms form one BB constraint (three in the case of TO's). Finally, in accordance with previous observations,[23] charge-compensating alkali or alkaline-earth cations (i.e., those in the vicinity of Al, which do not create

any NBOs) are excluded from this enumeration as they do not contribute to the rigidity of the network.

5.3 Results and discussion

5.3.1 *Number of Constraints Unifies Influence of Network Modifying and Forming Elements*

A basis for the description of glass structure has been established in previous work in two forms: (1) network ratio or degree of de-polymerization, i.e., the number of non-bridging oxygens per tetrahedral silicate or aluminate unit in the glass network (NBO/T),[144] and (2) the number of topological constraints per atom (n_c).[23,118] The former is a fairly commonplace descriptor for glass composition,[58,102] and the latter has recently emerged as a promising descriptor of glass structure and reactivity.[23,118] Both provide useful benchmarks for comparison between glassy materials, and can be determined from other parameters expected to reflect a glass's composition and structure.

One among these available parameters is determined by X-ray diffraction (XRD), in which the position of the diffuse peak, characteristic of the amorphous silicate XRD pattern (see Figure 18a), has long been associated with the short range order of glass.[81,144,147,148] Higher 2θ angles for this peak represent a smaller average interatomic spacing in the glass, as also evidenced by increased glass density.[144] XRD peak position was initially seen as an adequate parameter to describe and compare glasses such as those present in fly ash (e.g., via correlation to NBO/T). However, Figure 19(a) demonstrates that the response of this parameter relative to NBO/T is distinct depending on whether the glass compositions differ in calcium (Ca) or aluminum (Al) content. Addition of a Al, a network forming element, has minimal impact on XRD peak position, as Al is expected to reside

in tetrahedral network sites and will only contribute to increased average interatomic spacing via its nominally longer Al-O bond as compared with the Si-O bond.[91] By comparison, addition of Ca, a network modifying element, has the expected impact to decrease average interatomic spacing by creating additional non-bridging oxygens and filling space in the interstices of the glass network, consequently resulting in higher 2θ peak angles associated with higher-calcium glass. As such, the use of XRD peak position in calculation of unifying compositional parameters for glass, e.g., NBO/T,[144] should be limited to cases wherein compositional changes are largely modifier-induced, e.g., in the case of many fly ashes which vary primarily in their calcium content.

A second parameter that reflects glass structure is glass transition temperature (T_g), the characteristic temperature associated with a glass's transition from solid to liquid state that depends upon the connectivity and inter-atomic potential energies between bonded atoms in the glass.[109] However, NBO/T also fails to present a unified trend with T_g between varied Ca and Al contents studied herein (Figure 19b), which implies that the influence of network modifying and forming elements on T_g cannot be described by inter-tetrahedral-connectivity alone. In this case the number of topological constraints (n_c) provides a more comprehensive metric for connectivity and glass structure, evidencing a single strong correlation with T_g for the glasses with both varied Ca and Al contents (Figure 19c). This highlights an advantage of using number of constraints in unifying description of structure-dependent glass dissolution,[23,118] as it is able to account for influences of both network modifying (Ca) and network forming (Al) elements on chemical structure.

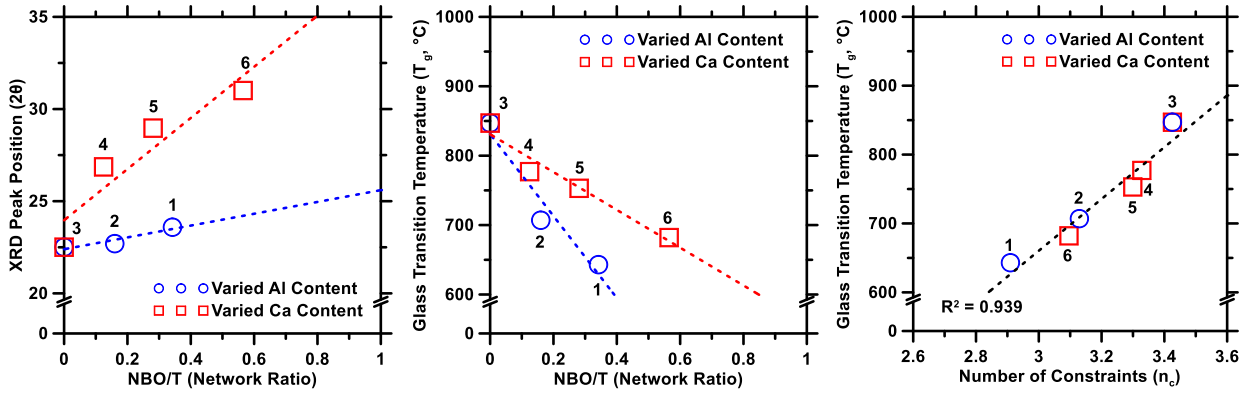

(a) **(b)** **(c)**

Figure 19: Two parameters related to glass composition and structure: **(a)** XRD amorphous peak position, and **(b)** glass transition temperature plotted as a function of degree of de-polymerization (i.e. non-bonding oxygens per silicate tetrahedral unit, NBO/T), as well as **(c)** glass transition temperature as a function of number of topological constraints per network atom (n_c). Each point is labeled with the index number of the corresponding glass as noted in Table 4. Dashed lines shown in parts (a) and (b) are provided to guide the eye, and do not represent physically meaningful correlations.

5.3.2 *Aluminosilicate Dissolution Slows Over Time in Proportion to Aluminum Content*

Dissolution rate of the aluminosilicate glasses studied, as determined from the release rate of silicon (Si, the primary network forming element), slows over time as shown in a few representative element release profiles of Figure 20(a). These profiles can be divided into two periods: "initial dissolution," within the first 24 hours, and "steady-state dissolution," from 24 to 840 hours. For the purposes of this study the division between the two periods is largely arbitrary, and was chosen to establish a basis of comparison for two apparently distinct dissolution regimes, though the phenomenon of slowing dissolution over time *without* an approach to saturation or precipitation has also been observed for several other glass types,[149,150] and has been attributed to the possible formation of altered layers at the glass surface.[130,131,151–153] Dissolution rate was

calculated from Si release during each of the two periods by determining the slope of a linear fit, in the interest of utilizing a quantitative yet simple and mechanism-agnostic approach.

It is interesting to note that "initial" and "steady-state" dissolution rates are roughly proportional for many of the glass types and conditions tested (Figure 20b). In particular, the content of aluminum in each glass appears to give a first indication as to the magnitude of dissolution rate reduction over time. To quantify this trend, the average dissolution rate reduction (similar between temperatures for a given glass type and solution pH) was calculated as the ratio between "steady-state" and "initial" dissolution rates (Figure 20c), and showed that a glass's aluminum content is linearly correlated to the magnitude of change in its dissolution kinetics over time. Notably, these trends are *not* evident when dissolution rate reduction is plotted against either the NBO/T or n_c parameters, despite their well elaborated relation to the *initial* composition and structure of such glasses.[23,118,144] This raises the possibility that, excepting cases in which environmental conditions have been tailored so that dissolution may best reflect this initial state of the glass as in [[23,118]], the evolution of these parameters over time in response to more varied environmental conditions must be considered prior to their successful implementation in modeling late-stage dissolution. Correlations between kinetic changes and compositional variables of the pristine glass (i.e., aluminum content) offer preliminary indication that such a "dynamic n_c" could be determined from knowledge of the glass's initial state, albeit requiring further study to outline which glass alteration mechanisms[130,131] may best apply to the given glass and environment under consideration.

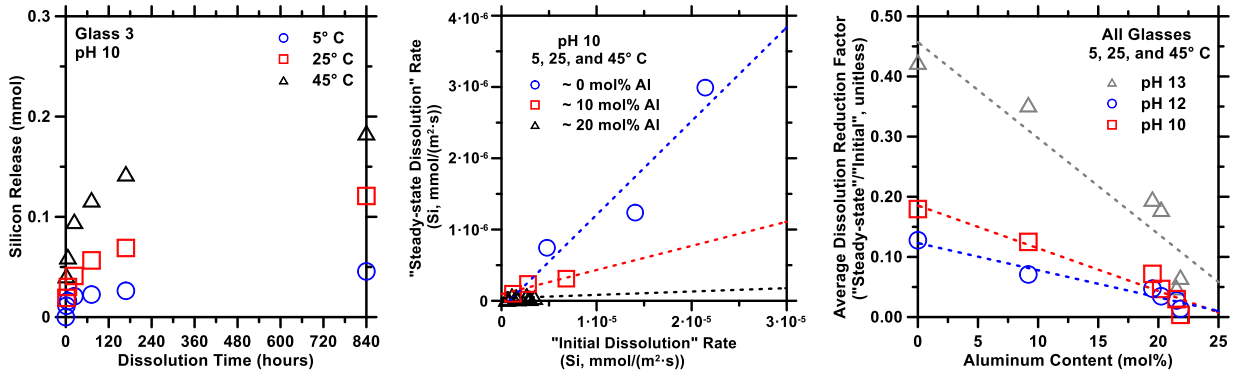

(a) **(b)** **(c)**

Figure 20: (a) Representative silicon release profiles of Glass 3 at pH 10, **(b)** a representative illustration of proportionality between "initial" and "steady-state" dissolution rates for all of the glass types at pH 10, and **(c)** an illustration of the relation between the average dissolution reduction factor, i.e., the ratio of "steady-state" to "initial" dissolution rate, and the aluminum content of each glass at each of the three solution pH values studied. Dashed lines in part (b) and (c) are provided to guide the eye for ease of comparison between data series.

5.3.3 *Topological Prediction of Activation Energy is Inconsistent with Experimental Values*

Of primary interest with regard to "initial dissolution" is the influence of *initial* composition and structure of the pristine glass on its dissolution kinetics, here defined by silicon hydrolysis from the glass network (as opposed to leaching of network-modifier ions such as sodium and calcium), which requires measurements to be conducted for short times and far from solution saturation.[154] Thus, consideration of "initial" dissolution rate allows for approximate comparison to previous such far-from-saturation studies on analogous fly ash glass.[118] Initial dissolution rates plotted as a function of the number of constraints per atom for each glass produce clear exponential trends for dissolution occurring at pH 10, with the rate of silicon release decreasing for increasing values of n_c (figure 21a). This result parallels similar findings in other studies for a variety of different glass types, which also exhibit an exponential decay in dissolution rate with increasing n_c,[23,103,106,118,149]

demonstrated in Figure 21(a) by overlaid dissolution data of fly ashes of similar composition to the synthetic glasses tested herein.

Regression analysis of dissolution vs. n_c data for aluminosilicates has in the past been used to calculate effective energies required to break a unit atomic constraint during dissolution (utilizing an Arrhenius-like equation), which for this class of materials fell in the range of 25 kJ/mol.[23,118] Such energies, when multiplied by the number of topological constraints n_c, were originally suggested to equate to an effective activation energy,[23] whereby knowledge of atomic topology for would enable description of their dissolution kinetics from a thermodynamic basis. However, recent investigation has brought to light that (1) additional consideration of the bond-strength of network forming elements is needed to generalize such a description between types of glass,[149] and (2) topological prediction of effective activation energy may prove inconsistent when compared against an effective activation energy calculated in the more typical way (i.e., from several experimental dissolution rates determined at multiple temperatures, as illustrated in Figure 21b).[150]

Of particular significance here is the finding that, for glass compositions *without* the possibility of weaker network bonds relative to those of previously studied aluminosilicates, the effective activation energies determined by topological prediction (i.e., $E_{a,effective} = n_c \cdot E_0$ using $E_0 \approx 23.9$ kJ/mol from Ref.[[118]]) *do* remain inconsistent compared with those determined experimentally. This inconsistency is illustrated in Figure 21(c) for each of the glass compositions, demonstrating that the experimental values for activation energy are unexpectedly low. This suggests that either:

(1) the measured dissolution is not rate-limited by hydrolysis of network forming elements,[155] as was assumed previously,[23] (2) the composition and structure of the glass surface has altered over the course of dissolution to reduce the local number of topological constraints per atom and facilitate dissolution, or (3) the mechanism for dissolution has changed over the course of reaction *because* of such compositional and structural alterations. The previous observation that dissolution of these glasses slowed over time in proportion to aluminum content (*Section 5.3.2*), in particular, seems to favor this latter explanation: that the near-surface region of the glass experiences time-dependent structural changes that influence dissolution mechanism,[130,131] as informed by initial composition and driven by environmental factors such as elevated hydroxyl activity (i.e., solution pH).

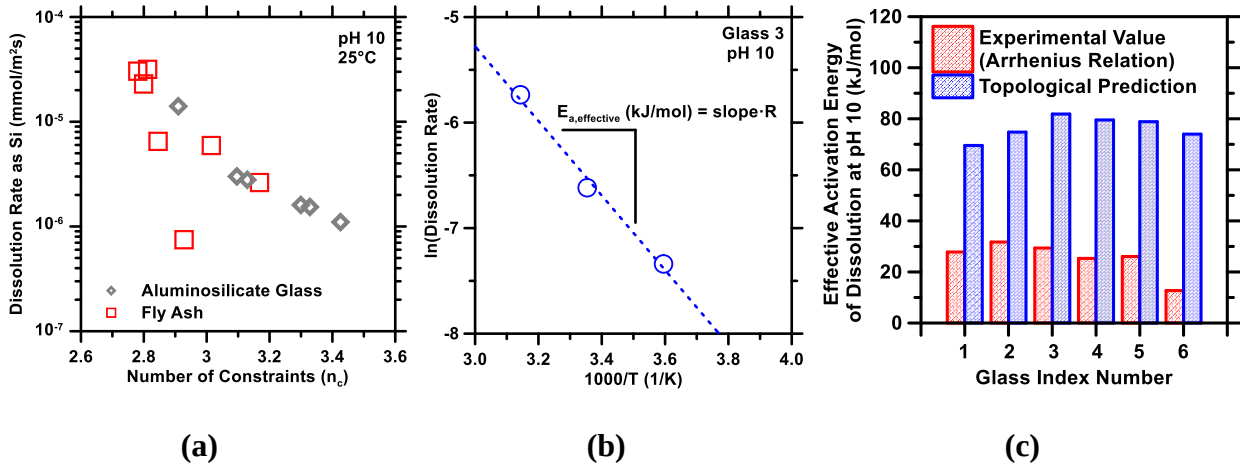

Figure 21: (a) "Initial" dissolution rate of each aluminosilicate glass at pH 10 and room temperature, overlaid on previously acquired data from fly ash,[118] demonstrating an exponential dependence on number of topological constraints. **(b)** An illustration of an Arrhenius plot used to determine effective activation of dissolution from rate values determined at 5, 25, and 45° C. **(c)** A representative set of effective activation energies for the dissolution of each aluminosilicate glass at pH 10, compared against the topological prediction. It should be noted that experimental activation energies are similarly low at higher values of solution pH, though with some mild increases due to greater aluminum release (as measured, due to a general increase in dissolution rate of all elements at higher pH), consistent

with the finding that Al inhibits silicate dissolution and increases activation energy accordingly.[150,156]

3.4 Topological Dependence of Dissolution Rate Diminishes with Increasing Solution pH

Among the environmental factors to which glass structure (n_c) may respond, elevated temperature has already shown to produce the expected increase in dissolution rate consistently across a variety of glass compositions (i.e., maintaining the dependence on initial n_c, Figure 22a), albeit to a lower degree than expected (i.e., as reflected by activation energies, Figure 21c). Elevated solution pH, however, is observed to almost completely obscure any apparent dependence of dissolution kinetics on initial n_c (Figure 22b), demonstrating a marked difference from the more simplistic dissolution behavior of fly ash at elevated pH reported elsewhere (a uniform increase in rate with pH, as has been shown herein in Figure 22a for temperature only).[118] This difference is likely due to the methods employed, wherein solution composition remained fixed (i.e., via complete renewal of solutions between dissolution steps),[118] compared with those utilized herein, wherein solution composition was allowed to evolve over time as the glass began to equilibrate with the contacting solution. As alluded to in each of the two preceding sections, both the slowing dissolution kinetics over time and the lower-than-expected activation energy (i.e., relatively less acceleration in dissolution at higher temperatures) provide indirect evidence of structural changes to the near-surface region of the glass and an associated suppression of dissolution, i.e., suggesting that the *initial* n_c no longer suffices as a descriptive structural metric as glass begins equilibrate with its environment. The obscuration of any dependence of even the "initial" dissolution rate on n_c at high pH provides a third piece of indirect evidence in support of this idea.

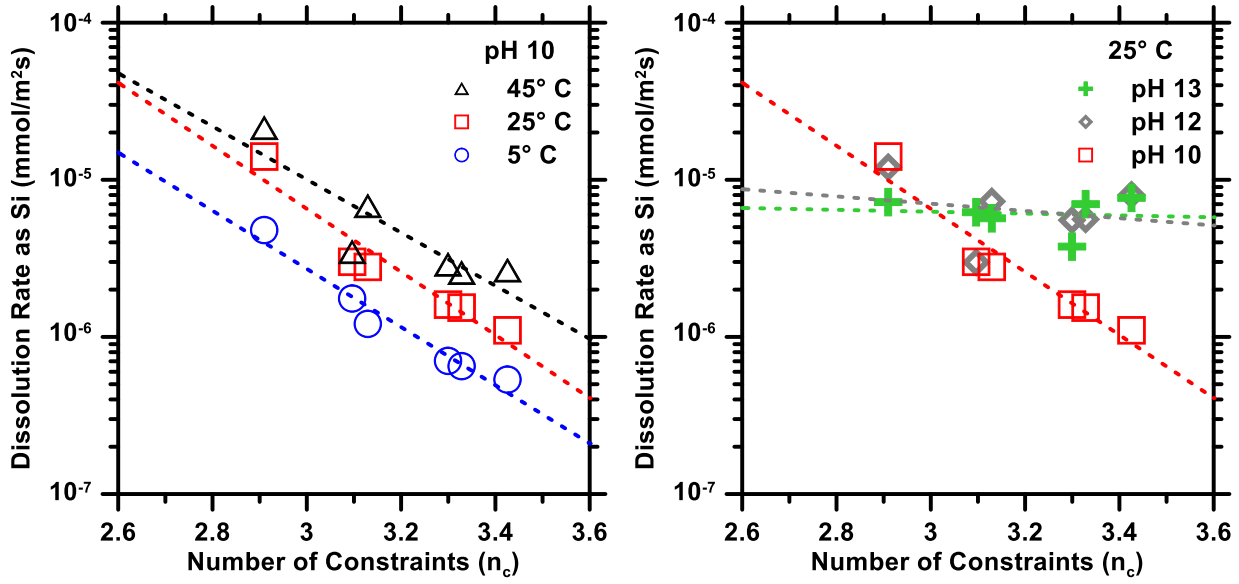

Figure 22: "Initial" dissolution rates plotted as a function of number of constraints for **(a)** dissolution occurring at pH 10 compared between 5, 25, and 45° C, and **(b)** dissolution occurring at 25° C compared between solution pH 10, 12, and 13.

5.3.5 *Incongruence of Dissolution of Aluminum Scales in Inverse Proportion to that of Calcium*

Loss of dependence of glass dissolution on its *initial* state (as quantified by number of constraints) raises the question of whether (1) dissolution of more highly-constrained glass is accelerated (i.e., an effective reduction in local n_c) or, (2) dissolution of less highly-constrained glass is suppressed. The former, local reductions to n_c, has been proposed by studies using MD simulations to demonstrate a tendency for glass surfaces to form an energetically favorable "isostatic" phase (i.e., $n_c = 3$).[157] While this phenomenon *would* evidence itself in a "flattening" of the dissolution vs. initial-n_c trend (Figure 22b), the uniformly observed decline in dissolution rates over time (Figure 20a), specifically for even the most highly-constrained glasses, would suggest the opposite: either the glasses under study generally become *more* highly-constrained over time at their surfaces, or there is a shift in dissolution mechanism from network hydrolysis to diffusive transport through

the altered layer (as supported by the low observed activation energies),[155] both of which would necessarily result in a suppression of dissolution kinetics. As such, suppression of the dissolution of less highly-constrained glass as the cause for rate alterations is given further consideration.

Previously discussed observations of silicon release rate have already provided limited verification that simpler compositional variables (i.e., aluminum content) may hold the key to gaining better understanding of the response of glass to its environment (Figure 20c). Following from this, aluminum and calcium release are considered by calculating their degree of congruence (DOC), which can act as a gauge of the retention of these elements in the glass surface during dissolution:

$$Degree\ of\ Congruence\ (M) = \frac{([M]/[Si])_{solution}}{([M]/[Si])_{solid}} \qquad (\mathbf{4})$$

Where M is calcium or aluminum release (mmol), $([M]/[Si])_{solution}$ is the ratio of this element to silicon in solution at a given time, and $([M]/[Si])_{solid}$ is the ratio of this element to silicon in the pristine glass prior to initiation of dissolution. Degree of congruence (DOC) less than 1 implies preferred retention of the element in the glass, whereas DOC > 1 implies preferred dissolution of the element from the glass (DOC = 1 implies congruent dissolution).

Degree of congruence appears to evolve over time for both calcium and aluminum, shown in Figure 23(a) and 23(b), respectively. In general, this evolution stabilizes after seven days of

dissolution (168 hours), with the values at this point presumably reflecting an approach to a dynamic equilibrium between the altered glass surface and the contacting solution: dissolution is ongoing, but this implies a stabilization in the composition of such a hypothetical altered surface though individual parts of it may be forming or dissolving. Comparison between degree of congruence (DOC) for calcium after such stabilization shows a decline in DOC by roughly an order of magnitude between pH 10 and pH 13, suggesting that elevation of pH results in more calcium being *retained* in the glass surface. Aluminum DOC shows the reverse trend, suggesting more aluminum being *released* from the glass surface at elevated pH. This apparent inverse correlation between aluminum and calcium release, shown in Figure 23(c), implies a trade-off between dissolution of network forming elements (e.g., Al, Si) and network modifying elements (e.g., Ca, Na). Such a trade-off has been noted in the literature to be characteristic of the formation of altered surface layers during glass dissolution, wherein increased rates of network bond hydrolysis were associated with increased rates of glass surface re-structuring (i.e., network bond re-condensation), resulting in "porosity closure" and a consequent reduction in the transport of network modifying elements out of the glass.[131] While this result was achieved in the past by compositional variation (e.g., adding "stronger" network forming elements such as zirconium),[131] current results demonstrate that such a phenomenon can now also be expected when varying the environmental conditions under which dissolution takes place from relatively more "aggressive" (e.g., high pH, high temperature) to relatively less "aggressive" (e.g., low pH, low temperature), corresponding to variation between preferential release of network-formers and network-modifiers, respectively (relative to the bulk glass composition).

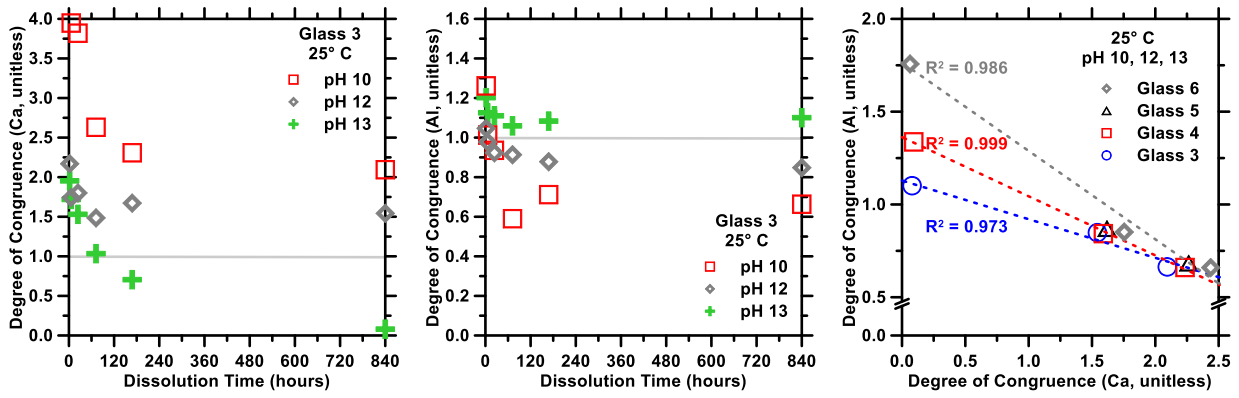

(a) **(b)** **(c)**

Figure 23: Representative time-dependent profiles illustrating evolution of degree of congruence (DOC, Equation 1) for the dissolution of glass 3 at 25° C, over a range of solution pH values, with respect to **(a)** calcium, and **(b)** aluminum. **(c)** Inverse correlations between DOC for Al and Ca at 25° C for several glass types with varied aluminum content.

5.4 Chapter summary and conclusions

The number of topological constraints is demonstrated to be descriptive of the structural detail of a range of soda-lime aluminosilicate glasses with varied Ca and Al contents similar to those present in fly ash. However, several important qualifications are outlined pertaining to the conditions under which the *initial* number of constraints may remain descriptive of glass dissolution rate as the system evolves over time. Specifically, number of constraints is shown to fail to describe dissolution kinetics under increasingly "aggressive" solution pH and temperature environments, providing several indirect indications that the glass surface, and its local composition and structure, alter over time. Tentative indication is provided that calcium and aluminum content of the bulk glass may be a starting point to develop new models that can incorporate the influence of such varied environmental conditions. Finally, it is found that the relative rates of release of aluminum and calcium (normalized by initial glass composition) scale inversely, lending support to an existing theory for a mechanism of surface re-structuring that dictates the preferential release of

either network forming or network modifying elements.[131] Outcomes enable a better understanding of which elements may be preferentially released from aluminosilicate glass of a given composition under varied environments: aluminum at high pH and/or high temperature, and calcium at low pH and/or low temperature. These understandings also provide and improved basis for the future development a *dynamic* description of aluminosilicate glass structure that can accommodate such varied environments more readily to accurately model dissolution behavior.

Chapter 6: Calcium nitrate: A chemical admixture to inhibit aggregate dissolution and mitigate expansion caused by alkali-silica reaction

6.1 Chapter scope

The formation of expansive gels over the course of alkali-silica reaction (ASR) results in cracking and mechanical property degradations of concrete.[158–160] Due to the damaging nature of ASR, and the diminishing supply of quality aggregates,[161] reliable ASR mitigation strategies are becoming increasingly important. Current approaches for reducing ASR use silica-rich Class F fly ash and lithium-based admixtures.[162–169] These additives can effectively mitigate ASR damage, but they have at least three shortcomings including: (i) seasonal variations in the supply of Class F fly ash in the U.S.,[170] (ii) heterogeneity and compositional variability of available fly ash compositions that result in different levels of ASR suppression from one fly ash to the other,[171] and (iii) the high (prohibitive) cost of lithium-based admixtures.[159] As *local* supplies of non-reactive aggregates continue to dwindle, especially in urban areas, it may become necessary to utilize *marginally reactive aggregates* in concrete construction. However, this will only be possible if an effective, economical, reliable and simple-to-implement approach is available for ASR mitigation.

The onset and progression of ASR depends on numerous material and environmental factors. Put simply, ASR occurs when reactive siliceous aggregates dissolve into the concrete's pore fluid, releasing silicon (Si) species at a rate or to an extent sufficient to precipitate hydrous alkali-silica gels.[159] The terminology "reactive aggregate" is somewhat ambiguous, so a quantitative metric is defined herein as the surface area-normalized dissolution rate of the aggregate. This choice reflects

our current understanding of ASR as a dissolution-precipitation process,[159] whereby dissolved silicon forms Si-rich hydrate gels that cause expansion and damage. Aggregate dissolution is therefore necessary for ASR, so suppressing the rate or amount of Si-dissolution would suppress the ASR process and its consequences. Based on this premise, and the noted ability of calcium to hinder silicate dissolution,[172–174] this work, for the first time, demonstrates that calcium nitrate, an inexpensive and highly soluble calcium salt,[175] inhibits both aggregate dissolution and mortar bar expansion concurrently. It is thereby able to mitigate ASR even when a highly reactive sodium borosilicate (NBS) glass is used as a model aggregate. Our observations suggest that calcium nitrate, and perhaps other alkaline earth salts can form the basis for a novel, transformative, and cost-effective means of suppressing ASR in concrete systems.

6.2 Materials and methods

6.2.1 *Materials and specimen preparation*

An ASTM C150 compliant Type I/II ordinary portland cement (OPC) was used.[176] The cement's oxide equivalent composition as measured by X-ray fluorescence (XRF) is reported in Table 5. The uncertainties reported are expressed as the standard deviation of three replicate measurements. The alkali content expressed in Na_2O equivalent was 0.37%, consistent with a low-alkali OPC.[176] The mineralogical composition of the OPC as determined by X-ray diffraction and Rietveld analysis is also reported in Table 5.

Table 5: The oxide equivalent and mineralogical compositions of the OPC used herein.

Oxide Phase	Composition (mass %)	Uncertainty (mass %)	Mineral Phase	Composition (mass %)	Uncertainty (mass %)
CaO	65.75	0.40	C_3S	57.8	1.60
SiO_2	20.54	0.40	C_2S	18.2	1.50
Al_2O_3	4.97	0.20	C_4AF	9.1	0.50
Fe_2O_3	3.10	0.10	C_3A	4.2	0.70
SO_3	2.75	0.10	$CaCO_3$	1.3	0.10
MgO	2.44	0.10	MgO	1.2	0.40
K_2O	0.29	0.01	$CaSO_4$	1.0	0.50
Na_2O	0.18	0.20	$CaSO_4 \cdot 0.5H_2O$	0.8	0.10
			$CaSO_4 \cdot 2H_2O$	0.5	0.20
			CaO	0.5	0.20

A recycled, crushed Type 33 alkali-borosilicate glass (NBS, Vitro Minerals)[177] was used as a model reactive siliceous aggregate, with a size gradation compliant with ASTM C441.[178,179] The oxide composition of the borosilicate glass as determined by SEM-EDS,[180] was (81.4 ± 2.2) % SiO_2, (12.0 ± 2.3) % B_2O_3, (4.7 ± 0.2) % Na_2O, and (1.9 ± 0.2) % Al_2O_3, by mass. The specific surface area of the smallest glass sieve fraction specified by ASTM C441, sieve #50-100 (Table 6), is 27.7 ± 1.7 m^2/kg as measured by static light scattering (SLS, LS 13320, Beckman Coulter) performed on suspensions of the glass particles in isopropanol (IPA).

The dissolution rates of silicate glasses are conventionally measured as the rate of silicon release per unit surface area. However, specific surface area measurements are quite sensitive to the method used, so reported dissolution rates can vary significantly from one study to another depending on the methods and assumptions used to characterize the surface area.[181–183] For example, light scattering is expected to underestimate the geometric surface area unless the

particles are unagglomerated spheres, and N_2 sorption is expected to overestimate geometric surface area by a factor of 2.5 because it is sensitive to molecular-scale surface defects.[183] For reference, the specific surface area of the glass particles as determined by N_2 sorption is 232.6 ± 7.8 m^2/kg (ASAP 2020 BET analyzer, Micromeritics). The ratios of N_2 sorption- and light scattering-based surface areas to the geometric surface area of NBS glass (i.e., measured using vertical scanning interferometry, VSI),[184] were calculated as 2.2 and 0.26, respectively. Nevertheless, for consistency the SLS-measured surface areas (Table 6) were used to normalize the dissolution rates in the remainder of this study.

Table 6: The specific surface area and median particle diameter (d_{50}) of the four size fractions of NBS glass particles, determined by static light scattering (SLS). The specific surface areas determined by this method have a coefficient of variation of about 5%.

Sample ID	Specific Surface Area (SSA, m^2/kg, from SLS)	d_{50} (μm)
Size 1 (Sieve #50-100)	27.7	76.4
Size 2	115	47.9
Size 3	210	15.9
Size 4	277	11.8

6.2.2 *Experimental methods*

Mortar bar expansion: The expansion of prismatic mortar bars (25 mm x 25 mm x 285 mm) was measured following a modified ASTM C441 protocol.[179] OPC and NBS glass (ASTM C441-compliant gradation) were mixed with deionized (DI) water to form mortars with water-cement mass ratio w/c = 0.50 following ASTM C305 [185]. The NBS glass particles, assumed to have a density of 2230 kg/m^3, were incorporated at volume fractions of ϕ_a = 0.15, 0.25, 0.35, 0.45, and

0.55 of the total mortar volume. In select cases, the mortar bars also contained prescribed volume fractions of ASTM C778 compliant quartz sand with a density of 2650 kg/m^3. Three different calcium nitrate dosages, in addition to a control without calcium nitrate, were used for mortars with ϕ_a = 0.25. The dosages were 1 mass %, 2 mass %, and 4 mass %, corresponding to 122 mmol/L, 244 mmol/L, and 488 mmol/L calcium nitrate, in solution. In each case the calcium nitrate was dissolved in water before mixing with the solids.

Following casting, mortar bar specimens were cured for 24 hours under 100 % relative humidity (RH) at 25 °C, 35 °C, or 45 °C. The curing temperatures were held to within ± 0.1 °C. Afterward, specimens were removed from molds and cured for an additional 24 hours under 100 % RH at the same temperatures. After 48 hours, the specimens were surface dried and the length t_0 was measured using a comparator.[186] This length will hereafter be called the initial length. The specimens were then cured under saturated conditions at the same temperatures for either 200 days or until the length exceeded that which can be measured by the comparator. The length was measured at intervals of 3 days to 14 days, from early to later ages. At least three replicate specimens were measured at each time and for each unique mortar bar formulation.

The rationale behind the above modifications of the ASTM C441 method was three-fold. First, the modifications enabled a quantitative comparison of the effects of reaction temperature on expansion. Second, it allowed the direct comparison of the effects of different aggregate volume fractions (ϕ_a) on expansion, including identification of a possible pessimum formulation.[187] Finally, the modifications make it possible to compare the influences of both temperature and ϕ_a

with and without additions of calcium nitrate ($Ca(NO_3)_2$, sometimes abbreviated as CN where convenient). One benefit of this modified method is the ability to vary aggregate volume fractions and temperature to maximize the expansion. For example, a temperature of 45°C and aggregate volume fraction of ϕ_a = 0.25 produced the maximum ASR expansion. Consequently, at different temperatures one can determine how calcium nitrate performs in so-called a "worst case" ASR scenario.

***Dissolution rate determination*:** (2.000 ± 0.005) g of NBS glass particles were added to 200 mL of a 10 mmol/L NaOH solution (pH 12) and sealed in high-density polyethylene (HDPE) bottles. While this solid-to-liquid ratio is in no way reflective of that between the aggregate and pore fluid in a realistic concrete, it provides a first point of comparison from which such an equivalence may be developed. Solutions were prepared by dissolving reagent grade NaOH in Milli-Q water (>18 MΩ·cm). The selection of the alkali cation, whether Na^+ or K^+, is expected to have little, if any, effect on the measured dissolution rates.[172,188] Salt influences on dissolution rates were tested by adding reagent grade calcium nitrate, aluminum nitrate, or lithium nitrate to the reference NaOH solution. The nitrate concentrations tested were (1, 10, 100, or 1000) mmol/L of $Ca(NO_3)_2$, (0.1, 0.5, or 1) mmol/L $Al(NO_3)_3$, and 1 mmol/L $LiNO_3$. The experiments were undertaken for each of the four different particle size ranges in Table 6.

The HDPE bottles were stored at 25°C, 35°C, or 45 °C and periodically agitated to limit particle settling, compaction, or cementation. The dissolution progress was measured by periodically withdrawing a small quantity of solution and measuring the concentrations of Si, Al, Ca, K, and

Na by inductively-coupled-plasma optical emission spectrometry (ICP-OES). Specifically, 6 mL of the solution were withdrawn after (0, 1, 3, 6, 24, 72, and 168) hours, passed through a 0.2 μm syringe filter, and diluted by a factor of 3 with 5% (by volume) nitric acid (0.79 mmol/L HNO_3) to stabilize the solution. Silicon and aluminum (axial view), as well as calcium, potassium, and sodium (radial view) were measured, with corresponding uncertainties (i.e., as determined by measurements carried out on a known reference solution) of: ± 0.85 % for Si, ± 0.81 % for Al, ± 3.08 % for Ca, ± 1.35 % for K, and ± 6.15 % for Na. The composition data revealed a nearly linear increase in Si concentration with time for the first six hours. The slope of that line determined by linear regression, divided by the initial particle surface area, was used to characterize the *initial* dissolution rate in units of mmol/(m^2·s).

***Surface analysis of NBS glass particles*:** Following 7 days of dissolution, the glass surfaces were characterized for their morphology, bulk composition, and possible coverage by precipitates using thermogravimetric analysis (TGA, STA 6000, Perkin Elmer), attenuated total reflectance Fourier transform infrared spectroscopy (ATR-FTIR, Spectrum Two, Perkin Elmer), and scanning electron microscopy paired with energy dispersive spectroscopy (SEM-EDS, Phenom G2).

- TGA was conducted by heating partially dissolved glass particles at a rate of 10 °C/min in pure aluminum oxide crucibles from 35 °C to 975 °C under ultra-high purity (99.999%) N_2 purge gas at a flow rate of 20 mL/min, as the mass loss (due to thermal decomposition) was measured. The types and mass fractions of compounds present were identified from the mass loss occurring within characteristic decomposition temperature ranges, such as (35 to 125) °C for evaporable water and (550 to 700) °C for calcium carbonate.

- ATR-FTIR was conducted by placing partially dissolved glass particles on a diamond/ZnSe composite crystal and compressing the assembly at approximately 70 N with a pressure applicator at an incidence angle of 90°. Each spectrum acquired was the average of four scans in the wavenumber range of 4000-450 cm^{-1} with a spectral resolution of 1 cm^{-1}. Peak assignments for potential surface precipitates were made using similarly acquired patterns for reference compositions of calcite and synthetic calcium-silicate-hydrate (C-S-H) with a Ca/Si atomic ratio of 1.8.[189,190] The actual Ca/Si ratio of C-S-H formed on glass particles may vary (e.g., determined by SEM-EDS to range between 1.4-to-1.8). However, C-S-H with Ca/Si = 1.8 was used for peak assignments because its absorption peaks are more distinct relative to the background absorption of the NBS glass, particularly at high wavenumbers (> 1200 cm^{-1}), and the absorption peaks appear in similar locations for different Ca/Si compositions.
- SEM-EDS was conducted by mounting partially dissolved glass particles on copper tape and sputter-coating them with a few nanometers of gold prior to backscatter imaging (10 kV) and energy dispersive x-ray spectroscopy for elemental analysis (15 kV). This imaging was used to assess the morphology and composition of the glass surfaces and to detect any obvious surface precipitates. Sections extracted from the mortar samples were also prepared for SEM analysis, i.e., after 14 days of aging. These mortar fragments were subjected to solvent exchange in isopropanol to arrest hydration, after which they were stabilized in an epoxy resin and polished. These surfaces were also sputter-coated with gold and analyzed in a manner identical to that described for the particles above to assess compositional profiles in the near-surface region for the NBS glass particles.

***Interrogation of other changes to the cementitious environment*:** To assess the influence of calcium nitrate additions on other aspects of the cementitious environment, measurements were made of the zeta potential of the glass particles, a proxy for surface charge (Zeta-PALS, Brookhaven Instruments Corporation). Suspensions of 0.01 % by mass of NBS glass particles of size class 2 (Table 6) in a 10 mmol/L NaOH solution were prepared with and without calcium nitrate additions. The measurements were initiated in ≤ 10 minutes after adding the glass particles. A sequence of 10 replicate measurements was acquired, with each measurement requiring about one minute to perform, from which the mean and standard deviation were calculated; no appreciable drift was observed across the measurements.

In addition to zeta potential measurements, the time-dependent evolution of cement paste pore solution compositions was measured. Cylindrical cement paste specimens were prepared for pore solution extractions at w/c = 0.45 according to ASTM C305, with 1 %, 2 %, or 4 % $Ca(NO_3)_2$ (by mass of cement) added to the mixing water. The specimens were stored at 25 °C and pore solutions were extracted at (1, 3, 7, and 28) days. Sodium, potassium, calcium, and aluminum concentrations in these solutions were measured by ICP-OES using the same extraction and dilution procedures as described previously.

6.3 Results and discussion

6.3.1 *Mortar expansion kinetics are influenced by aggregate reactivity and volume fraction*

The ASR-induced expansion strain of mortar bars, as shown in Figure 24(a), exhibits two distinct regimes: (1) an approximately linear increase, which gradually reaches (2) a plateau with little or no expansion, most evident at higher NBS volume fractions such as ϕ_a = 0.55. A comparison of the expansion kinetics for different ϕ_a is given in Figure 24(b) by normalizing the expansion strain by NBS volume fraction. This normalization causes the linear regimes in Figure 24(a) to collapse onto a single line at times up to 20 days. Additionally, this normalization more clearly shows that the transition to a plateau happens at earlier times with increasing aggregate volume fraction. Further quantitative analysis of the expansion behavior can be undertaken by examining four parameters: (1) initial expansion rate, $R_{e,i}$, which is the initial slope of the curves in Figure 24(a) over the first 20 days; (2) mature expansion rate, $R_{e,m}$, taken to be the slope of the curves in Figure 24(a) between 100 days and 200 days; (3) time of plateau onset, t_p, i.e., the time at which the linear fits used to determine initial and mature expansion rate intersect; and (4) 200 day expansion, ε_{200}, i.e., the expansion measured after 200 days; an arbitrary but sufficiently mature point in time.

Figure 25(a) shows the expansion at 200 days as a function of ϕ_a. The plot suggests a pessimum aggregate fraction (i.e., that for which the most expansion occurs), ϕ^*_a, of about 0.35 at 25 °C and 35 °C, or about 0.25 at 45 °C. That is, the strain at 200 days increases with ϕ_a for $\phi_a < \phi^*_a$ but decreases at higher aggregate fractions. The behavior below the pessimum is consistent with the idea that ASR-induced expansion is proportional to the reactive aggregate surface area. However, the reverse trend for $\phi_a > \phi^*_a$ indicates that some factor or factors besides reactive surface area

affect the expansion at higher volume fractions. Two other trends are associated with ϕ_a. First, the time of plateau onset (t_p) uniformly decreases with increasing ϕ_a (not shown), and second, above the pessimum the mature expansion rate ($R_{e,m}$) was effectively zero. Neither of these latter two observations on the effect of aggregate fraction can be explained in terms of the aggregate surface area alone.

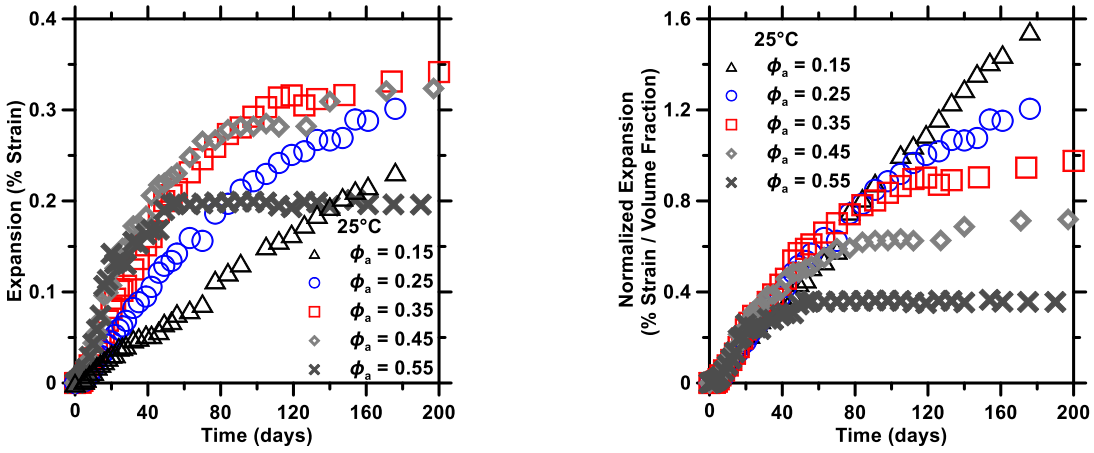

(a) **(b)**

Figure 24: The **(a)** measured expansion, and **(b)** volume-fraction-normalized expansion of NBS glass-containing mortar bars at 25°C, for volume fractions, ϕ_a, ranging from 0.15 to 0.55.

To better understand why the expansion strain decreased with increasing ϕ_a above the pessimum, the NBS glass was replaced, in part, by inert quartz sand while leaving the total volume fraction of aggregate unchanged. For example, the data shown as solid points in Figure 25 were obtained with ϕ_a = 0.55 = 0.15 NBS glass + 0.40 quartz sand. Replacing glass with quartz sand is expected to effectively reduce reactive surface area while leaving mortar stiffness broadly unchanged (N.B.: The NBS-glass and quartz sand feature stiffnesses that are similar to each other, i.e., around 82 GPa for NBS-glass and 86 GPa for quartz, respectively).[191,192] The early-age expansion of these

quartz-substituted mortars (Figure 25b, filled symbols) was similar to that of the ϕ_a = 0.15 NBS-glass containing samples, though their expansion slowed more rapidly over time, reaching a plateau similar to that of the ϕ_a = 0.55 NBS-glass mortars (Figure 25a, filled symbols). This suggests that while parameters such as the initial expansion rate ($R_{e,i}$) may better reflect the chemical effects of the aggregate (e.g., reactive surface area), the plateau-ing behavior, and the other parameters (ε_{200}, t_p, $R_{e,m}$), are affected also by the mechanical stiffness of the mortar bars. This is indicated by the reduction in expansion with increasing aggregate dosage beyond the pessimum, i.e., as the composite becomes stiffer, and appears to be insensitive to whether the aggregate is reactive (NBS) or not (quartz). Therefore, and to avoid the complexities of the pessimum effect and its variation with reaction temperature, here forward consideration will only be given to systems that feature an aggregate dosage at or below the pessimum (i.e., $\phi_a \leq 0.25$). This also justifies the reasons for using a modified ASTM C441 protocol, since the test method as formulated is implemented at 38°C and incorporates NBS glass at $\phi_a \approx 0.55$, i.e., in excess of the pessimum aggregate dosage.

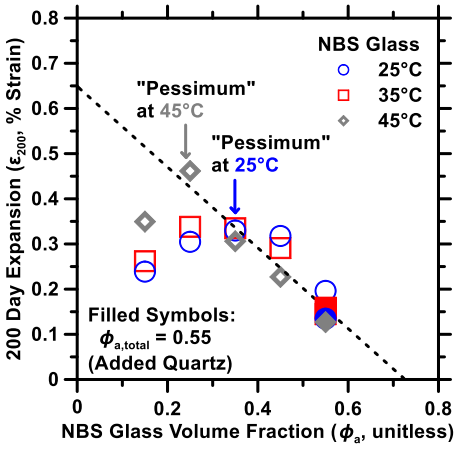

(a)

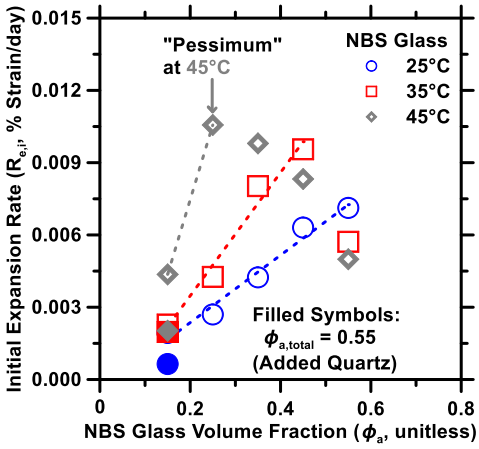

(b)

Figure 25: (a) The 200 d expansion data, ε_{200}, plotted as a function of NBS glass volume fraction. A linear fit to strain for $\phi_a > \phi^*_a$ is also shown. **(b)** The initial expansion rate of NBS glass mortar bars, $R_{e,i}$, plotted as a function of the NBS glass volume fraction. The linear regressions suggest proportionality between ϕ_a and expansion rate. The data for quartz-substituted systems ($\phi_{a,total}$ = 0.55 consisting of 0.15 NBS glass and 0.40 quartz sand) are shown as solid symbols for comparison (on both plots).

Figure 26(a) compares how the initial expansion rates depend on temperature, ϕ_a, and calcium nitrate (CN) admixture dosage. The reference condition for this comparison is established at 45°C, ϕ_a = 0.25, and 0 % CN, which produces the highest rate and extent of expansion. As expected from Figures 24 and 25, decreasing either the temperature or the aggregate volume fraction (and surface area), or increasing the calcium nitrate dose all reduce the rate and extent of expansion. The effect of adding a modest amount of calcium nitrate (2 mass %) suppresses the expansion rate as much as a 10 °C temperature reduction or a 10 % decrease in ϕ_a. Further increasing the dosage of CN produces even greater suppression of the expansion rate, even more than a 20 °C temperature reduction achieves. Figure 26(b) suggests that systems differing only in their CN dosage might converge to approximately equal expansion strain at late ages. That is, adding CN might only delay the ASR expansion and damage, by suppressing the initial expansion rates, rather than suppressing them entirely. The efficacy of calcium nitrate in suppressing early-age ASR expansion rates may be thought to be on account of its acceleration of early-age hydration and strength gain. However, this possibility can be rejected as CN's effect on properties such as mortar stiffness and strength is effectively negligible for the dosages considered.[193] Even so, expansion data alone cannot reveal whether calcium nitrate acts by slowing the reaction rate (or the extent of ASR) per unit area or by somehow reducing the total reactive surface area of the aggregates.

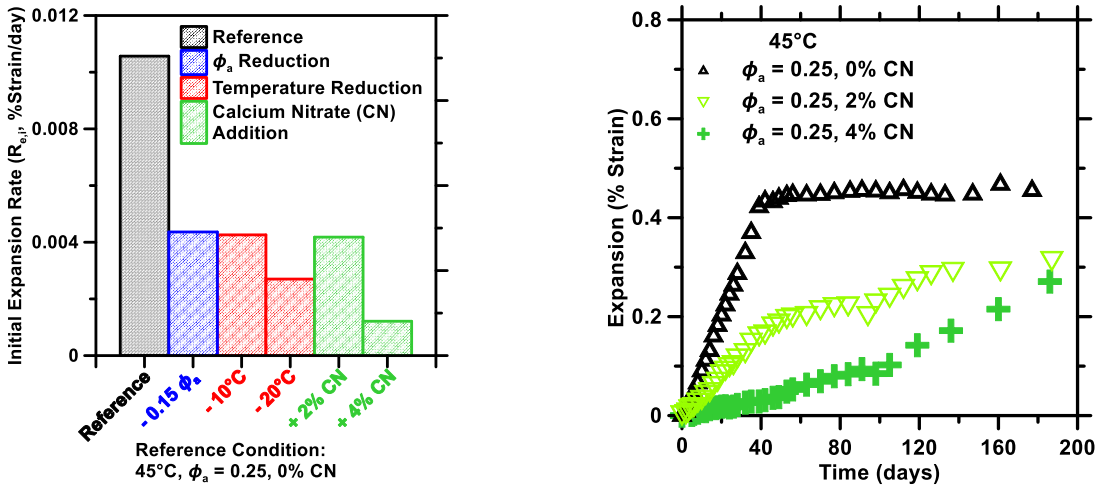

Figure 26: (a) A comparison between the initial expansion rates of cementitious mortar bars over the first 20 days for conditions encompassing: different NBS glass volume fractions (ϕ_a), reaction temperature, and calcium nitrate (CN) dosage. **(b)** A comparison between expansion profiles for the reference mortar bars and its $Ca(NO_3)_2$ containing counterparts, showing the progressive inhibition of expansion with increasing additive dosage.

6.3.2 *Kinetics of dissolution of NBS glass in alkaline solutions*

Since ASR is provoked by the presence of reactive aggregates,[159] to offer a quantitative basis of discussion it is meaningful to assess the surface area-normalized reactivity of aggregates. This allows one to understand how the dosage of calcium nitrate ($Ca(NO_3)_2$, CN) affects dissolution rates, and in turn suppresses ASR-induced expansion.

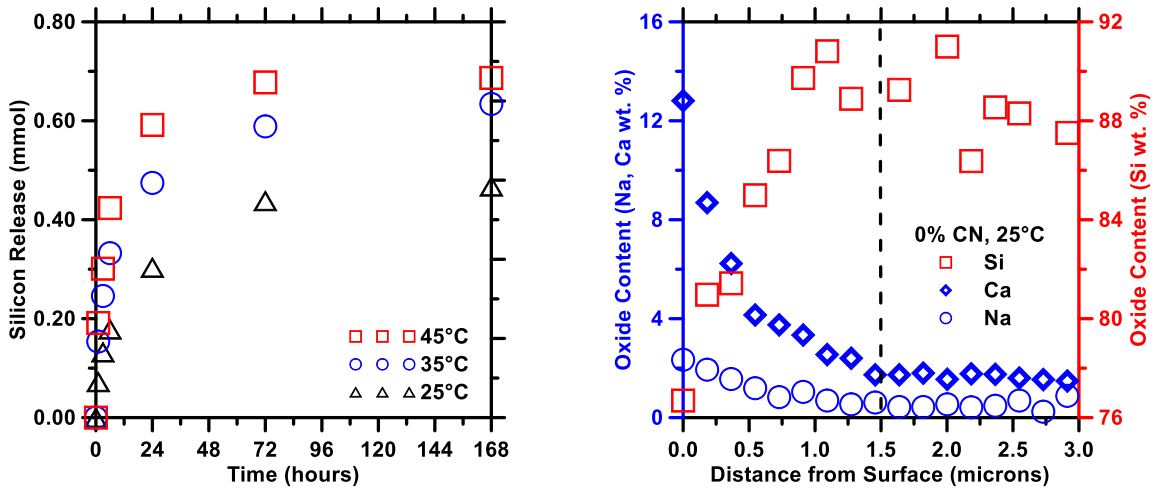

(a) **(b)**

Figure 27: (a) Representative silicon release as a function of time and temperature, for the dissolution of NBS glass (Size 3, d_{50} = 15.9 μm) in a pH 12 (10 mmol/L NaOH) solution. **(b)** A compositional line profile acquired using SEM-EDS transverse to the surface of a representative borosilicate glass particle embedded in 14 d mortar bar. It should be noted that the interaction volume associated with the SEM-EDS measurement is on the order of one cubic micron, limiting the use of this technique as applied to altered surface layers.

Figure 27(a) shows representative silicon release profiles as a function of time at each temperature of interest in the absence of CN (pH 12 NaOH). At early times < 6 hours, the concentration of solubilized silicon increased near-linearly, as typical for far-from-equilibrium dissolution.[194–196] After around 24 hours of dissolution, the silicon concentration in solution plateaued, as did the release of other elements (not shown). The plateau in dissolution for the reference system was not associated with the formation of precipitates nor saturation with respect to silicon (see *Section 6.3.4*). Aside from these two expected phenomena, an alternate explanation for the plateau may be that NBS dissolution is *transport controlled* under these conditions.[197] Such transport control as caused by *in-solution* transport limitation [197] likely does play some role for NBS glass, as evidenced by an enhancement in dissolution rate under stirred conditions, though *surface alteration* of the NBS glass particles (i.e., acting as a diffusion barrier), another well-known

phenomenon for glasses, may also contribute to slowed dissolution.[86,87,153,198,199] Despite the high pH, which is expected to limit the formation of glass alteration layers,[153] SEM-EDS compositional profiles at NBS-glass particle surfaces suggest the presence of Na- and Ca-enriched, and consequently silicon-depleted regions (i.e., relative to the bulk NBS glass, Figure 27b). While this provides some indication that the mechanisms controlling dissolution may evolve over time, detailed specifics are lacking (e.g., SEM-EDS has an interaction volume on the order of one cubic micron, insufficient for the small-scale characterization necessary for study of alteration layers), and so further work – a broad question of interest to the glass community – is needed to examine how time-dependent surface alterations may affect silicate glass's dissolution kinetics.

6.3.3 *Dissolution is slowed by calcium and aluminum species even at low concentrations*

Initial dissolution rates were determined for a range of CN concentrations as shown in Figure 28(a). For simplicity, the initial dissolution rate, r_d, was measured by first using linear regression to determine the slope (mmol/h) in the range $0 < t < 6$ h when the concentration increases approximately linearly with time (Figure 27a). The slope was then divided by the initial total glass surface area (specific surface area multiplied by original mass), and the units transformed to obtain the rate in units of mmol/(m^2·s). Lithium and aluminum nitrates were also considered because of the prevalent use of lithium for ASR mitigation, and because of the known ability of aluminum to inhibit the dissolution of crystalline quartz.[156] In general, both calcium and aluminum reduced the initial dissolution rate, but lithium nitrate exerted little or no effect. This emphasizes that the role of lithium nitrate in ASR suppression is *not* to inhibit dissolution,[169] and therefore highlights that dissolution rate measurements alone may not be able to identify effective ASR inhibitors.

Significant reductions in dissolution rates are observed when either calcium (nitrate) or aluminum (nitrate) are present even at concentrations as low as 1 mmol/L (Figure 28a).[200] Such low concentrations are present inherently in most concrete port solutions at later ages. This suggests that in cementitious environments, silicate glass dissolution may be inherently slower than in pristine NaOH solutions, simply on account of the background abundance of Ca and Al species resulting from OPC hydration. Figure 28(a) also shows that at concentrations on the order of 1 mmol/L, Al species inhibit the glass dissolution more than Ca species at the same concentration. However, Al concentrations were restricted herein to match the quantity of aluminum that could be realistically mobilized, e.g., corresponding to the solubility limit of gibbsite,[201] or that are expected in mature cement paste pore solutions.[202] Practically speaking, this is important because excess aluminum can detrimentally affect setting behavior and the long-term durability of cement-based materials – likely ruling out the use of aluminum additives for ASR mitigation in concrete.[203] Calcium nitrate produces a progressive reduction in dissolution rate with increasing dosage (Figure 28a). However, the CN effect has limitations, too; the dissolution rate stops decreasing at CN concentrations above 100 mmol/L. For practical concrete applications such as set acceleration, CN is added to the mixing water at concentrations between 100 mmol/L and 500 mmol/L, so current usage of CN in industry, e.g., for set acceleration applications, is expected to be sufficient to achieve the most dissolution suppression that CN can likely provide.

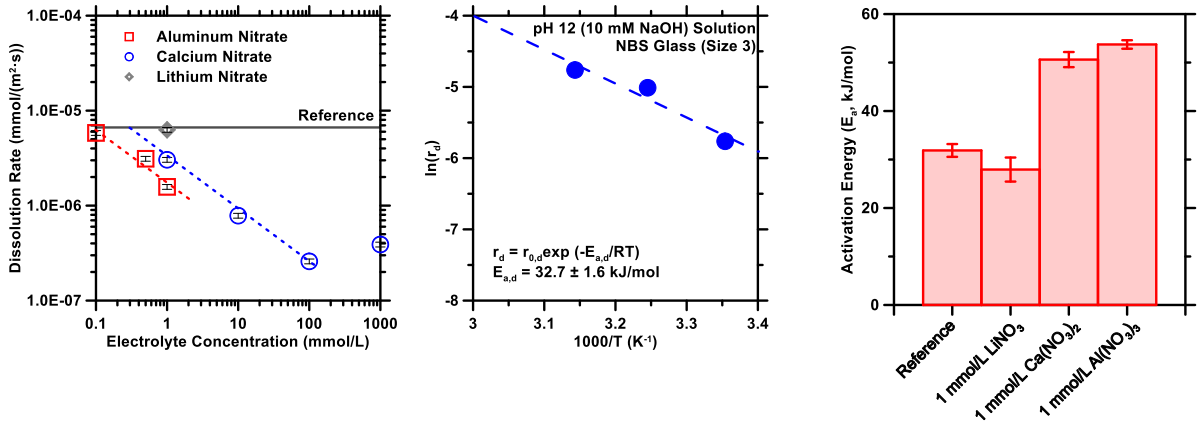

(a) **(b)** **(c)**

Figure 28: (a) The dissolution rates of NBS glass (Size 3, d_{50} = 15.9 µm) in a pH 12 (10 mmol/L NaOH) solution dosed with Al, Ca, and Li nitrate salts, as a function of salt concentration. **(b)** A representative Arrhenius plot that is used to estimate the activation energy of NBS glass dissolution. **(c)** The activation energy (E_a, kJ/mol) of NBS glass dissolution in selected solution compositions from 25 °C ≤ T ≤ 45 °C.

6.3.4 *Dissolution suppression by calcium goes beyond surface area reductions*

The initial dissolution rates of the NBS glass are dependent on temperature (Figure 27a). To describe the temperature dependence of dissolution, the rate data were plotted against inverse temperature in Figure 28(b), and the slope obtained by linear regression was used to infer an effective activation energy of dissolution, described as: $r_d = r_{0,d} \exp\left(-E_{a,d}/RT\right)$, where, $r_{0,d}$ is a pre-exponential factor (mmol/(m^2·s)), $E_{a,d}$ is the apparent activation energy of dissolution (J/mol), R is the gas constant (8.314 J/(mol·K)), and T is the thermodynamic temperature (K).[204] The calculations produce an *apparent* or *effective* activation energy of a reaction process comprising multiple dissolution steps such as network hydrolysis, surface diffusion, and bulk mass transport of dissolved species, without any distinctions made for elementary reactions.[194,204,205] This effective activation energy, which is expectedly similar for all size fractions of glass tested (Table 6), is $E_{a,d}$ = 32 ± 1.6 kJ/mol (Figure 28c). Although the dissolution rate of NBS glass should

increase with pH in the basic regime, the effective activation energy should be pH-independent because nucleophilic attack of the silanol groups by OH^- ions remains the dominant mechanism of dissolution.[172,194,204] Therefore, although the solution pH in which dissolution was evaluated, pH 12, is slightly lower than that of typical cementitious pore solutions,[188,206] the activation energy is expected to be similar even as the pH increases. The reference effective activation energy is, however, expected to be lower than that applicable to NBS glass dissolution in realistic cementitious environments, in which low concentrations of calcium and aluminum present in the pore solution would reduce silicate dissolution rates, as previously discussed.[156,172–174,207–209] Careful analysis of the dissolution rate data indicates that the activation energy increases substantially in the presence of dissolved Ca or Al. This implicates a fundamental change in the rate limiting step of dissolution, and not simply an effect related to a reduction in reactive surface area, as an example. It may suggest that dissolution suppression by increases in activation energy, produced by low concentrations of either Ca or Al species, may be due to any of several effects, such as (1) their influence on near-surface transport of dissolved species;[197] (2) ion adsorption on reactive surface sites;[156] or (3) the formation of altered surface layers.[173,210]

6.3.5 *Surface barriers containing Ca form rapidly but require higher Ca concentrations*

Geochemical analysis of the solution composition data over the course of dissolution, i.e., using PHREEQC[211,212] and GEMS,[213–215] reveals that when CN is added at concentrations in excess of 10 mmol/L the solution rapidly ($\leq$ 1 h) becomes supersaturated with respect to calcite and calcium silicate hydrate (C-S-H) for pH > 12, with the latter expected to precipitate in larger amounts. In light of this, the influence on glass dissolution of calcium nitrate and similar alkaline earth salts is

likely associated with two factors. The first, already touched upon earlier, is the interactions of calcium ions with the glass surface,[86,87,173,198,199,216] which increases the effective activation energy of the dissolution process. An increase in effective activation energy could reflect an increase in the rigidity of the glass's atomic network, surficially, as proposed by Pignatelli *et al.*[121] and Oey *et al.*[118] However, the supersaturation of the CN solution with respect to calcite and C-S-H suggests that a second and concurrent effect is the formation of calcium-bearing precipitates on reacting particle surfaces,[172–174] which can form, e.g., a diffusion barrier and partially passivate the surface by reducing its exposed reactive area. Realistic cementitious systems have solutions that evolve in composition over time, especially at early times before the solution approaches equilibrium with respect to the precipitated solids. In those systems, additives such as calcium nitrate can increase the calcium concentration at early ages, but at later ages the calcium concentration will still be effectively constrained by chemical equilibrium considerations, as suggested by the later-age data shown in Figure 29(a). Therefore, the dissolution suppression produced by calcium nitrate is caused primarily by the early formation of stable, calcium-containing precipitates on the glass surfaces which persist on reactive aggregate surfaces over time.

Zeta potential measurements were made to investigate the possibility that calcium-containing barriers rapidly form on and passivate NBS glass surfaces. Zeta potential, the electric potential at the shear boundary that separates the more tightly bound near-surface portion of the electrical double layer from the bulk solution, is used here as a proxy for particle surface charge. Figure 29(b) indicates significant changes in zeta potential depending on the type and concentration of nitrate additive. Among the possible reasons for a change in zeta potential are (1) an alteration in the atomic arhictecture of the solid surface, (2) precipitation of another phase on the solid surface,

and/or (3) changes in the type or concentration of charged ions in the double layer, which may also be associated with a compression of the double layer itself. Therefore, the interpretation of zeta potential changes can be challenging and should be supplemented with complementary measurements using microscopy or other surface characterization methods, as will be discussed shortly. At this point, some insight still can be gained by analyzing the zeta potential reversals observed in Figure 29(b). The alkaline solutions used in this study were in direct contact with air containing CO_2 at a concentration of around 410 ppm. So, the solutions containing dissolved calcium are expected to be supersaturated with respect to calcite. Figure 29(b) shows that the zeta potential of the NBS particles in solutions with [Ca] ≥ 10 mmol/L is approximately equal to that of calcite particles of about the same size in similar solutions. This observation provides indirect evidence that calcium carbonate might precipitate on the NBS surfaces in these solutions and may be responsible for the zeta potential changes relative to the reference system. All the zeta potential measurements were made within the first 10 minutes after introducing the particles to the solution, so surface precipitates must form relatively quickly if this hypothesis is correct, consistent with geochemical analyses.

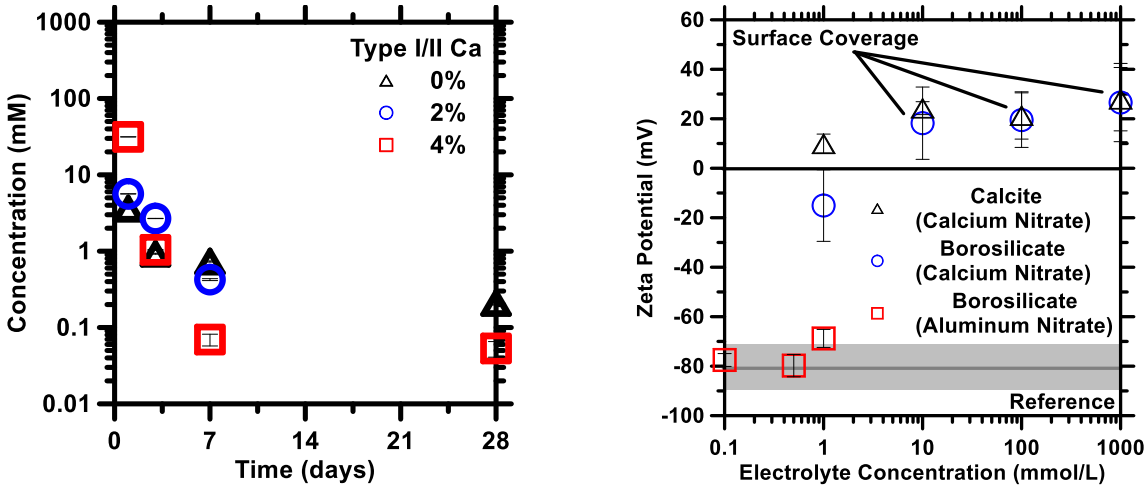

(a) **(b)**

Figure 29: (a) The concentration of Ca-species in extracted cementitious pore solution as a function of time for both $Ca(NO_3)_2$-dosed and calcium nitrate free systems, and **(b)** The zeta potential of calcite and NBS-glass particles in contact with pH 12 (10 mmol/L NaOH) solutions containing different concentrations of calcium (and aluminum) nitrate. The shaded gray region shows the zeta potential that is measured under *additive-free* conditions (the width of the gray region shows the standard deviation of replicate measurements).

Consistent with the indication from solution analyses and zeta potential that CN additions induce rapid precipitation on NBS-glass surfaces, SEM-EDS analysis confirmed the substantial formation of surface precipitates (i.e., in addition to any presence of Ca-species in the glass surface), which increased progressively with additive concentration (e.g., from 1 mmol/L to 100 mmol/L, Figure 30). These precipitates evidenced compositions with C/Ca ≈ 1 (atom ratio), i.e., as applicable for the case of calcite. The dramatic increase in the coverage of surface precipitates at about 100 mmol/L Ca concentration is consistent with thermogravimetric analysis (TGA). Herein, the calcite content present on the glass surfaces was observed to increase by a factor of 10 (i.e., from ≈ 1 mass % to 10 mass %) as the CN dosage increased from 1 mmol/L and 100 mmol/L. At a dosage of 100 mmol/L CN, calcium-silicate-hydrates were also noted to form (C-S-H, e.g., based on TGA-based water loss trends) which indicated, roughly, a calcite-to-C-S-H ratio on the order of 4:1 of the

precipitates (mass basis). Further analysis using FTIR confirmed the presence of both C-S-H and calcite, based on the matching of known peak positions of these compounds.[189,190] It should be noted, however, that in the thermodynamic limit, C-S-H is unstable in the presence of atmospheric CO_2, and thus in time it will convert to a mixture of calcite and hydrous silica. Nevertheless, in separate experiments of NBS-glass dissolution carried out under CO_2-free conditions, both in the presence and absence of CN, NBS-glass dissolution rates of a similar magnitude to those observed under conditions of atmospheric CO_2 exposure manifest. This may suggest that, in fact, C-S-H forms first on NBS-glass surfaces, and then in an open-system converts systematically to calcite so long as atmospheric CO_2 is present.

6.3.6 *Activation energy comparisons suggest that dissolution controls ASR*

The experiments performed here cannot distinguish the many individual elementary reactions that participate in ASR. However, it should still be possible to determine whether the overall process of glass dissolution exerts a greater or lesser influence on macroscopic ASR rates than the overall ASR gel growth process or the expansion process. The effective activation energy of the dissolution process has already been discussed (Figure 28c). The temperature dependence of the expansion rates of mortar bars with NBS aggregate (*Section 6.3.1*) was also analyzed to obtain an effective activation energy of expansion of about 50 kJ/mol. This value is close to the activation energy of dissolution of NBS when calcium nitrate or aluminum nitrate is added (Figure 28c). The mortar bar pore solution has calcium and aluminum concentrations comparable to those produced in the dissolution experiments. The equality of the two activation energies therefore is either a

surprising coincidence or, more likely, is indirect evidence that the rate of the dissolution process exerts a greater influence on ASR than the rate of gel growth.

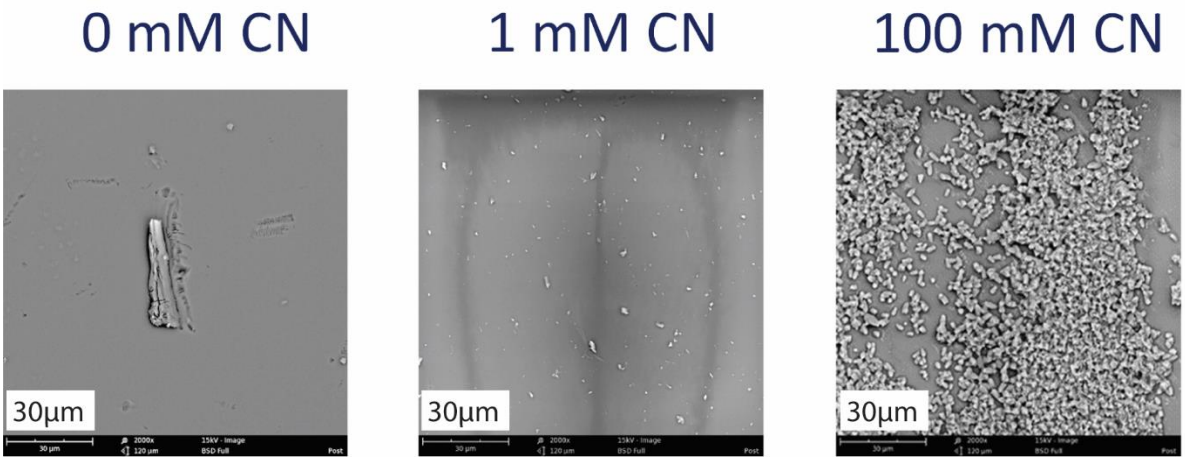

Figure 30: Representative SEM images of NBS glass particles exposed to pH 12 NaOH solutions for 7 days across varying concentrations of calcium nitrate (CN). The surface coverage of precipitates forming on the NBS-glass surfaces increases dramatically with CN concentration thus implicating the role of surficial barrier formation in dissolution inhibition. The image for 100 mmol/L CN has been republished with permission from.[172]

Both the activation energy of the dissolution process and of mortar bar expansion are now compared to that calculated based on a recently proposed topological approach.[217] The dissolution rate in a given solution composition may be written as $r_d = r_{0,d} \exp(-n_c E_0/RT)$, where n_c represents the average number of topological constraints per atom (unitless) and E_0 represents the average rupture energy of a unit constraint.[217,218] For the NBS glass, n_c = 3.43 has been calculated using topological constraint theory,[217,218] and E_0 is between 8 kJ/mol and 25 kJ/mol for aluminoborate and aluminosilicate glasses, respectively.[149,217,218] Alkali and alkaline-earth network modifiers slightly reduce n_c and the effective activation energy of dissolution, $n_c E_0$, based on prior analysis of fly ash glasses,[218] but this influence of network modifiers is relatively small,

only a few kJ/mol. On the other hand, the boron atoms in a glass are known to reduce the activation energy of hydrolysis substantially because the hydrolysis barriers for B–O–B and B–O–Si hydrolysis are lower than for Si–O–Si hydrolysis.[219] The effective activation energy of dissolution in the absence of $Ca(NO_3)_2$ (Figure 28c), together with the number of constraints per atom, suggest that $E_0 \approx 10$ kJ/mol. This value is consistent with that assessed for aluminoborate glasses and suggests that the rate of dissolution of the NBS glass is probably most influenced by its weak B–O–B and B–O–Si bonds rather than the strong Si–O–Si ones. The glass used in this study might also be phase-separated, comprising both a chemically durable Si-rich phase and a more reactive B-rich phase.[220] This is consistent with the fact that over-constrained glasses ($n_c > 3$, as in the present case) tend to exhibit phase separation or crystallization.[221]

The observation that the effective activation energy does not significantly change in the presence of Li suggests, as postulated previously, that Li species do not affect glass dissolution. In contrast, either $Ca(NO_3)_2$ or $Al(NO_3)_3$ additions greatly increase the activation energy to ≈50 kJ/mol (Figure 28c). This indicates that changing the solution composition induces a significant change in the dissolution process, perhaps a change in its rate-controlling step. This also implies that a simple geometrical surface area reduction alone is not solely responsible for the observed inhibition of dissolution because a surface area change should affect only the rate and not the activation energy. Instead, the additives likely cause a modification of the local environment at reactive surface sites, e.g., by ion adsorption and/or formation of an altered surface layer that increases the energy required to sever bonds at the surface or to diffuse through a barrier layer, respectively. This nature of inhibition acts in parallel with reductions in surface area by precipitation (Figure 30) to produce the severe dissolution inhibition shown in Figure 28(a). This paints a broader picture of a

concentration-dependent response, wherein while low dosages of Ca-species induce changes to the reactivity of the glass's surface, the formation of precipitates at higher dosages causes incremental reductions in geometrical surface area. Thus, after inducing an initial change in the rate-limiting step, and the activation energy of glass dissolution, no further change in the activation energy of dissolution is produced thereafter, i.e., with increasing Ca-concentration, although the rate and extent of glass dissolution continues to reduce progressively.

This analysis of the equivalence of activation energies of NBS dissolution and of mortar bars made using NBS aggregate offers support for the hypothesis that aggregate dissolution rates control ASR expansion in these systems containing elevated dissolved calcium. It also supports the idea that CN is able to mitigate ASR primarily because the excess dissolved calcium promotes early-age surface precipitation of C-S-H or calcite on NBS glass surfaces thereby reducing their dissolution rate (Figure 29a). These beneficial effects are not observed in typical OPC-based systems because the initial Ca-concentrations in those systems are not high enough to induce the formation of the surface precipitates (Figure 30); which are pre-requisite to suppress the silicate dissolution rate sufficiently to mitigate alkali-silica reaction.

6.4 Chapter summary and conclusions

Using a highly reactive sodium borosilicate (NBS) glass as a model ASR-reactive aggregate, this study has shown, for the first time, that calcium nitrate additions effectively inhibit aggregate dissolution and, in turn, mortar bar expansion. These processes are shown to be closely related, as highlighted by their nearly identical effective activation energies. This suggests that the aggregate

dissolution process dictates the progress of ASR. Furthermore, this work suggests that any chemical additive capable of inhibiting reactive silicate dissolution, i.e., regardless of its operating mechanism, can serve as a viable ASR mitigation method. For example, while a Class F fly ash may react to provide enough calcium or aluminum in solution to interact with reactive sites on the aggregate surfaces, higher dosages of soluble alkaline-earth salts could promote the precipitation of C-S-H or calcite to partially cover and passivate the dissolving aggregate surface. Thus, candidate ASR inhibitors could be quantitatively evaluated by measuring their influence on aggregate dissolution rates over time, although this would require the development of a cost-effective standard test method for measuring dissolution rate changes.

This work also helps understand how surface alterations affect chemical reaction rates. This is important to distinguish how intrinsic reactivity reductions versus physical coverage are important in affecting ASR reaction rates. Surface reactivity changes are indeed important, as suggested in this study, but physical surface coverage is perhaps even more important for reducing the rate and extent of aggregate dissolution during ASR. This latter aspect especially dictates why ASR mitigation can be achieved by the use of soluble alkaline-earth salts.

Implications: This work provides new insights into how soluble alkaline-earth salts, such as $Ca(NO_3)_2$ (and by extension others such as $Ca(NO_2)_2$, and their Mg-variants, among others) can mitigate ASR in concrete. However, substantial work is needed to fulfill the remaining knowledge gaps prior to commercialization. For example, practical construction operations employ a variety of concrete mixtures that may contain any number of supplementary cementitious material types

and doses, a range of water-binder ratios, and a variety of aggregate types, textures, and intrinsic reactivities. Field concrete may also encounter a wide range of temperature and humidity conditions that can affect ASR rates. The adoption of soluble alkaline-earth salts as ASR inhibitors in practice will therefore require a demonstrated predictability of how the inhibitor will function in such a wide range of conditions. Preliminary studies, not discussed here, indicate that $Ca(NO_3)_2$ additions also reduce the dissolution rates of reactive aggregates such as siliceous sandstone, gneiss, and chalcedony that are common in North America. However, more work is needed to quantify how reductions in silicate dissolution rates are related to reductions in expansion and damage measured by ASTM C1293. This knowledge base is needed to enable the development of practical admixture type and dosage guidelines as a function of an aggregate's native and inhibited dissolution rates. In addition, this will enable more accurate predictions of the service life of a structure built using concrete containing marginal aggregates that is dosed with $Ca(NO_3)_2$ or other appropriate chemical admixtures.

Chapter 7: Machine learning can predict setting behavior and strength evolution of hydrating cement systems

7.1 Chapter scope

The hydration of ordinary portland cement (PC) entails multiple concurrent chemical reactions.[222] These reactions cause extensive changes in phase assemblage and microstructure, which in turn determine the time-dependent evolution of concrete properties and performance such as setting time and compressive strength. Mature (28 d) compressive strength is the metric most commonly used to specify and qualify a concrete for structural design[4] Multi-scale simulations suggest the need to couple microstructural and mechanical models as a means to predict time-dependent mechanical properties.[223] However, these approaches are still severely limited by gaps in knowledge of OPC's hydration process and its constituent mechanisms, and are generally unable to forecast the evolution of properties and performance unless they are experimentally, and narrowly, calibrated to the specific system of interest.[223]

In the absence of knowledge needed to predict cement hydration rates and associated changes in properties, data-driven machine learning (ML) methods offer an attractive, mechanism-agnostic approach for estimating engineering properties such as the 28 d compressive strength of concrete.[223–232] Young *et al*.[24] have recently demonstrated that ML can, when trained on enough data, make reasonable estimations of the 28 d compressive strength of field-produced concretes as a function of its attributes such as water-to-cement mass ratio (w/c), aggregate content, and the content and type of mineral and chemical admixtures. Such results demonstrate the potential of ML approaches for predicting concrete performance because the data that were used therein were obtained for concrete produced under the *relatively uncontrolled* conditions of diverse construction

sites. The predictions could likely be made even more accurate by including site-specific variables such as temperature and humidity changes with time. However, the study was limited to concretes produced with Type I/II PC.

To supplement and extend existing models, the current study takes another step toward truly predictive models of concrete properties by applying ML methods to estimate the effects of OPC characteristics, such as chemical composition and fineness, on target performance characteristics such as paste setting time and mortar compressive strength. In addition, a tentative lower bound on the number of data records that are required for future estimation of other concrete properties is established. Special focus is paid to identify potential technical barriers faced by ML methods to identifying *general trends* among thousands of data points and, more importantly, to accurately predict the properties of any *one* material of interest.

7.2 Background and methods

7.2.1 *Machine learning algorithms*

Young *et al*. showed that bootstrap-aggregated (or bagged) decision tree ensembles can accurately estimate the 28 d compressive strength of concrete when trained on large datasets with potentially high inherent variability.[24] These rule-based estimators identify logical splits in data, partitioning the input space into a tree of decision nodes that are traversed until arriving at a final prediction of the target, called a leaf node. A simple operation, such as the multiplication of the input by a constant, produces the output estimation from each leaf node. A collection, or ensemble of trees are constructed, each tree being trained on different data sets and attributes, and their results are then averaged to produce the final prediction of the target.[233] This study focuses on three different

decision tree ensembles because of their ability to estimate field concrete compressive strength.[24] The first method is a bagged[x] tree ensemble, which bootstrap samples *n* different subsets of the training data with replacement to train *n* trees. Other than the random sampling from the training data, the method is deterministic in the sense that the decision nodes are chosen from among all attributes using a deterministic function such as information gain or Gini index.[234] In addition, the threshold value for splitting at a decision node is chosen to be that which optimizes that deterministic function. The second method, a random forest ensemble, differs from the bagged tree ensemble in that it selects the attribute chosen for each decision node from among a randomly chosen small subset of the attributes. The third method, called extra[xi] trees, is the same as a random forest except that the threshold value for splitting a decision node is also chosen at random instead of being prescribed by optimization of a thresholding function.[235] Other ML estimators besides these three tree ensembles were also examined, including basic linear regression and K-nearest neighbor (K-NN) regression.[236–238] The tree ensembles provided the highest prediction accuracy for every attribute, although the results of the other regression methods are also shown for comparison. All the algorithms used for estimator construction are regressors from the scikit-learn library, and can be accessed and downloaded, along with their documentation, at http://scikit-learn.org/stable/.[236]

7.2.2 *Data collection and preprocessing*

Two datasets were utilized. The first dataset was provided by the Cement and Concrete Reference Laboratory (CCRL) Proficiency Sample Program, which issues four OPCs each year for

[x] The term "bagged" is a portmanteau of the terms "bootstrap" and "aggregated".

[xi] The term "extra" is a portmanteau of the terms "extremely" and "randomized".

comprehensive physical and chemical testing by nearly 200 different laboratories. This dataset consists of measurements of 48 attributes of a given OPC sample (see Table 7), as established by ASTM test methods.[239] The second dataset is a compilation of different industry survey data supplied by the Portland Cement Association (PCA) and the National Institute of Standards and Technology (NIST), formerly the National Bureau of Standards (NBS). This dataset comprises 2211 different PCs characterized by an unknown number of testing institutions using standard test methods. It also includes the averages[xii] of 19 of the 48 attributes for each of the CCRL cements (marked in bold in Table 7). Two other attributes, normal consistency and final setting time, were also reported in the majority of records available, and so were also considered in this study (italicized in Table 7). The bolded entries in the "Chemical Tests" column of Table 7 were used as inputs to the final ML estimators, along with Blaine fineness, while the bolded and italicized entries in the "Physical Tests" column of Table 7, with the exception of Blaine fineness, were used as targets for ML prediction using these estimators.

Prior to use as inputs and targets in the machine learning estimators, the data were preprocessed to remove obvious errors and to ensure they would be compatible with all the ML algorithms used. First, on an attribute-by-attribute basis, unphysical or meaningless values were deleted. Among these were percentages outside the range of 0 % to 100 %[xiii] and unphysical values such as negative setting time or compressive strength. Second, a filter was applied to each attribute to delete any outliers, which we defined according Chauvenet's criterion[240] as more than four standard

[xii] Use of averages was necessary to ensure that no cement was over-represented in the input data to ML models, as this is known to negatively impact ML estimator performance.

[xiii] Any percentage values in excess of 100 % or below 0 % were retained only if they were physically meaningful. For example, negative percentages in autoclave expansion measurements correspond to shrinkage.

deviations from the mean of that attribute across all cements. The mean(s) were recalculated after those outliers were removed and the filter was reapplied, the process being repeated until no more outliers were identified. Less than 0.05 % of the data were discarded by this filtering for any given attribute, and the process of omitting outliers required only three iterations. Afterward, duplicate records (that is, identical cements) were deleted and any missing attributes were replaced by mean imputation, setting each missing value to the mean for the appropriate attribute as determined using data from the other cements. This is the simplest of all methods of data imputation, used in situations when data are missing completely at random, i.e., when the absence of a value is unrelated to the state of the system or values of other variables.

Of the two datasets, that from the CCRL contains the greater number of records, nearly 31 000, and has a more comprehensive list of potential attributes to be used as inputs or targets for ML estimators. However, that dataset is also missing more data, contains many more duplicates (consisting of only about 200 unique cements), and consequently was unable to train any ML estimators as accurately as the composite survey dataset. The CCRL data were incorporated in the composite survey dataset, however, by using the mean value of each attribute for each cement instead of the individual records. Randomly shuffling the order of data records proved essential for effectively training the ML estimators regardless of the algorithm used. This indicates that the ranges of attribute values are not homogeneously distributed across the different surveys in the compilation, and that leaving the data grouped by survey alone introduces an inadvertent bias in the sampling of input attributes toward one particular study. Therefore, random shuffling as implemented herein is an effective and necessary way to ameliorate that artifact.

Table 7: The cement attributes provided in the datasets, and the ASTM standards [239] (in square brackets) used to measure them. The boldfaced entries are reported consistently for nearly all cements in the full dataset, and italicized entries are reported in at least 50 % of the records in the dataset. Other entries were not consistently reported and were excluded from inputs to ML estimators. All boldfaced and italicized entries listed under "Physical Tests," with the exception of Blaine Fineness, were utilized as target attributes in this study, and as such were also excluded from inputs to ML estimators. All other entries that were excluded from inputs to ML estimators were verified to be of minimal importance to estimator performance, as outlined in Section *7.3.2*.

Chemical Tests	**Physical Tests**
SiO_2 (mass %) [C114]	*Paste Normal Consistency (%), [C187]*
Al_2O_3 (mass %) [C114]	**Vicat Paste Initial Set (minutes), [C191]**
Fe_2O_3 (mass %) [C114]	*Vicat Paste Final Set (minutes) [C191]*
CaO (mass %) [C114]	Gillmore Initial Set (minutes) [C266]
C_3S (mass %) [C150]	Gillmore Final Set (minutes) [C266]
C_2S (mass %) [C150]	False Set (%) [C451]
C_3A (mass %) [C150]	Autoclave Expansion (%) [C151]
C_4AF (mass %) [C150]	Air Content (%) [C185]
Free CaO (mass %) [C114]	Air Content Mixing Water (%) [C185]
MgO (mass %) [C114]	Air Content Mixture Flow (%) [C185]
SO_3 (mass %) [C114]	**3 Day Mortar Compressive Strength (MPa) [C109]**
Na_2O (mass %) [C114]	**7 Day Mortar Compressive Strength (MPa) [C109]**
K_2O (mass %) [C114]	**28 Day Mortar Compressive Strength (MPa) [C109]**
Loss on Ignition (mass %) [C114]	Mortar Compressive Strength Mixture Flow (%) [C109]
Insoluble Residue (mass %) [C114]	**Blaine Fineness (m^2/kg) [C204]**
Carbon Dioxide (mass %) [C114]	Wagner Fineness (m^2/kg) [C115]
Limestone (mass %) [C114]	Sieve Fineness (% passing) [C430]
ZnO (mass %) [C114]	0 Day Heat of Solution (cal/g) [C186]
Mn_2O (mass %) [C114]	7 Day Heat of Solution (cal/g) [C186]
P_2O_5 (mass %) [C114]	28 Day Heat of Solution (cal/g) [C186]
TiO_2 (mass %) [C114]	7 Day Heat of Hydration (cal/g) [C186]
Cl (mass %) [C114]	28 Day Heat of Hydration (cal/g) [C186]
	Mortar Bar Expansion (%) [C1038]
	Mortar Bar Mixing Water (%) [C1038]
	Mortar Bar Flow [C1038]

7.2.3 *Estimator optimization*

Numerous machine learning estimators were constructed and applied to predict initial set (minutes), 3 d compressive strength (MPa), 7 d compressive strength (MPa), and 28 d compressive strength (MPa). These targets were chosen because the first three affect the scheduling of construction operations, and the 28 d strength is both an input for structural design and a specification criterion. Each estimator was trained and tested on the combined datasets with the performance of each estimator being evaluated using several error metrics. Both training and testing were conducted on different portions of data using a standard low-bias resampling procedure called k-Fold Cross-Validation.[xiv,241,242] The data records were randomly split into k = 10 "folds," nine of which were used to train the estimator, and one of which was used to evaluate the estimator after training. The process was then repeated nine additional times, each time using a different fold as the test set, and the remaining nine folds as the training set.

The estimators used in this study are sensitive to the magnitude of the attributes in the sense that they will be biased to assign more importance to attributes with inherently greater values. For example, merely changing the units of Blaine fineness of the powder from m^2/kg to cm^2/g increases the numerical value by a factor of ten and can influence the accuracy of the estimators even though the physical data are the same. To address this kind of artifact, after the training and testing sets were identified and separated, the data for each attribute were rescaled to a standard normal distribution (mean = 0, variance = 1). This step was taken after the separation of the training and testing sets to avoid data leakage (i.e., the unintentional passing of information about the test set

[xiv] Cross-validation is necessary to evaluate how machine-learning estimators are likely to perform when making predictions on previously unseen data: a portion of the data are taken as a training set and used to train and optimize the model, and the remainder of the data are withheld as a testing set to evaluate the model's performance.

to the training set) which could potentially happen if the combined testing and training data were rescaled together.

Estimator optimization was performed by determining extremal values of one of three objective functions that characterize the overall fidelity of the predictions to the actual values in the testing set. The objective functions are the root mean square error (RMSE), the mean absolute percentage error (MAPE), and the coefficient of determination (R^2):

$$\mathrm{RMSE} = \sqrt{\frac{\sum_{i=1}^{n}(P_i - A_i)^2}{n}} \tag{5}$$

$$\mathrm{MAPE} = \frac{100}{n}\sum_{i=1}^{n}\left|\frac{P_i - A_i}{A_i}\right| \tag{6}$$

$$\mathrm{R}^2 = 1 - \frac{\sum_{i=1}^{n}(P_i - A_i)^2}{\sum_{i=1}^{n}(A_i - \bar{A})^2} \tag{7}$$

where n is the number of records in the testing set, P_i and A_i are the predicted and actual target value of the i^{th} record in the testing set, respectively, and $\bar{A}$ is the arithmetic average of the actual target values. RMSE and MAPE indicate the average departure of estimated values from actual values, whereas R^2 is the fraction of the variance of the target values that is predictable from the attributes using the model. As described in Section 7.3.1, low RMSE and MAPE values may still be achieved even when the data are relatively scattered and the R^2 value is low. This has also been observed previously[24] and suggests that an error-based metric such as MAPE is a better test of estimator performance than R^2 because it can be compared more directly with the acceptable range of physical test values for attributes such as setting time or strength.[239]

Each of the machine learning estimators were finalized by optimizing their estimation performance via hyperparameter tuning. This procedure varied both the number of trees used in random forest estimators and the number of attributes considered per tree split when partitioning the input space. The results of this hyperparameter tuning, shown in Figure 31, indicate that estimator performance improves only marginally beyond a certain number of trees. Consequently, the final estimators reported here employ only 100 trees to avoid over-fitting of the training data, and the extremely-random forest estimators employ only two attributes per "split," for similar reasons. These fully-optimized ML estimators are a substantial improvement (roughly a two-fold reduction in MAPE) over prior work,[24] by merit of their consideration of cement composition.

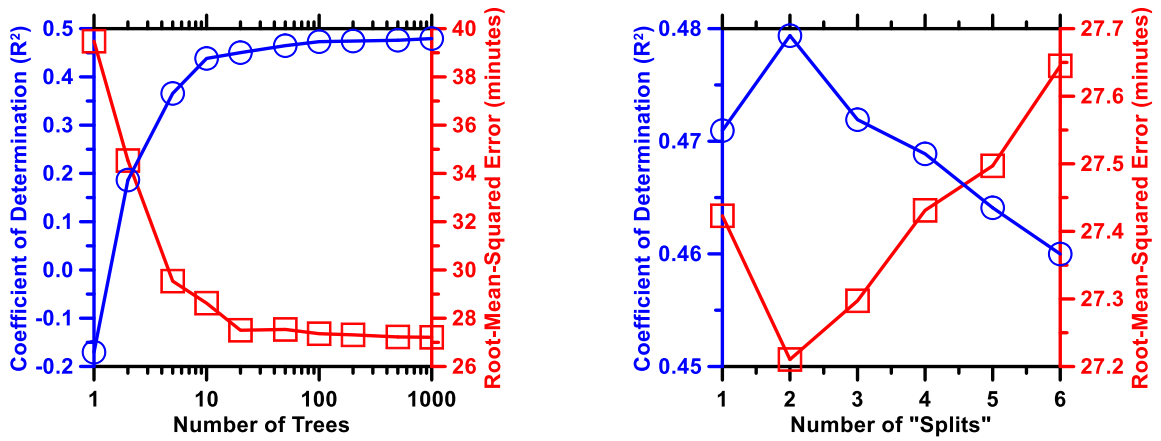

Figure 31: The results of a representative parameter tuning exercise for the extremely random forest estimators constructed to estimate initial setting time, showing: **(a)** A plateau in estimator performance with increasing number of trees (i.e., in each case using two attributes to determine each partitioning of the input space), and **(b)** A modest optimum of two splits is observed when using 1000 trees.

7.3 Results and discussion

7.3.1 *Estimation accuracy for a given target is comparable to ASTM repeatability limits*

Among the algorithms examined, ensembles of decision trees consistently produced the lowest errors, as shown in Table 8. Of the tree ensembles, the extra trees estimator most accurately estimated every primary attribute as measured by MAPE. The error metrics are not much greater in magnitude than the reported repeatability of the corresponding ASTM test methods, reported as a coefficient of variation, though there is no standard ML error parameter that would enable more direct comparisons.[239] For example, the MAPE for 7 d compressive strength predictions by extra trees estimators is 6.58 %, less than twice the single-operator coefficient of variation of the measurement using ASTM C109 (3.8%). Similarly, the variability in initial set time for that estimator, 25.5 minutes, is considerably less than the acceptable range of two successive measurements using ASTM C191 (34 minutes). This suggests that, for cement compositions covered by ASTM C150, ensemble machine learning approaches may reliably estimate the *average properties* and performance of paste / mortar formulations nearly as well or better than they can be repeatably measured in the lab.

Table 8: The results of 10-fold cross-validation using the following error metrics: root mean square error (RMSE), coefficient of determination (R^2), and mean absolute percentage error (MAPE). The input attributes were SiO_2 (mass %), Al_2O_3 (mass %), Fe_2O_3 (mass %), CaO (mass %), SO_3 (mass %), and Blaine fineness (m^2/kg), as determined by attribute importance in Section 7.3.2.

Target Attributes for Ten-Fold Cross-Validation												
	Initial Set Time[b]			**3 Day Strength[c]**			**7 Day Strength[c]**			**28 Day Strength[c]**		
Estimator	***RMSE (min)***	***R^2***	***MAPE (%)***	***RMSE (MPa)***	***R^2***	***MAPE (%)***	***RMSE (MPa)***	***R^2***	***MAPE (%)***	***RMSE (MPa)***	***R^2***	***MAPE (%)***
Linear	29.6	0.392	17.7	3.26	0.676	9.01	3.59	0.573	7.90	4.01	0.305	7.06
K-NN[a]	27.8	0.437	15.9	3.25	0.691	8.32	3.48	0.614	7.27	3.77	0.394	6.35
Decision Tree Ensemble Estimators:												
Bagged	26.2	0.524	15.0	2.79	0.766	7.29	3.18	0.668	6.67	3.50	0.489	5.91
Random	25.6	0.541	14.9	2.82	0.763	7.35	3.15	0.674	6.68	3.48	0.497	5.87
Extra	**25.5**	**0.547**	**14.7**	**2.82**	**0.762**	**7.29**	**3.14**	**0.675**	**6.58**	**3.44**	**0.506**	**5.79**
Boosted[a]	29.0	0.417	17.7	3.44	0.646	10.0	3.63	0.567	8.19	3.89	0.368	6.81
Gradient[a]	26.9	0.495	15.7	2.89	0.749	7.74	3.30	0.642	6.93	3.59	0.460	6.13

[a] K-nearest neighbors, boosted decision trees, and gradient boosted decision trees were also used, among other estimators (not shown), as they are likely to perform similarly to bagged decision trees. None performed better for these target attributes. For details regarding the implementation, see http://scikit-learn.org/stable/.
[b] ASTM C191.
[c] ASTM C109.

7.3.2 *Higher errors for late-age strength suggest missing data attributes*

Table 8 shows that estimator performance for predicting compressive strength is progressively poorer at later ages, regardless of the estimator used. For example, the RMSE of the extremely randomized forest estimator increases from 2.82 MPa at 3 d to 3.14 MPa and 3.44 MPa at 7 d and 28 d, respectively. Despite the somewhat poorer estimator performance for 28 d strength compared to earlier times, both the MAPE and RMSE for 28 d strength estimates are modestly better than those determined by Young *et al.*[24] for industrially produced concretes using similar estimators,

likely due to more detailed knowledge of mixture and material characteristics in the current study (cement composition, fineness). In any case, the greater errors at later ages may indicate that the available datasets are missing some important attributes that influence compressive strength at later ages.

One possible reason for this decrease in accuracy at later ages may be inconsistent or poorly controlled curing conditions in practice, the effects of which would become progressively more important with time. It is impossible to assess the likelihood of that possibility based on the data alone, however, because there are no requirements in ASTM C109 to report the imposed degree of control over curing temperature or moisture conditions. A second possible reason for increased error is air entrainment in some subset of the measurements, given that ASTM C109 allows the user to decide whether or not the sample will contain entrained air – macroscopic air voids stabilized by chemical admixtures to improve freeze-thaw resistance – requiring a lower water-cement mass ratio (w/c) of 0.460 than the value of 0.485 required for samples without air entrainment. Finally, differences in water content may play a significant role in poor estimator performance for initial setting time measured using ASTM C191, wherein the mixture must be prepared with "normal consistency" as measured by ASTM C187, which is the empirically determined water content required to achieve a prescribed paste stiffness after 30 s of mixing with 0.65 kg of cement powder (varying from about 22 % to 30 % of the powder mass among different PCs). Therefore, ML estimation of normal consistency has also been investigated, as it may serve as a proxy for w/c and is available in some of the compiled survey data.

Table 9: Results of 10-fold cross-validation for the final machine learning estimators of secondary targets with partial data records, evaluated using the same error metrics given in Table 7. The best-performing estimator (lowest MAPE) is marked in bold. The number of available data points used in each estimator is also reported.

Target Attribute for Ten-Fold Cross-Validation								
	Final Set				**Normal Consistency**			
Estimator	***RMSE (min)***	***R^2***	***MAPE (%)***	***Data Points***	***RMSE (%)***	***R^2***	***MAPE (%)***	***Data Points***
Linear	60.1	0.422	18.4	1144	1.04	0.292	2.96	1447
K-NN	59.6	0.432	17.6	1144	0.935	0.427	2.29	1447
Trees:								
Bagged	55.5	0.505	16.6	1144	0.920	0.446	2.28	1447
Random	55.5	0.505	16.6	1144	0.935	0.427	2.29	1447
Extra	**54.7**	**0.513**	**16.4**	1144	**0.894**	**0.471**	**2.23**	1447
Boosted	57.6	0.461	17.8	1144	1.11	0.193	3.31	1447
Gradient	57.9	0.461	17.5	1144	0.999	0.358	2.49	1447

[a]ASTM C191.
[b]ASTM C187.

7.3.3 *Secondary target estimation suggests some ability to account for missing attributes*

Among the other attributes in the dataset besides initial set and compressive strength, both normal consistency and final setting time were reported frequently enough to construct viable estimators. Estimators for these secondary targets, results of which are given in Table 9, were indeed about as accurate as those for primary targets in Table 8. However, in contrast to the primary targets, the errors in estimating normal consistency are significantly higher than the tolerances listed in its associated ASTM C187 test method. Nevertheless, the normal consistency estimators have the lowest MAPE of any estimator used in this study. ASTM C187 uses OPC pastes prepared with normal consistency, so the estimator's ability to capture the dependence of normal consistency on composition and fineness may explain why ML estimators are able to predict initial and final setting times from those same attributes despite the fact that the w/c used can be different for each

cement. In other words, cement details such as fineness are able to at least *somewhat* capture this indicator of "water demand" of a cement, but there likely are other powder characteristics – perhaps microscale texture or grinding aid type or dose – that affect normal consistency but are currently not being measured by standard test methods. This example highlights both a limitation of, and an opportunity for, ML methods: they can estimate certain aspects of concrete performance from routinely collected data, but they can also identify other performance attributes, the systematic estimation of which requires additional or perhaps qualitatively different material characterization. Similarly, as taken up in the next section, it is helpful for understanding to identify which currently measured attributes contribute most strongly to the quality of ML estimations of different targets.

7.3.4 *Selective omission identifies six attributes needed to estimate set and strength*

One can evaluate the relative importance of the different attributes in determining estimator performance in predicting the primary targets (initial set, compressive strength) by eliminating them one at a time from the training set. The corresponding increase in MAPE was used as a quantitative measure of attribute importance, as shown in Figure 32(a). Unsurprisingly, cement fineness is by far the most influential input attribute, followed by the oxides of sulfur, calcium, aluminum, silicon, and iron. Similar attribute rankings were obtained for all targets estimated. This is reassuring because (i) available surface area is well known to be a key factor that affects cement reaction rates and water demand, (ii) calcium and aluminum bearing cement phases such as tricalcium silicate (C_3S[xv]) and tricalcium aluminate (C_3A), are known to be the most reactive cement phases, and (iii) proper sulfation of a cement is empirically known to influence setting and

[xv] Conventional cement chemistry notation is used: C = CaO, S = SiO_2, A = Al_2O_3.

early-age strength gain. Predictions showed only marginal improvement upon inclusion of any other other attributes from Table 7 besides these six, such as minor oxides (Mg, Na, K), loss on ignition, or free lime content. Whether added alone or in combination with other such attributes, none affected the MAPE by more than 0.1 %. Replacing the four major oxides with the Bogue estimates of the four major clinker phases also did not improve estimator performance, which is understandable because the Bogue estimates are merely linear functions of the oxide proportions.

7.3.5 *Random omission identifies a tentative lower bound on training data needed*

Having now established the minimum attributes necessary for predicting the primary targets, we now turn attention to determining the minimum number of data records needed to make accurate target estimates. This measure of robustness of the different ML algorithms, when applied to these datasets, can be evaluated by retraining them with a sparse subset of the data. Specifically, learning curves were constructed by randomly omitting data records from the input, as illustrated in Figure 32(b). For convenience in terminology, we define "data-sufficiency" as the minimum number of data records at which the learning curves plateau. Figure 32(b) shows that the estimators approach peak performance, at least with respect to R^2, with less than 10 % of the available dataset; those trained with a random selection of at least 200 of the 2211 total available data records performed within about 1 % of the MAPE of the same estimators that were given access to the full training set. This suggests the viability of applying such estimators even for relatively smaller datasets and is an encouraging sign that these methods can also be used reliably even with limited field data. However, the error metrics frequently used to evaluate the quality of ML estimators, such as MAPE, are not necessarily suitable for the direct comparison between estimator accuracy *on*

average and the ability of the estimator to make consistently accurate predictions of engineering properties of particular cement systems.

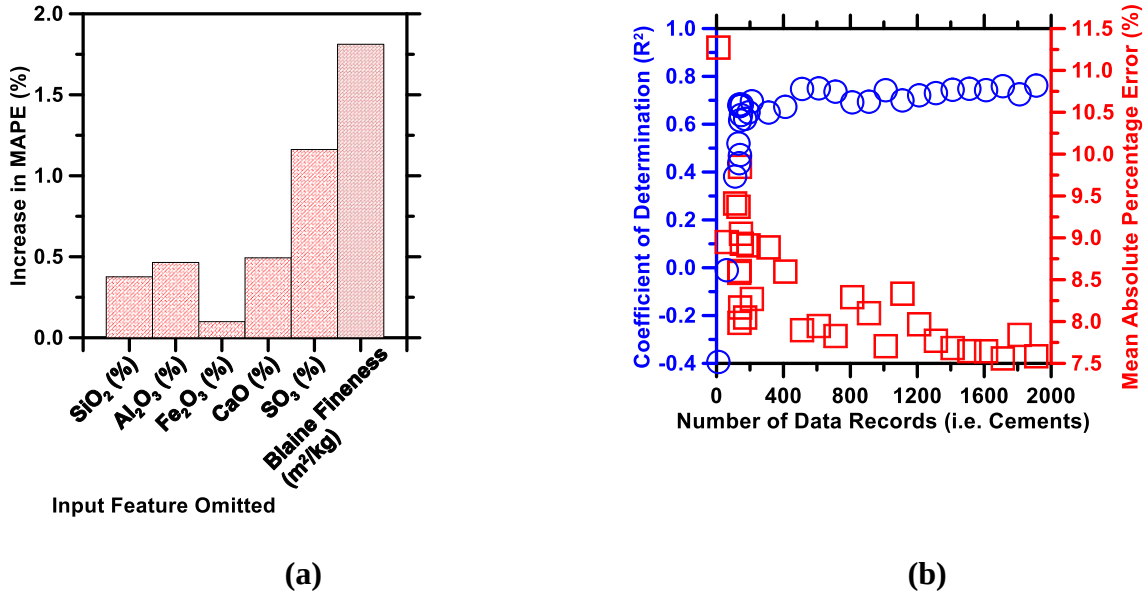

(a) **(b)**

Figure 32: Representative evaluations of estimator performance shown for the extremely random forest estimators constructed to estimate 3 d compressive strength which highlight **(a)** Attribute importance as determined by an increase in MAPE upon omission of a given input attribute, and **(b)** so-called "learning curves" for the estimator showing the minimum number of input records required to construct an adequate estimator.

7.3.6 *New evaluative metrics needed to properly reflect estimator prediction accuracy*

The three objective functions used to score the estimator performance in this study, which are among the most commonly used scoring metrics in other machine learning efforts, reflect the estimator's performance on average for the entire dataset, which comprises many cements. However, indicators of average error such as RMSE and MAPE do *not* indicate the estimator's accuracy in predicting the target value of any *particular* cement in the testing set. Just as a significant fraction of a normally distributed population lies outside one standard deviation of its mean, so does a given estimator produce individual errors much greater than the RMSE for a

significant fraction of the cements. As an example, Figure 33(a) shows the individual predictions of 28 d compressive strength made by an extremely random forest regressor with 500 trees applied to a testing set after training. The predicted value for each data record is plotted against the actual target value for that record. The RMSE for this estimator is less than 5 MPa, but the maximum error for any particular cement could be as high as 20 MPa and corresponds to a relative error of about 50 %.

To view the situation in a different way, the absolute prediction errors for 28 d strength of individual cements were collected in a histogram with 1 MPa bin widths. The histogram was converted into a normalized probability density plot, the positive portion of which is shown in Figure 33(b). For comparison, the same figure shows the corresponding histograms for 3-d compressive strength obtained in this study and for 28-d concrete strength obtained by Young *et al.*[24]. The errors have an approximately normal distribution with a peak near 2 MPa and a standard deviation of approximately 3.6 MPa. A tolerance interval for an ML estimator can then be established in a similar manner to the ASTM standard test methods. For example, given that the 28 d strength errors in Figure 33(b) are approximately normally distributed with a mean of 2 MPa and a standard deviation of 3.6 MPa, there is a 95 % probability that 90 % of the predictions will be no less than 6.2 MPa below the actual value and no more than 10.2 MPa above it. A tolerance interval this large is far from ideal. However, for comparison the interval for similar estimations from concrete mixture proportions by Young *et al.*[24] comes in at about ±15.5 MPa. As illustrated in Figure 33(b) by comparison to predictions on concrete, as well as 3 d strength, the current results clarify both the substantial improvement achieved by inclusion of attributes such as cement

composition, as well as the potential future improvements that may arise from inclusion of additional attributes such as curing conditions.

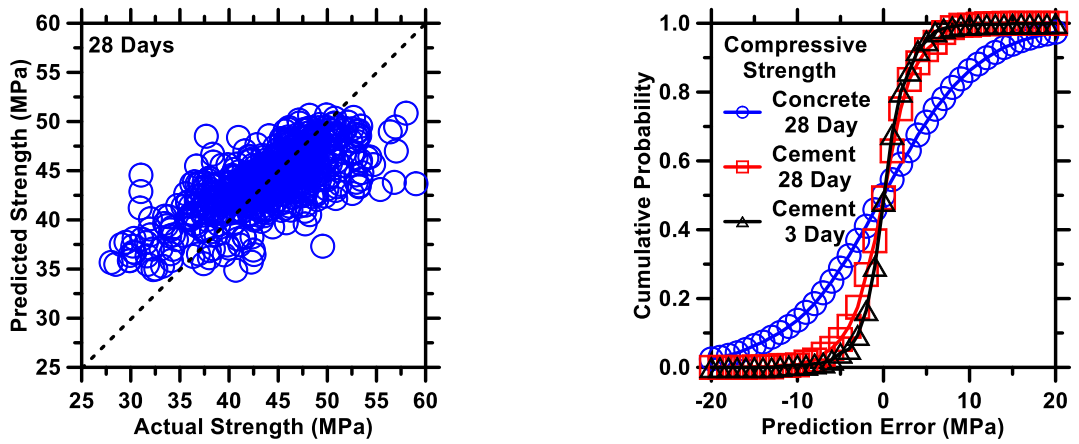

(a) **(b)**

Figure 33. The prediction results of an optimized 500-tree extremely random forest regression estimator, shown as **(a)** predicted vs actual strength values with a dashed line of identity provided to guide the eye, and **(b)** the normalized cumulative probability distribution of a prediction by the estimator having a given error. Also shown for comparison are distributions for a similar estimator applied to prediction of 3 d compressive strength of mortars (this study) and 28 d compressive strength of concretes (Young *et al.*[24]).

If ML estimators are to be used confidently for concrete mixture design and optimization, they will need to achieve much lower tolerance intervals in their predictions than are indicated herein. In statistical treatments such as those discussed above, the only way to reduce the probability that a particular estimate is outside a tolerable limit is to significantly reduce the average error values such as RMSE and MAPE, or to effectively tighten the distribution of errors about these average values. The ways to decrease average error are to provide the estimator with data that more uniformly span the range of possible values, to acquire better curated data, or to identify and collect data on other attributes that may relate more meaningfully to the target being estimated. Within the narrowly prescribed range of cement compositions and characteristics considered herein,

namely ASTM C150 PCs, the dataset would appear to be easily large enough to train the estimators according to the plateau in learning curves demonstrated in Figure 32(b). Consequently, the only feasible way to reduce the unexplained variance is to develop a means for identifying relatively more inconsistent data within the currently applied dataset, or to supplement the data with measurements of other material or processing characteristics that are currently not being routinely captured including, but not restricted to, the types and dosages of chemical admixtures, the particle size distribution of the OPC, clinker grinding parameters, curing conditions, and data on the mineralogy, texture, and impurities in the individual cement components.

7.3.7 *Under-sampling intermediate strength values reduces estimator bias*

The correlation between predicted and actual 28 d compressive strength values, as illustrated in Figure 33(a), exhibits a distinct bias: low actual compressive strength values are consistently over-predicted, while high values are consistently under-predicted. This suggests that such regression estimators, including ensemble models such as extremely random forests, suffer from an imbalance in the input data used to train them, specifically in that a scarcity of very low and very high compressive strength values leads to less accurate predictions in these ranges. This issue has been frequently addressed in the field of ML classification[243] by resampling, that is, omitting or adding data records in the ML training set. Development of this practice for regression estimators is only in its early stages,[243] with primary interest so far in its ability to allow for prediction of rare extremal values.[244] In the current case, where more accurate predictions within a narrowly prescribed range are the goal, resampling methods provide a ready means to reduce estimator bias by simply omitting a selection of the input data.

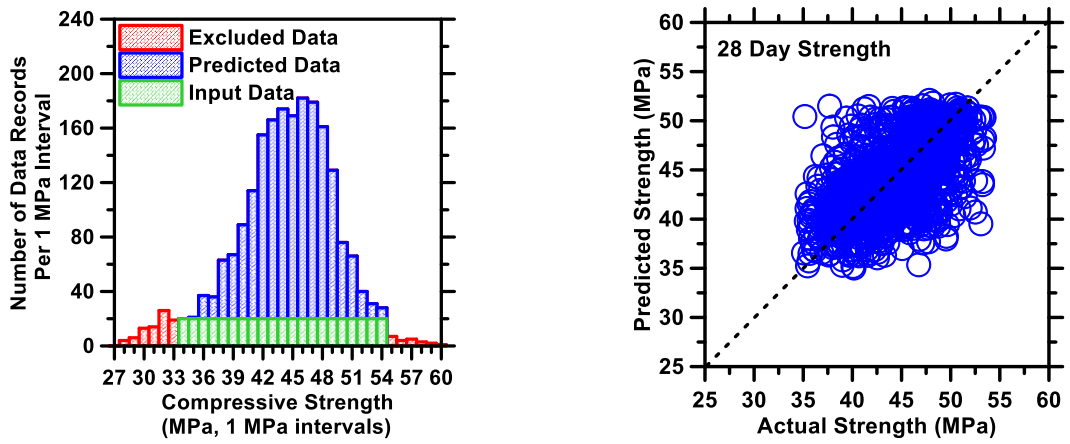

Figure 34. **(a)** The distribution of measured compressive strength values from the full dataset, with data that was used as input to train ML estimators, predictions to test ML estimators, and excluded data marked in green, blue, and red, respectively. **(b)** Prediction results of an optimized 500-tree extremely random forest regressor trained on an input set subject to under-sampling (as illustrated in part (a)), shown as predicted vs actual strength values with a dashed line of identity provided to guide the eye.

A tentative under-sampling procedure, developed specifically for the dataset under consideration, demonstrates that the input of *fewer data* is preferable when predicting the compressive strength of cement mortars (Figure 34b). The under-sampling in this case was conducted by analyzing the distribution in actual compressive strength values (Figure 34(a)), divided arbitrarily into 1 MPa intervals. About 90 % of the data records have compressive strengths between 34 MPa and 54 MPa. At least 20 data records were available within each 1 MPa interval in that range, but not outside that range. Therefore, 20 data records were randomly selected from each 1 MPa interval within the range of 34 MPa to 54 MPa, and the remainder of the records in that range were used to test prediction accuracy. The input set constructed in this manner consisted of 420 data records, more than enough to optimally train estimators according to Figure 32(b). Moreover, the new restricted training set corrected the bias in 28 d strength predictions, as can be seen by comparing Figure 34(b) with Figure 33(a).

The under-sampling procedure described above provides marginal improvements in previously discussed average error metrics; for example, R^2 for 28 d strength correlations increased from 0.506 to 0.582. However, the error in any specific prediction, as before, is still considerably larger than that achieved by repeated experimental measurements. Nonetheless, this result highlights an important guideline that should be taken into account, both when using existing datasets and when acquiring new data with a broader array of attributes: prediction bias can be reduced when the training set contains data that are more evenly spread over the entire range of possible target values. The same principle might apply to imbalances also in specific attributes, which then reduce estimator performance but are not easily identifiable. This is likely most applicable to cases for which some of the input attributes are known to vary widely, like those of concrete mixture proportions, as opposed to the relatively well-bounded cement compositions considered currently. The potential applications of under-sampling and/or over-sampling across many attributes to improve the performance of ML regression estimators represents a significant area for future research, with particular relevance to cement and concrete-type materials.

7.4 Chapter summary and conclusions

This study takes another important step toward predictive ML models of concrete properties by including the effects of OPC characteristics on the properties and performance of cement pastes and mortars. ML methods are applied to estimate 3 d, 7 d, and 28 d compressive strength and the time of initial set across numerous ASTM C150 compliant PCs – attributes that are typically measured in a laborious and time-intensive manner using standard test methods. At a minimum, accurate estimation of these properties by ML requires knowledge of the cement fineness and the

mass fractions of the oxides of silicon, aluminum, iron, calcium, and sulfur. Additionally, a lower bound of approximately 200 data records for different cements is required to enable this nature of estimations, with estimator performance improving only marginally with provision of more data records, likely due to the relatively narrow range of cement compositions and finenesses that are included. This implies that suitably-trained ML approaches may be used even when limited data are available.

A distinction of the dataset used in this study is that all the attributes and targets were measured following standard test methods that are intended to minimize the variability of measurement conditions. One advantage of this is that it enables the ML estimators to isolate and discover the influences of OPC powder characteristics on engineering performance without the complications of variability among other important parameters such as mixture proportions and curing temperature. In the field, these latter variables are not held constant and can have a decisive influence on concrete performance. However, prior applications of ensemble ML estimators to field concrete performance have demonstrated that realistic mixture proportioning, and production procedures and curing conditions can be accommodated and still yield reasonably accurate estimations of 28 d compressive strength.[24] Therefore, in a limited sense, this effort confirms the ability of ML methods to estimate how OPC powder characteristics affect binder properties, while outlining the limitations, such as the difference between an estimator's average accuracy and its accuracy in making single predictions. Tight tolerance intervals are a major goal in the ongoing effort to develop more comprehensive ML approaches to predicting the field performance of concrete with multicomponent binders. ML approaches are all the more desirable in this context,

however, because they can, if provided with suitable and sufficient data, capture the effects of variable environmental conditions and curing practices on concrete properties and performance.

Chapter 8: General conclusions and future work

8.1 Chapter scope

This chapter provides the general conclusions and suggested future work resulting from this dissertation. Detailed explanations, specifics, and outcomes of any of the subjects discussed herein can be found in each chapter of this document and in the publication record of the author.

8.2 General conclusions and future work

The two central hypotheses originally proposed in Chapter One have been partially validated, but require several qualifications:

- Dissolution rates of silicate and aluminate glasses, *are* well-described by simplified metrics derived from the composition and structure of the glass, but their relevance to development of engineering properties must be determined on a case-by-case basis, and also in terms of how they may evolve over time.
- Dissolution rates of such glasses *can* be controlled by introducing solvated ions, but the concentrations required to elicit substantial changes to engineering properties, expansion reduction during ASR as an example, are far higher than those typical to cementitious systems, necessitating consideration as to the specific ion used (feasibility of Ca vs. Al), and the specific mechanism by which it acts (mainly surface area reduction, for Ca).

With regard to the use of fly ash as a cement replacement agent, it can be concluded that its composition and structure, as distilled by the average number of broken bonds per network unit in

its glass phase (N_r), can be used to predict both the extent of reaction and rate of compressive strength gain for cement-fly ash pastes. This conclusion should be qualified in that it only applies to pastes containing a high proportion of fly ash (50% replacement by mass). While the end goal from an environmental standpoint is to replace as much cement as possible with fly ash, from a practical standpoint some fly ashes may be deemed "insufficiently reactive" based on the characterization methods developed herein. For these less-reactive fly ashes, lower cement replacement levels would be necessitated to maintain a minimum level of compressive strength development, and thus future work would be required to elucidate the overlapping influences of cement hydration and fly ash reactivity in these low-fly ash cement blends.

With regard to the use of fly ash as an alkali-silica reaction (ASR) mitigation agent, it can be concluded that under mildly alkaline conditions (pH 10) its dissolution rate is directly linked to the average number of topological constraints per network unit in its glass phase (n_c). It can furthermore be concluded that under mildly alkaline conditions, and consistent with other aluminosilicate materials, this reactivity is dictated largely by the bonds between network forming Si and Al, and only indirectly by network modifying Na and Ca, which result in a greater number of disconnected network units for charge balance. However, it should be clarified that in cases where the coordination state of network forming atoms may vary, as evidenced herein for Al in aluminoborate glass, network modifying ions also exert an additional effect dependent on their size and charge: smaller and more highly charged cations tend to favor higher coordination states of aluminum, resulting in a greater number of network bonds, higher n_c, and lower reactivity. While no such effects are expected based on simulated coordination of aluminum in the synthetic fly ash-like glasses considered herein, this is likely a fruitful area for future research given

preliminary indication that coordination alterations are possible in aluminosilicates, and indeed likely to substantially influence their reactivity.[245] Lastly, while the conclusion that dissolution of fly ash-like glass under hyper-alkaline conditions (pH 13) exhibits little to no compositional or structural dependence would suggest that associated impacts on ASR mitigation rely primarily upon a fly ash's composition (and presumably how this dictates evolution of the glass surface over time), the specifics of how it mitigates ASR are at odds with current understandings: both Ca and Al are known to slow dissolution of silicates, but lower-Ca fly ash is known to be a superior ASR mitigation agent. Again, this is another particularly fruitful area for future research, given that the low-levels of Ca and Al produced by cement hydration or fly ash leaching alone are noted to be insufficient to produce expansion reductions, i.e., ASR mitigation.

With regard to the broader role of Ca and Al in reducing dissolution and expansion rates of borosilicate glass (as a proxy for reactive aggregate during ASR), it can be concluded that while low concentrations elevate effective activation energy of dissolution, higher concentrations of Ca (as calcium nitrate), i.e., as required for precipitate formation (calcite and/or calcium-silicate hydrate), are required to observe substantial reductions in mortar expansion. The concentration dependent response highlights a new class of potential ASR mitigation agents: alkaline earth salts. Future research may aid in elucidating the benefits of particular salts in this class, as well as elaborating whether they work in tandem and do not interfere with early cement hydration. Beyond this, further work to confirm the validity of the assumption that aggregate dissolution is the rate controlling step of ASR would also be of great value, potentially through studies on the effect of calcium nitrate on realistic aggregates, as well as its effects across varied binder compositions or in the presence of other common chemical admixtures.

Finally, with regard to extending results of laboratory tests to predicting macroscopic property evolution of cementitious mixtures more generally (as necessary in complex and poorly understood cases such as ASR), it is concluded that machine learning (ML) represents a promising tool to aid future research, being readily extensible to prediction of properties beyond just compressive strength and across a variety of cement compositions. However, it also highlights the importance of proper data curation and pre-processing, the shortcomings inherent to current standard test methods (many of which may not record all information necessary to make accurate determinations), and most significantly the discrepancy between commonly accepted metrics of ML accuracy and the actual accuracy of individual predictions made by ML estimators. While this latter problem is not unique to materials chemistry, it is nonetheless a very important area for future study as, if not addressed, it alone will likely prevent the widespread adoption of ML for engineering applications simply due to the associated safety concerns posed by unreliable models. The key consideration in this case is to research algorithms that can improve ML estimators to a point at which their accuracy in individual predictions would be on par with that of standard experimental test methods (e.g., 95% confidence in any given estimation).

Chapter 9: References

(1) Cook, J.; Nuccitelli, D.; Green, S. A.; Richardson, M.; Winkler, B.; Painting, R.; Way, R.; Jacobs, P.; Skuce, A. Quantifying the Consensus on Anthropogenic Global Warming in the Scientific Literature. *Environmental research letters* **2013**, *8* (2), 024024.

(2) Lashof, D. A.; Ahuja, D. R. Relative Contributions of Greenhouse Gas Emissions to Global Warming. *Nature* **1990**, *344* (6266), 529–531.

(3) Miller, S. A.; Horvath, A.; Monteiro, P. J. Readily Implementable Techniques Can Cut Annual CO2 Emissions from the Production of Concrete by over 20%. *Environmental Research Letters* **2016**, *11* (7), 074029.

(4) Mindess, S.; Young, J. F.; Darwin, D. *Concrete*; Prentice Hall, 2003.

(5) Hendriks, C. A.; Worrell, E.; De Jager, D.; Blok, K.; Riemer, P. Emission Reduction of Greenhouse Gases from the Cement Industry. In *Proceedings of the fourth international conference on greenhouse gas control technologies*; 1998; pp 939–944.

(6) Ali, M. B.; Saidur, R.; Hossain, M. S. A Review on Emission Analysis in Cement Industries. *Renewable and Sustainable Energy Reviews* **2011**, *15* (5), 2252–2261.

(7) Mehta, P. K. Sustainable Cements and Concrete for the Climate Change Era–a Review. In *Second international conference on sustainable construction materials and technologies. Italy: Coventry University and The University of Wisconsin Milwaukee Centre for By-products Utilization*; 2010.

(8) Ponce, J. M.; Batic, O. R. Different Manifestations of the Alkali-Silica Reaction in Concrete According to the Reaction Kinetics of the Reactive Aggregate. *Cement and Concrete Research* **2006**, *36* (6), 1148–1156.

(9) Federal Highway Administration. Alkali-Aggregate Reactivity (AAR) Facts Book: Https://Www.Fhwa.Dot.Gov/Pavement/Concrete/Asr/Pubs/Hif13019.Pdf. Last Verified: August 25, 2017. U.S. Department of Transporation.

(10) Rajabipour, F.; Giannini, E.; Dunant, C.; Ideker, J. H.; Thomas, M. D. Alkali–Silica Reaction: Current Understanding of the Reaction Mechanisms and the Knowledge Gaps. *Cement and Concrete Research* **2015**, *76*, 130–146.

(11) Dhir, R. K.; Dyer, T. D.; Tang, M. C. Alkali-Silica Reaction in Concrete Containing Glass. *Materials and Structures* **2009**, *42* (10), 1451.

(12) ASTM International. Annual Book of ASTM Standards. 2012.

(13) Thomas, M. *Supplementary Cementing Materials in Concrete*; CRC Press, 2013.

(14) Provis, J. L. Geopolymers and Other Alkali Activated Materials: Why, How, and What? *Materials and Structures* **2014**, *47* (1–2), 11–25.

(15) American Coal Ash Association. Coal Combustion Product Production & Use Survey Report: Http://Www.Acaa-Usa.Org/Portals/9/Files/PDFs/RevisedFINAL2012CCPSurveyReport.Pdf, Last Verified, August 24, 2017. Published 2012.

(16) Chancey, R. T. *Characterization of Crystalline and Amorphous Phases and Respective Reactivities in a Class F Fly Ash*; The University of Texas at Austin, 2008.

(17) Chancey, R. T.; Stutzman, P.; Juenger, M. C.; Fowler, D. W. Comprehensive Phase Characterization of Crystalline and Amorphous Phases of a Class F Fly Ash. *Cement and Concrete Research* **2010**, *40* (1), 146–156.

(18) Bentz, D. P. Powder Additions to Mitigate Retardation in High-Volume Fly Ash Mixtures. *ACI Materials Journal* **2010**, *107* (5).

(19) Bentz, D. P.; Ferraris, C. F. Rheology and Setting of High Volume Fly Ash Mixtures. *Cement and Concrete Composites* **2010**, *32* (4), 265–270.

(20) Jantzen, C. M.; Brown, K. G.; Pickett, J. B. Durable Glass for Thousands of Years. *International Journal of Applied Glass Science* **2010**, *1* (1), 38–62.

(21) Oelkers, E. H.; Gislason, S. R. The Mechanism, Rates and Consequences of Basaltic Glass Dissolution: I. An Experimental Study of the Dissolution Rates of Basaltic Glass as a Function of Aqueous Al, Si and Oxalic Acid Concentration at 25 C and PH= 3 and 11. *Geochimica et Cosmochimica Acta* **2001**, *65* (21), 3671–3681.

(22) Lenton, T. M.; Britton, C. Enhanced Carbonate and Silicate Weathering Accelerates Recovery from Fossil Fuel CO2 Perturbations. *Global Biogeochemical Cycles* **2006**, *20* (3).

(23) Pignatelli, I.; Kumar, A.; Bauchy, M.; Sant, G. Topological Control on Silicates' Dissolution Kinetics. *Langmuir* **2016**, *32* (18), 4434–4439.

(24) Young, B. A.; Hall, A.; Pilon, L.; Gupta, P.; Sant, G. Can the Compressive Strength of Concrete Be Estimated from Knowledge of the Mixture Proportions?: New Insights from Statistical Analysis and Machine Learning Methods. *Cement and Concrete Research* **2019**, *115*, 379–388.

(25) Worrell, E.; Price, L.; Martin, N.; Hendriks, C.; Meida, L. O. Carbon Dioxide Emissions from the Global Cement Industry 1. *Annual Review of Energy and the Environment* **2001**, *26* (1), 303–329.

(26) Mehta, P. K. High-Performance, High-Volume Fly Ash Concrete for Sustainable Development. In *Proceedings of the international workshop on sustainable development and concrete technology*; 2004; pp 3–14.

(27) Juenger, M. C. G.; Winnefeld, F.; Provis, J. L.; Ideker, J. H. Advances in Alternative Cementitious Binders. *Cem. Concr. Res.* **2011**, *41* (12), 1232–1243.

(28) Shehata, M. H.; Thomas, M. D. Use of Ternary Blends Containing Silica Fume and Fly Ash to Suppress Expansion Due to Alkali–Silica Reaction in Concrete. *Cement and Concrete Research* **2002**, *32* (3), 341–349.

(29) Bentz, D. P. Powder Additions to Mitigate Retardation in High-Volume Fly Ash Mixtures. *ACI Materials Journal* **2010**, *107* (5).

(30) Bentz, D. P.; Ferraris, C. F. Rheology and Setting of High Volume Fly Ash Mixtures. *Cement and Concrete Composites* **2010**, *32* (4), 265–270.

(31) Chancey, R. T. Characterization of Crystalline and Amorphous Phases and Respective Reactivities in a Class F Fly Ash, University of Texas at Austin, 2008.

(32) Chancey, R. T.; Stutzman, P.; Juenger, M. C.; Fowler, D. W. Comprehensive Phase Characterization of Crystalline and Amorphous Phases of a Class F Fly Ash. *Cement and Concrete Research* **2010**, *40* (1), 146–156.

(33) ASTM Standards Website. Available at: Http://Www.Astm.Org/Standards/. Accessed on 3/9/2015 at 3:03 p.m. PST.

(34) Mehta, P. K. Influence of Fly Ash Characteristics on the Strength of Portland-Fly Ash Mixtures. *Cement and Concrete Research* **1985**, *15* (4), 669–674.

(35) Berry, E. E.; Hemmings, R. T.; Cornelius, B. J. Mechanisms of Hydration Reactions in High Volume Fly Ash Pastes and Mortars. *Cement and Concrete Composites* **1990**, *12* (4), 253–261.

(36) Papadakis, V. G. Effect of Fly Ash on Portland Cement Systems: Part I. Low-Calcium Fly Ash. *Cement and Concrete Research* **1999**, *29* (11), 1727–1736.

(37) Papadakis, V. G. Effect of Fly Ash on Portland Cement Systems: Part II. High-Calcium Fly Ash. *Cement and Concrete Research* **2000**, *30* (10), 1647–1654.

(38) Lam, L.; Wong, Y. L.; Poon, C. S. Degree of Hydration and Gel/Space Ratio of High-Volume Fly Ash/Cement Systems. *Cement and Concrete Research* **2000**, *30* (5), 747–756.

(39) Sakai, E.; Miyahara, S.; Ohsawa, S.; Lee, S.-H.; Daimon, M. Hydration of Fly Ash Cement. *Cement and Concrete Research* **2005**, *35* (6), 1135–1140.

(40) Roy, D. M.; Luke, K.; Diamond, S. Characterization of Fly Ash and Its Reactions in Concrete. In *MRS Proceedings*; Cambridge Univ Press, 1984; Vol. 43, p 3.

(41) Pietersen, H. S. Reactivity of Fly Ash and Slag in Cement, TU Delft, Delft University of Technology, 1993.

(42) Aughenbaugh, K. L.; Chancey, R. T.; Stutzman, P.; Juenger, M. C.; Fowler, D. W. An Examination of the Reactivity of Fly Ash in Cementitious Pore Solutions. *Materials and structures* **2013**, *46* (5), 869–880.

(43) Snellings, R. Surface Chemistry of Calcium Aluminosilicate Glasses. *Journal of the American Ceramic Society* **2015**, *98* (1), 303–314.

(44) Le Saoût, G.; Kocaba, V.; Scrivener, K. Application of the Rietveld Method to the Analysis of Anhydrous Cement. *Cement and concrete research* **2011**, *41* (2), 133–148.

(45) Berge, A.; Adl-Zarrabi, B.; Hagentoft, C.-E. Determination of Specific Heat Capacity by Transient Plane Source. *Frontiers of Architectural Research* **2013**, *2* (4), 476–482.

(46) Yue, Y.-Z. Characteristic Temperatures of Enthalpy Relaxation in Glass. *Journal of Non-Crystalline Solids* **2008**, *354* (12), 1112–1118.

(47) Varshneya, A. K. *Fundamentals of Inorganic Glasses*; Elsevier, 1993.

(48) Winburn, R. S.; Grier, D. G.; McCarthy, G. J.; Peterson, R. B. Rietveld Quantitative X-Ray Diffraction Analysis of NIST Fly Ash Standard Reference Materials. *Powder Diffraction* **2000**, *15* (03), 163–172.

(49) Abràmoff, M. D.; Magalhães, P. J.; Ram, S. J. Image Processing with ImageJ. *Biophotonics international* **2004**, *11* (7), 36–42.

(50) Biehl, L.; Landgrebe, D. MultiSpec—a Tool for Multispectral–Hyperspectral Image Data Analysis. *Computers & Geosciences* **2002**, *28* (10), 1153–1159.

(51) Janoušek, V.; Farrow, C. M.; Erban, V. Interpretation of Whole-Rock Geochemical Data in Igneous Geochemistry: Introducing Geochemical Data Toolkit (GCDkit). *Journal of Petrology* **2006**, *47* (6), 1255–1259.

(52) Oey, T.; Kumar, A.; Bullard, J. W.; Neithalath, N.; Sant, G. The Filler Effect: The Influence of Filler Content and Surface Area on Cementitious Reaction Rates. *Journal of the American Ceramic Society* **2013**, *96* (6), 1978–1990.

(53) Kumar, A.; Oey, T.; Kim, S.; Thomas, D.; Badran, S.; Li, J.; Fernandes, F.; Neithalath, N.; Sant, G. Simple Methods to Estimate the Influence of Limestone Fillers on Reaction and Property Evolution in Cementitious Materials. *Cement and Concrete Composites* **2013**, *42*, 20–29.

(54) Diamond, S. The Utilization of Flyash. *Cement and concrete Research* **1984**, *14* (4), 455–462.

(55) Diamond, S. On the Glass Present in Low-Calcium and in High-Calcium Flyashes. *Cement and Concrete Research* **1983**, *13* (4), 459–464.

(56) Oh, J. E.; Jun, Y.; Jeong, Y.; Monteiro, P. J. The Importance of the Network-Modifying Element Content in Fly Ash as a Simple Measure to Predict Its Strength Potential for Alkali-Activation. *Cement and Concrete Composites* **2015**, *57*, 44–54.

(57) Shelby, J. E. *Introduction to Glass Science and Technology*; Royal Society of Chemistry, 2005.

(58) Kingery, W. D.; Bowen, H. K.; Uhlmann, D. R. Introduction to Ceramics, 1976. *Jhon Willey & Sons, New York*.

(59) Hemmings, R. T.; Berry, E. E. On the Glass in Coal Fly Ashes: Recent Advances. In *MRS Proceedings*; Cambridge Univ Press, 1987; Vol. 113, p 3.

(60) Neuville, D. R.; Cormier, L.; Flank, A.-M.; Briois, V.; Massiot, D. Al Speciation and Ca Environment in Calcium Aluminosilicate Glasses and Crystals by Al and Ca K-Edge X-Ray Absorption Spectroscopy. *Chemical Geology* **2004**, *213* (1), 153–163.

(61) Avramov, I.; Vassilev, T.; Penkov, I. The Glass Transition Temperature of Silicate and Borate Glasses. *Journal of non-crystalline solids* **2005**, *351* (6), 472–476.

(62) Avramov, I.; Rüssel, C.; Keding, R. Effect of Chemical Composition on Viscosity of Oxide Glasses. *Journal of non-crystalline solids* **2003**, *324* (1), 29–35.

(63) Mazurin, O. V. *Handbook of Glass Data*; Elsevier. Distributors for the US and Canada, Elsevier Science Pub. Co., 1983.

(64) Cormier, L.; Neuville, D. R.; Calas, G. Relationship Between Structure and Glass Transition Temperature in Low-Silica Calcium Aluminosilicate Glasses: The Origin of the Anomaly at Low Silica Content. *Journal of the American Ceramic Society* **2005**, *88* (8), 2292–2299.

(65) Durdziński, P. T.; Dunant, C. F.; Haha, M. B.; Scrivener, K. L. A New Quantification Method Based on SEM-EDS to Assess Fly Ash Composition and Study the Reaction of Its Individual Components in Hydrating Cement Paste. *Cement and Concrete Research* **2015**, *73*, 111–122.

(66) Diamond, S. Particle Morphologies in Fly Ash. *Cem. Concr. Res.* **1986**, *16* (4), 569–579.

(67) Bentz, D. P.; Ferraris, C. F.; De la Varga, I.; Peltz, M. A.; Winpigler, J. Mixture Proportioning Options for Improving High Volume Fly Ash Concretes. *Int. J. Pavement Res. Technol.* **2010**, *3* (5), 234–240.

(68) Biernacki, J. J.; Mogulla, N. R.; Bollig, J.; Bijou, M. Kinetics of Carbon Oxidation from Fly Ash. *Fuel* **2010**, *89* (5), 1077–1086.

(69) Külaots, I.; Hurt, R. H.; Suuberg, E. M. Size Distribution of Unburned Carbon in Coal Fly Ash and Its Implications. *Fuel* **2004**, *83* (2), 223–230.

(70) Berry, E. E.; Hemmings, R. T.; Zhang, M.-H.; Cornelius, B. J.; Golden, D. M. Hydration in High-Volume Fly Ash Concrete Binders. *ACI Materials Journal* **1994**, *91* (4).

(71) Bentz, D. P.; Durán-Herrera, A.; Galvez-Moreno, D. Comparison of ASTM C311 Strength Activity Index Testing vs. Testing Based on Constant Volumetric Proportions. *J ASTM Int* **2012**, *9* (1), 7.

(72) Bentz, D. P.; Barrett, T.; De la Varga, I.; Weiss, W. J. Relating Compressive Strength to Heat Release in Mortars. *Adv Civ Eng Mater* **2012**, *1* (1), 14.

(73) Qomi, M. A.; Krakowiak, K. J.; Bauchy, M.; Stewart, K. L.; Shahsavari, R.; Jagannathan, D.; Brommer, D. B.; Baronnet, A.; Buehler, M. J.; Yip, S.; et al. Combinatorial Molecular Optimization of Cement Hydrates. *Nature Communications* **2014**, *5*.

(74) Malhotra, V. M. Fly Ash, Slag, Silica Fume, and Rice-Husk Ash in Concrete: A Review. *Concrete International* **1993**, *15* (4).

(75) Rivera, F.; Martínez, P.; Castro, J.; López, M. Massive Volume Fly-Ash Concrete: A More Sustainable Material with Fly Ash Replacing Cement and Aggregates. *Cement and Concrete Composites* **2015**, *63*, 104–112.

(76) Mehta, P. K. Influence of Fly Ash Characteristics on the Strength of Portland-Fly Ash Mixtures. *Cement and Concrete Research* **1985**, *15* (4), 669–674.

(77) Papadakis, V. G. Effect of Fly Ash on Portland Cement Systems: Part I. Low-Calcium Fly Ash. *Cement and Concrete Research* **1999**, *29* (11), 1727–1736.

(78) Papadakis, V. G. Effect of Fly Ash on Portland Cement Systems: Part II. High-Calcium Fly Ash. *Cement and Concrete Research* **2000**, *30* (10), 1647–1654.

(79) Roy, D. M.; Luke, K.; Diamond, S. Characterization of Fly Ash and Its Reactions in Concrete. In *MRS Proceedings*; Cambridge Univ Press, 1984; Vol. 43, p 3.

(80) Aughenbaugh, K. L.; Chancey, R. T.; Stutzman, P.; Juenger, M. C.; Fowler, D. W. An Examination of the Reactivity of Fly Ash in Cementitious Pore Solutions. *Materials and structures* **2013**, *46* (5), 869–880.

(81) Snellings, R. Surface Chemistry of Calcium Aluminosilicate Glasses. *Journal of the American Ceramic Society* **2015**, *98* (1), 303–314.

(82) Oey, T.; Huang, C.; Worley, R.; Ho, S.; Timmons, J.; Cheung, K. L.; Kumar, A.; Bauchy, M.; Sant, G. Linking Fly Ash Composition to Performance in Cementitious Systems. In *2015 World of Coal Ash (WOCA) Conference in Nashville, TN - May 5-7, 2015*; 2015.

(83) Kumar, A.; Reed, J.; Sant, G. Vertical Scanning Interferometry: A New Method to Measure the Dissolution Dynamics of Cementitious Minerals. *Journal of the American Ceramic Society* **2013**, *96* (9), 2766–2778.

(84) Pignatelli, I.; Kumar, A.; Shah, K.; Balonis, M.; Bauchy, M.; Wu, B.; Sant, G. Vertical Scanning Interferometry: A New Method to Quantify Re-/de-Mineralization Dynamics of Dental Enamel. *Dental Materials* **2016**.

(85) Pignatelli, I.; Kumar, A.; Alizadeh, R.; Le Pape, Y.; Bauchy, M.; Sant, G. A Dissolution-Precipitation Mechanism Is at the Origin of Concrete Creep in Moist Environments. *The Journal of Chemical Physics* **2016**, *145* (5), 054701.

(86) Hellmann, R.; Cotte, S.; Cadel, E.; Malladi, S.; Karlsson, L. S.; Lozano-Perez, S.; Cabié, M.; Seyeux, A. Nanometre-Scale Evidence for Interfacial Dissolution-Reprecipitation Control of Silicate Glass Corrosion. *Nature materials* **2015**, *14* (3), 307.

(87) Cailleteau, C.; Devreux, F.; Spalla, O.; Angeli, F.; Gin, S. Why Do Certain Glasses with a High Dissolution Rate Undergo a Low Degree of Corrosion? *The Journal of Physical Chemistry C* **2011**, *115* (13), 5846–5855.

(88) Bennett, P. C.; Melcer, M. E.; Siegel, D. I.; Hassett, J. P. The Dissolution of Quartz in Dilute Aqueous Solutions of Organic Acids at 25 C. *Geochimica et Cosmochimica Acta* **1988**, *52* (6), 1521–1530.

(89) Dove, P. M.; Crerar, D. A. Kinetics of Quartz Dissolution in Electrolyte Solutions Using a Hydrothermal Mixed Flow Reactor. *Geochimica et Cosmochimica Acta* **1990**, *54* (4), 955–969.

(90) Myers, R. J.; Geng, G.; Li, J.; Rodríguez, E. D.; Ha, J.; Kidkhunthod, P.; Sposito, G.; Lammers, L. N.; Kirchheim, A. P.; Monteiro, P. J. The Role of Adsorption Phenomena in Cubic Tricalcium Aluminate Dissolution. *Langmuir* **2016**.

(91) Bauchy, M. Structural, Vibrational, and Elastic Properties of a Calcium Aluminosilicate Glass from Molecular Dynamics Simulations: The Role of the Potential. *The Journal of chemical physics* **2014**, *141* (2), 024507.

(92) Du, J.; Cormack, A. N. The Medium Range Structure of Sodium Silicate Glasses: A Molecular Dynamics Simulation. *Journal of Non-Crystalline Solids* **2004**, *349*, 66–79.

(93) Cormack, A. N.; Du, J. Molecular Dynamics Simulations of Soda–Lime–Silicate Glasses. *Journal of non-crystalline solids* **2001**, *293*, 283–289.

(94) Du, J.; Corrales, L. R. Compositional Dependence of the First Sharp Diffraction Peaks in Alkali Silicate Glasses: A Molecular Dynamics Study. *Journal of non-crystalline solids* **2006**, *352* (30), 3255–3269.

(95) Wang, B.; Yu, Y.; Lee, Y. J.; Bauchy, M. Intrinsic Nano-Ductility of Glasses: The Critical Role of Composition. *Frontiers in Materials* **2015**, *2*, 11.

(96) Bauchy, M.; Micoulaut, M. Atomic Scale Foundation of Temperature-Dependent Bonding Constraints in Network Glasses and Liquids. *Journal of Non-Crystalline Solids* **2011**, *357* (14), 2530–2537.

(97) Phillips, J. C. Topology of Covalent Non-Crystalline Solids I: Short-Range Order in Chalcogenide Alloys. *Journal of Non-Crystalline Solids* **1979**, *34* (2), 153–181.

(98) Mauro, J. C. Topological Constraint Theory of Glass. *American Ceramic Society Bulletin* **2011**, *90* (4), 31.

(99) Bauchy, M.; Abdolhosseini Qomi, M. J.; Bichara, C.; Ulm, F.-J.; Pellenq, R. J.-M. Nanoscale Structure of Cement: Viewpoint of Rigidity Theory. *The Journal of Physical Chemistry C* **2014**, *118* (23), 12485–12493.

(100) Maraghechi, H.; Rajabipour, F.; Pantano, C. G.; Burgos, W. D. Effect of Calcium on Dissolution and Precipitation Reactions of Amorphous Silica at High Alkalinity. *Cement and Concrete Research* **2016**, *87*, 1–13.

(101) Hamilton, J. P. *Corrosion Behavior of Sodium Aluminosilicate Glasses and Crystals*; 1999.

(102) Shelby, J. E. *Introduction to Glass Science and Technology*; Royal Society of Chemistry, 2005.

(103) Hamilton, J. P.; Brantley, S. L.; Pantano, C. G.; Criscenti, L. J.; Kubicki, J. D. Dissolution of Nepheline, Jadeite and Albite Glasses: Toward Better Models for Aluminosilicate Dissolution. *Geochimica et Cosmochimica Acta* **2001**, *65* (21), 3683–3702.

(104) Boolchand, P.; Zhang, M.; Goodman, B. Influence of One-Fold-Coordinated Atoms on Mechanical Properties of Covalent Networks. *Physical Review B* **1996**, *53* (17), 11488.

(105) Chancey, R. T. *Characterization of Crystalline and Amorphous Phases and Respective Reactivities in a Class F Fly Ash*; ProQuest, 2008.

(106) Hamilton, J. P. *Corrosion Behavior of Sodium Aluminosilicate Glasses and Crystals*; 1999.

(107) Donald, I. W. Preparation, Properties and Chemistry of Glass-and Glass-Ceramic-to-Metal Seals and Coatings. *Journal of materials science* **1993**, *28* (11), 2841–2886.

(108) Ezz-Eldin, F. M. Leaching and Mechanical Properties of Cabal Glasses Developed as Matrices for Immobilization High-Level Wastes. *Nuclear Instruments and Methods in Physics Research Section B: Beam Interactions with Materials and Atoms* **2001**, *183* (3), 285–300.

(109) Varshneya, A. K. *Fundamentals of Inorganic Glasses*; Elsevier, 2013.

(110) Brow, R. K.; Watkins, R. D. Sealing Glasses for Titanium and Titanium Alloys. 5104738, April 1992.

(111) Brow, R. K.; Watkins, R. D. High Expansion, Lithium Corrosion Resistant Sealing Glasses. 5021307, June 1991.

(112) Brow, R. K.; Watkins, R. D. High Expansion, Lithium Corrosion Resistant Sealing Glasses. 5015530, May 1991.

(113) Bengisu, M.; Brow, R. K.; Yilmaz, E.; Moguš-Milanković, A.; Reis, S. T. Aluminoborate and Aluminoborosilicate Glasses with High Chemical Durability and the Effect of P 2 O 5 Additions on the Properties. *Journal of non-crystalline solids* **2006**, *352* (32), 3668–3676.

(114) Bunker, B. C.; Kirkpatrick, R. J.; Brow, R. K. Local Structure of Alkaline-Earth Boroaluminate Crystals and Glasses: I, Crystal Chemical Concepts—Structural Predictions and Comparisons to Known Crystal Structures. *Journal of the American Ceramic Society* **1991**, *74* (6), 1425–1429.

(115) Bunker, B. C.; Kirkpatrick, R. J.; Brow, R. K.; Turner, G. L.; Nelson, C. Local Structure of Alkaline-Earth Boroaluminate Crystals and Glasses: II, 11B and 27Al MAS NMR Spectroscopy of Alkaline-Earth Boroaluminate Glasses. *Journal of the American Ceramic Society* **1991**, *74* (6), 1430–1438.

(116) Brow, R. K.; Tallant, D. R. Structural Design of Sealing Glasses. *Journal of Non-Crystalline Solids* **1997**, *222*, 396–406.

(117) Pignatelli, I.; Kumar, A.; Field, K. G.; Wang, B.; Yu, Y.; Le Pape, Y.; Bauchy, M.; Sant, G. Direct Experimental Evidence for Differing Reactivity Alterations of Minerals Following Irradiation: The Case of Calcite and Quartz. *Scientific reports* **2016**, *6*.

(118) Oey, T.; Kumar, A.; Pignatelli, I.; Yu, Y.; Neithalath, N.; Bullard, J. W.; Bauchy, M.; Sant, G. Topological Controls on the Dissolution Kinetics of Glassy Aluminosilicates. *Journal of the American Ceramic Society* **2017**.

(119) Oey, T.; Hsiao, Y.-H.; Callagon, E.; Wang, B.; Bauchy, M.; Sant, G. N. Rate Controls on Silicate Dissolution in Cementitious Environments. *RILEM Technical Letters* **2017**, *2*, 67–73.

(120) Hsiao, Y.-H.; La Plante, E. C.; Krishnan, N. A.; Le Pape, Y.; Neithalath, N.; Bauchy, M.; Sant, G. Effects of Irradiation on Albite's Chemical Durability. *The Journal of Physical Chemistry A* **2017**, *121* (41), 7835–7845.

(121) Wang, M.; Pignatelli, I.; Oey, T.; Smedskjaer, M. M.; Mauro, J. C.; Sant, G.; Bauchy, M. Topological Model of the Dissolution Kinetics of Silicate Glasses. In *12th Pacific Rim Conference on Ceramic and Glass Technology*; 2017.

(122) Januchta, K.; Bauchy, M.; Youngman, R. E.; Rzoska, S. J.; Bockowski, M.; Smedskjaer, M. M. Modifier Field Strength Effects on Densification Behavior and Mechanical

Properties of Alkali Aluminoborate Glasses. *Physical Review Materials* **2017**, *1* (6), 063603.

(123) Mascaraque, N.; Januchta, K.; Frederiksen, K. F.; Youngman, R. E.; Bauchy, M.; Smedskjaer, M. M. Structural Dependence of Chemical Durability in Modified Aluminoborate Glasses. *arXiv:1805.05191 [cond-mat]* **2018**.

(124) Frederiksen, K. F.; Januchta, K.; Mascaraque, N.; Youngman, R. E.; Bauchy, M.; Rzoska, S. J.; Bockowski, M.; Smedskjaer, M. M. Structural Compromise between High Hardness and Crack Resistance in Aluminoborate Glasses. *J. Phys. Chem. B* **2018**. https://doi.org/10.1021/acs.jpcb.8b02905.

(125) Mascaraque, N.; Bauchy, M.; Smedskjaer, M. M. Correlating the Network Topology of Oxide Glasses with Their Chemical Durability. *The Journal of Physical Chemistry B* **2017**, *121* (5), 1139–1147.

(126) Mascaraque, N.; Bauchy, M.; Fierro, J. L. G.; Rzoska, S. J.; Bockowski, M.; Smedskjaer, M. M. Dissolution Kinetics of Hot Compressed Oxide Glasses. *The Journal of Physical Chemistry B* **2017**, *121* (38), 9063–9072.

(127) Züchner, L.; Chan, J. C.; Müller-Warmuth, W.; Eckert, H. Short-Range Order and Site Connectivities in Sodium Aluminoborate Glasses: I. Quantification of Local Environments by High-Resolution 11B, 23Na, and 27Al Solid-State NMR. *The Journal of Physical Chemistry B* **1998**, *102* (23), 4495–4506.

(128) Conradt, R. Chemical Durability of Oxide Glasses in Aqueous Solutions: A Review. *Journal of the American Ceramic Society* **2008**, *91* (3), 728–735.

(129) Kim, M.; Corkhill, C. L.; Hyatt, N. C.; Heo, J. Development, Characterization and Dissolution Behavior of Calcium-Aluminoborate Glass Wasteforms to Immobilize Rare-Earth Oxides. *Scientific reports* **2018**, *8* (1), 5320.

(130) Cailleteau, C.; Angeli, F.; Devreux, F.; Gin, S.; Jestin, J.; Jollivet, P.; Spalla, O. Insight into Silicate-Glass Corrosion Mechanisms. *Nature materials* **2008**, *7* (12), 978–983.

(131) Cailleteau, C.; Devreux, F.; Spalla, O.; Angeli, F.; Gin, S. Why Do Certain Glasses with a High Dissolution Rate Undergo a Low Degree of Corrosion? *The Journal of Physical Chemistry C* **2011**, *115* (13), 5846–5855.

(132) Casey, W. H.; Westrich, H. R. Control of Dissolution Rates of Orthosilicate Minerals by Divalent Metal-Oxygen Bonds. *Nature* **1992**, *355* (6356), 157.

(133) Velbel, M. A. Bond Strength and the Relative Weathering Rates of Simple Orthosilicates. *American Journal of Science* **1999**, *299* (7–9), 679–696.

(134) Kjeldsen, J.; Smedskjaer, M. M.; Mauro, J. C.; Yue, Y. Hardness and Incipient Plasticity in Silicate Glasses: Origin of the Mixed Modifier Effect. *Applied Physics Letters* **2014**, *104* (5), 051913.

(135) Tuller, H. L.; Button, D. P.; Uhlmann, D. R. Fast Ion Transport in Oxide Glasses. *Journal of Non-Crystalline Solids* **1980**, *40* (1–3), 93–118.

(136) Jain, H.; Peterson, N. L. Impurity Alkali Diffusion in Sodium-Cesium Silicate Glasses. *Journal of the American Ceramic Society* **1983**, *66* (3), 174–176.

(137) Tsomaia, N.; Brantley, S. L.; Hamilton, J. P.; Pantano, C. G. NMR Evidence for Formation of Octahedral and Tetrahedral Al and Repolymerization of the Si Network during Dissolution of Aluminosilicate Glass and Crystal. *American Mineralogist* **2003**, *88* (1), 54–67.

(138) Criscenti, L. J.; Brantley, S. L.; Mueller, K. T.; Tsomaia, N.; Kubicki, J. D. Theoretical and 27 Al CPMAS NMR Investigation of Aluminum Coordination Changes during Aluminosilicate Dissolution. *Geochimica et Cosmochimica Acta* **2005**, *69* (9), 2205–2220.

(139) Bauchy, M.; Qomi, M. J. A.; Bichara, C.; Ulm, F.-J.; Pellenq, R. J.-M. Rigidity Transition in Materials: Hardness Is Driven by Weak Atomic Constraints. *Physical review letters* **2015**, *114* (12), 125502.

(140) Smedskjaer, M. M.; Mauro, J. C.; Yue, Y. Prediction of Glass Hardness Using Temperature-Dependent Constraint Theory. *Physical review letters* **2010**, *105* (11), 115503.

(141) Wang, B.; Krishnan, N. A.; Yu, Y.; Wang, M.; Le Pape, Y.; Sant, G.; Bauchy, M. Irradiation-Induced Topological Transition in SiO 2: Structural Signature of Networks' Rigidity. *Journal of Non-Crystalline Solids* **2017**, *463*, 25–30.

(142) Bauchy, M.; Micoulaut, M. Transport Anomalies and Adaptative Pressure-Dependent Topological Constraints in Tetrahedral Liquids: Evidence for a Reversibility Window Analogue. *Physical review letters* **2013**, *110* (9), 095501.

(143) Collin, M.; Fournier, M.; Frugier, P.; Charpentier, T.; Moskura, M.; Deng, L.; Ren, M.; Du, J.; Gin, S. Structure of International Simple Glass and Properties of Passivating Layer Formed in Circumneutral PH Conditions. *npj Materials Degradation* **2018**, *2* (1), 4.

(144) Oey, T.; Timmons, J.; Stutzman, P.; Bullard, J. W.; Balonis, M.; Bauchy, M.; Sant, G. An Improved Basis for Characterizing Suitability of Fly Ash as a Cement Replacement Agent. *J Am Ceram Soc* n/a-n/a. https://doi.org/10.1111/jace.14974.

(145) Durdziński, P. T.; Dunant, C. F.; Haha, M. B.; Scrivener, K. L. A New Quantification Method Based on SEM-EDS to Assess Fly Ash Composition and Study the Reaction of Its Individual Components in Hydrating Cement Paste. *Cement and Concrete Research* **2015**, *73*, 111–122.

(146) Van Hoek, E. R.; Winter, R. Amorphous Silica and the Intergranular Structure of Nanocrystalline Silica. *Physics and Chemistry of Glasses* **2004**, *43* (C; SPI), 80–84.

(147) Diamond, S. The Utilization of Flyash. *Cement and concrete Research* **1984**, *14* (4), 455–462.

(148) Diamond, S. On the Glass Present in Low-Calcium and in High-Calcium Flyashes. *Cement and Concrete Research* **1983**, *13* (4), 459–464.

(149) Oey, T.; Frederiksen, K. F.; Mascaraque, N.; Youngman, R.; Balonis, M.; Smedskjaer, M. M.; Bauchy, M.; Sant, G. The Role of the Network-Modifier's Field-Strength in the Chemical Durability of Aluminoborate Glasses. *Journal of Non-Crystalline Solids* **2019**, *505*, 279–285.

(150) Oey, T.; Callagon, E.; Falzone, G.; Hsiao, Y.-H.; Wada, A.; Monfardini, L.; Bauchy, M.; Bullard, J. W.; Sant, G. Calcium Nitrate: A Chemical Admixture to Inhibit Aggregate Dissolution and Mitigate Expansion Caused by Alkali-Silica Reaction. *Cement and Concrete Composites* **2019**, *Submitted Pending Review*.

(151) Hellmann, R.; Cotte, S.; Cadel, E.; Malladi, S.; Karlsson, L. S.; Lozano-Perez, S.; Cabié, M.; Seyeux, A. Nanometre-Scale Evidence for Interfacial Dissolution–Reprecipitation Control of Silicate Glass Corrosion. *Nature materials* **2015**, *14* (3), 307–311.

(152) Hellmann, R.; Wirth, R.; Daval, D.; Barnes, J.-P.; Penisson, J.-M.; Tisserand, D.; Epicier, T.; Florin, B.; Hervig, R. L. Unifying Natural and Laboratory Chemical Weathering with Interfacial Dissolution–Reprecipitation: A Study Based on the Nanometer-Scale Chemistry of Fluid–Silicate Interfaces. *Chemical Geology* **2012**, *294*, 203–216.

(153) Hamilton, J. P.; Pantano, C. G. Effects of Glass Structure on the Corrosion Behavior of Sodium-Aluminosilicate Glasses. *Journal of non-crystalline solids* **1997**, *222*, 167–174.

(154) Angeli, F.; Boscarino, D.; Gin, S.; Mea, G. D.; Boizot, B.; Petit, J. C. Influence of Calcium on Sodium Aluminosilicate Glass Leaching Behaviour. *Physics and chemistry of glasses* **2001**, *42* (4–5), 279–286.

(155) Brantley, S. L. Reaction Kinetics of Primary Rock-Forming Minerals under Ambient Conditions. *Treatise on geochemistry* **2003**, *5*, 605.

(156) Bickmore, B. R.; Nagy, K. L.; Gray, A. K.; Brinkerhoff, A. R. The Effect of Al (OH) 4- on the Dissolution Rate of Quartz. *Geochimica et Cosmochimica Acta* **2006**, *70* (2), 290–305.

(157) Wilkinson, C. J.; Doss, K.; Hahn, S. H.; Keilbart, N.; Potter, A. R.; Smith, N. J.; Dabo, I.; van Duin, A. C.; Kim, S. H.; Mauro, J. C. Topological Control of Water Reactivity on Glass Surfaces: Evidence of a Chemically Stable Intermediate Phase. *The journal of physical chemistry letters* **2019**.

(158) Stark, D. Chapter 34: Alkali-Silica Reactions in Concrete. In *Significance of Tests and Properties of Concrete and Concrete-making Materials*; Lamond, J. F., Pielert, J. H., Eds.; ASTM International: West Conshohocken, PA, 2006.

(159) Rajabipour, F.; Giannini, E.; Dunant, C.; Ideker, J. H.; Thomas, M. D. A. Alkali–Silica Reaction: Current Understanding of the Reaction Mechanisms and the Knowledge Gaps. *Cem. Concr. Res.* **2015**, *76*, 130–146. https://doi.org/10.1016/j.cemconres.2015.05.024.

(160) Poole, A. B. Introduction to Alkali-Aggregate Reaction in Concrete. In *The Alkali-Silica Reaction in Concrete*; Swamy, R. N., Ed.; Blackie and Son Ltd, 2002.

(161) Miller, R.; Bush, L. *Update of Mineral Land Classification for Portland Cement Concrete-Grade Aggregate in the Temescal Valley Production Area, Riverside County, California*; 231; California Geological Survey, 2014.

(162) McCoy, W. J.; Caldwell, A. G. New Approach to Inhibiting Alkali-Aggregate Expansion. In *Journal Proceedings*; 1951; Vol. 47, pp 693–706.

(163) Thomas, M. The Effect of Supplementary Cementing Materials on Alkali-Silica Reaction: A Review. *Cement and Concrete Research* **2011**, *41* (12), 1224–1231.

(164) Mahyar, M.; Erdoğan, S. T.; Tokyay, M. Extension of the Chemical Index Model for Estimating Alkali-Silica Reaction Mitigation Efficiency to Slags and Natural Pozzolans. *Construction and Building Materials* **2018**, *179*, 587–597.

(165) Kim, T.; Olek, J. The Effects of Lithium Ions on Chemical Sequence of Alkali-Silica Reaction. *Cement and Concrete Research* **2016**, *79*, 159–168. https://doi.org/10.1016/j.cemconres.2015.09.013.

(166) Tremblay, C.; Bérubé, M. A.; Fournier, B.; Thomas, M. D. A. Performance of Lithium-Based Products against ASR: Effect of Aggregate Type and Reactivity, and Reaction Mechanisms. In *Proceedings of the Seventh CANMET/ACI International Conference on Recent Advances in Concrete Technology (Suppl. Papers)*; 2004; pp 247–267.

(167) Tremblay, C.; Bérubé, M.-A.; Fournier, B.; Thomas, M. D.; Folliard, K. J. Effectiveness of Lithium-Based Products in Concrete Made with Canadian Natural Aggregates Susceptible to Alkali-Silica Reactivity. *ACI materials journal* **2007**, *104* (2), 195.

(168) Drimalas, T.; Ideker, J. H.; Bentivegna, A. F.; Folliard, K. J.; Fournier, B.; Thomas, M. D. The Long-Term Monitoring of Large-Scale Concrete Specimens Containing Lithium Salts to Mitigate Alkali-Silica Reaction. *Special Publication* **2012**, *289*, 1–17.

(169) Ekolu, S.; Rakgosi, G.; Hooton, D. Long-Term Mitigating Effect of Lithium Nitrate on Delayed Ettringite Formation and ASR in Concrete – Microscopic Analysis. *Materials Characterization* **2017**, *133*, 165–175. https://doi.org/10.1016/j.matchar.2017.09.025.

(170) Rea, C.; Darby, K.; Suszko, C.; McDonald, K.; Hoffman, K. *Fly Ash: Current and Future Supply*; Caltrans, 2016.

(171) Oey, T.; Timmons, J.; Stutzman, P.; Bullard, J. W.; Balonis, M.; Bauchy, M.; Sant, G. An Improved Basis for Characterizing Suitability of Fly Ash as a Cement Replacement Agent. *J Am Ceram Soc* **2017**, n/a-n/a. https://doi.org/10.1111/jace.14974.

(172) La Plante, E. C.; Oey, T.; Hsiao, Y.-H.; Perry, L.; Bullard, J. W.; Sant, G. N. Enhancing Silicate Dissolution Kinetics in Hyperalkaline Environments. *The Journal of Physical Chemistry C* **2019**.

(173) Mercado-Depierre, S.; Angeli, F.; Frizon, F.; Gin, S. Antagonist Effects of Calcium on Borosilicate Glass Alteration. *Journal of Nuclear Materials* **2013**, *441* (1), 402–410.

(174) Maraghechi, H.; Rajabipour, F.; Pantano, C. G.; Burgos, W. D. Effect of Calcium on Dissolution and Precipitation Reactions of Amorphous Silica at High Alkalinity. *Cement and Concrete Research* **2016**, *87*, 1–13.

(175) Calcium Nitrate: Compound Summary. U.S. National Library of Medicine.

(176) *ASTM Standard C150/C150M-16e1. Standard Specification for Portland Cement*; ASTM International: West Conshohocken, PA, 2016.

(177) Vitro Minerals. http://www.vitrominerals.com/order-samples/c-441-test-grade/ http://www.vitrominerals.com/order-samples/c-441-test-grade/ (accessed Jan 9, 2017).

(178) *ASTM Standard C441/C441M-11. Standard Test Method for Effectiveness of Pozzolans or Ground Blast-Furnace Slag in Preventing Excessive Expansion of Concrete Due to the Alkali-Silica Reaction*; ASTM International: West Conshohocken, PA, 2011.

(179) *ASTM Standard C1260-14. Standard Test Method for Potential Alkali Reactivity of Aggregates (Mortar-Bar Method)*; ASTM International: West Conshohocken, PA, 2014.

(180) Stutzman, P. E.; Feng, P.; Bullard, J. W. Phase Analysis of Portland Cement by Combined Quantitative X-Ray Powder Diffraction and Scanning Electron Microscopy. *Journal of research of the National Institute of Standards and Technology* **2016**, *121*, 47–107.

(181) Ferraris, C.; Garboczi, E. Identifying Improved Standardized Tests for Measuring Cement Particle Size and Surface Area. *Transportation Research Record: Journal of the Transportation Research Board* **2013**, *2342* (1), 10–16. https://doi.org/10.3141/2342-02.

(182) Bullard, J. W.; Garboczi, E. J. A Model Investigation of the Influence of Particle Shape on Portland Cement Hydration. *Cement and Concrete Research* **2006**, *36* (6), 1007–1015.

(183) Fournier, M.; Ull, A.; Nicoleau, E.; Inagaki, Y.; Odorico, M.; Frugier, P.; Gin, S. Glass Dissolution Rate Measurement and Calculation Revisited. *Journal of Nuclear Materials* **2016**, *476*, 140–154.

(184) Kumar, A.; Reed, J.; Sant, G. Vertical Scanning Interferometry: A New Method to Measure the Dissolution Dynamics of Cementitious Minerals. *Journal of the American Ceramic Society* **2013**, *96* (9), 2766–2778.

(185) *ASTM Standard C305-14. Standard Practice for Mechanical Mixing of Hydraulic Cement Pastes and Mortars of Plastic Consistency*; ASTM International: West Conshohocken, PA, 2014.

(186) *ASTM C490/C490M-11e1. Standard Practice for Use of Apparatus for the Determination of Length Change of Hardened Cement Paste, Mortar, and Concrete*; ASTM International: West Conshohocken, PA, 2011.

(187) Binal, A. The Pessimum Ratio and Aggregate Size Effects on Alkali Silica Reaction. *Procedia Earth and Planetary Science* **2015**, *15*, 725–731. https://doi.org/10.1016/j.proeps.2015.08.103.

(188) Glasser, F. P. Chemistry of the Alkali-Aggregate Reaction. In *The Alkali-Silica Reaction in Concrete*; Swamy, R. N., Ed.; Blackie and Son Ltd, 2002.

(189) Ahn, D. J.; Berman, A.; Charych, D. Probing the Dynamics of Template-Directed Calcite Crystallization with in Situ FTIR. *The Journal of Physical Chemistry* **1996**, *100* (30), 12455–12461.

(190) Yu, P.; Kirkpatrick, R. J.; Poe, B.; McMillan, P. F.; Cong, X. Structure of Calcium Silicate Hydrate (C-S-H): Near-, Mid-, and Far-Infrared Spectroscopy. *Journal of the American Ceramic Society* **1999**, *82* (3), 742–748.

(191) Spinner, S. A. M. Elastic Moduli of Glasses at Elevated Temperatures by a Dynamic Method. *Journal of the American Ceramic Society* **1956**, *39* (3), 113–118.

(192) McSkimin, H. J.; Andreatch Jr, P.; Thurston, R. N. L. Elastic Moduli of Quartz versus Hydrostatic Pressure at 25 And- 195.8 C. *Journal of Applied Physics* **1965**, *36* (5), 1624–1632.

(193) Oey, T.; Stoian, J.; Li, J.; Vong, C.; Balonis, M.; Kumar, A.; Franke, W.; Sant, G. Comparison of Ca (NO 3) 2 and CaCl 2 Admixtures on Reaction, Setting, and Strength Evolutions in Plain and Blended Cementing Formulations. *Journal of Materials in Civil Engineering* **2014**, *27* (10), 04014267.

(194) Brantley, S. L.; Kubicki, J. D.; White, A. F. *Kinetics of Water-Rock Interaction*; Springer, 2008; Vol. 168.

(195) Lüttge, A. Crystal Dissolution Kinetics and Gibbs Free Energy. *J. Electron. Spectrosc. Relat. Phenom.* **2006**, *150* (2–3), 248–259. https://doi.org/10.1016/j.elspec.2005.06.007.

(196) Arvidson, R. S.; Luttge, A. Mineral Dissolution Kinetics as a Function of Distance From Equilibrium – New Experimental Results. *Chem. Geol.* **2010**, *269* (1–2), 79–88. https://doi.org/10.1016/j.chemgeo.2009.06.009.

(197) Brantley, S. L. Reaction Kinetics of Primary Rock-Forming Minerals under Ambient Conditions. *Treatise on geochemistry* **2003**, *5*, 605.

(198) Cailleteau, C.; Angeli, F.; Devreux, F.; Gin, S.; Jestin, J.; Jollivet, P.; Spalla, O. Insight into Silicate-Glass Corrosion Mechanisms. *Nature materials* **2008**, *7* (12), 978–983.

(199) Hellmann, R.; Wirth, R.; Daval, D.; Barnes, J.-P.; Penisson, J.-M.; Tisserand, D.; Epicier, T.; Florin, B.; Hervig, R. L. Unifying Natural and Laboratory Chemical Weathering with Interfacial Dissolution–Reprecipitation: A Study Based on the Nanometer-Scale Chemistry of Fluid–Silicate Interfaces. *Chemical Geology* **2012**, *294*, 203–216.

(200) Lothenbach, B.; Winnefeld, F.; Alder, C.; Wieland, E.; Lunk, P. Effect of Temperature on the Pore Solution, Microstructure and Hydration Products of Portland Cement Pastes. *Cement and Concrete Research* **2007**, *37* (4), 483–491.

(201) Wesolowski, D. J. Aluminum Speciation and Equilibria in Aqueous Solution: I. The Solubility of Gibbsite in the System Na-K-Cl-OH-Al (OH) 4 from 0 to 100 C. *Geochimica et Cosmochimica Acta* **1992**, *56* (3), 1065–1091.

(202) Rothstein, D.; Thomas, J. J.; Christensen, B. J.; Jennings, H. M. Solubility Behavior of Ca-, S-, Al-, and Si-Bearing Solid Phases in Portland Cement Pore Solutions as a Function of Hydration Time. *Cement and Concrete Research* **2002**, *32* (10), 1663–1671.

(203) Sandberg, P. J.; Roberts, L. R. Cement-Admixture Interactions Related to Aluminate Control. *Journal of ASTM International* **2005**, *2* (6), 1–14.

(204) Icenhower, J. P.; McGrail, B. P.; Shaw, W. J.; Pierce, E. M.; Nachimuthu, P.; Shuh, D. K.; Rodriguez, E. A.; Steele, J. L. Experimentally Determined Dissolution Kinetics of Na-Rich Borosilicate Glass at Far From Equilibrium Conditions: Implications for Transition

State Theory. *Geochim. Cosmochim. Acta* **2008**, *72* (12), 2767–2788. https://doi.org/10.1016/j.gca.2008.02.026.

(205) Icenhower, J. P.; Steefel, C. I. Experimentally Determined Dissolution Kinetics of SON68 Glass at 90 °C Over a Silica Saturation Interval: Evidence Against a Linear Rate Law. *J. Nucl. Mater.* **2013**, *439* (1–3), 137–147. https://doi.org/10.1016/j.jnucmat.2013.04.008.

(206) Diamond, S. A Review of Alkali-Silica Reaction and Expansion Mechanisms 1. Alkalies in Cements and in Concrete Pore Solutions. *Cem. Concr. Res.* **1975**, *5* (4), 329–345.

(207) Chappex, T.; Scrivener, K. L. The Effect of Aluminum in Solution on the Dissolution of Amorphous Silica and Its Relation to Cementitious Systems. *J. Am. Ceram. Soc.* **2013**, *96* (2), 592–597. https://doi.org/10.1111/jace.12098.

(208) Houston, J. R.; Herberg, J. L.; Maxwell, R. S.; Carroll, S. A. Association of Dissolved Aluminum with Silica: Connecting Molecular Structure to Surface Reactivity Using NMR. *Geochimica et Cosmochimica Acta* **2008**, *72* (14), 3326–3337.

(209) Mason, H. E.; Maxwell, R. S.; Carroll, S. A. The Formation of Metastable Aluminosilicates in the Al–Si–H2O System: Results from Solution Chemistry and Solid-State NMR Spectroscopy. *Geochimica et Cosmochimica Acta* **2011**, *75* (20), 6080–6093.

(210) Angeli, F.; Boscarino, D.; Gin, S.; Mea, G. D.; Boizot, B.; Petit, J. C. Influence of Calcium on Sodium Aluminosilicate Glass Leaching Behaviour. *Physics and chemistry of glasses* **2001**, *42* (4–5), 279–286.

(211) Parkhurst, D. L.; Appelo, C. A. J. *Description of Input and Examples for PHREEQC Version 3: A Computer Program for Speciation, Batch-Reaction, One-Dimensional Transport, and Inverse Geochemical Calculations*; US Geological Survey, 2013.

(212) Charlton, S. R.; Parkhurst, D. L. Modules Based on the Geochemical Model PHREEQC for Use in Scripting and Programming Languages. *Computers & Geosciences* **2011**, *37* (10), 1653–1663.

(213) Http://Gems.Web.Psi.Ch/, Last Verified, August 25, 2016.

(214) Kulik, D. A.; Wagner, T.; Dmytrieva, S. V.; Kosakowski, G.; Hingerl, F. F.; Chudnenko, K. V.; Berner, U. R. GEM-Selektor Geochemical Modeling Package: Revised Algorithm

and GEMS3K Numerical Kernel for Coupled Simulation Codes. *Computational Geosciences* **2013**, *17* (1), 1–24.

(215) Wagner, T.; Kulik, D. A.; Hingerl, F. F.; Dmytrieva, S. V. GEM-Selektor Geochemical Modeling Package: TSolMod Library and Data Interface for Multicomponent Phase Models. *The Canadian Mineralogist* **2012**, *50* (5), 1173–1195.

(216) Dove, P. M. The Dissolution Kinetics of Quartz in Aqueous Mixed Cation Solutions. *Geochimica et Cosmochimica Acta* **1999**, *63* (22), 3715–3727.

(217) Pignatelli, I.; Kumar, A.; Bauchy, M.; Sant, G. Topological Control on Silicates' Dissolution Kinetics. *Langmuir* **2016**, *32* (18), 4434–4439.

(218) Oey, T.; Kumar, A.; Pignatelli, I.; Yu, Y.; Neithalath, N.; Bullard, J. W.; Bauchy, M.; Sant, G. Topological Controls on the Dissolution Kinetics of Glassy Aluminosilicates. *Journal of the American Ceramic Society* **2017**.

(219) Zapol, P.; He, H.; Kwon, K. D.; Criscenti, L. J. First-Principles Study of Hydrolysis Reaction Barriers in a Sodium Borosilicate Glass. *International Journal of Applied Glass Science* **2013**, *4* (4), 395–407.

(220) Jantzen, C. M.; Brown, K. G.; Pickett, J. B. Durable Glass for Thousands of Years. *International Journal of Applied Glass Science* **2010**, *1* (1), 38–62.

(221) Bauchy, M. Deciphering the Atomic Genome of Glasses by Topological Constraint Theory and Molecular Dynamics: A Review. *Computational Materials Science* **2019**, *159*, 95–102.

(222) Bullard, J. W.; Jennings, H. M.; Livingston, R. A.; Nonat, A.; Scherer, G. W.; Schweitzer, J. S.; Scrivener, K. L.; Thomas, J. J. Mechanisms of Cement Hydration. *Cement and Concrete Research* **2011**, *41* (12), 1208–1223.

(223) Yeh, I.-C. Modeling of Strength of High-Performance Concrete Using Artificial Neural Networks. *Cement and Concrete research* **1998**, *28* (12), 1797–1808.

(224) Chou, J.-S.; Chiu, C.-K.; Farfoura, M.; Al-Taharwa, I. Optimizing the Prediction Accuracy of Concrete Compressive Strength Based on a Comparison of Data-Mining Techniques. *Journal of Computing in Civil Engineering* **2010**, *25* (3), 242–253.

(225) Akande, K. O.; Owolabi, T. O.; Twaha, S.; Olatunji, S. O. Performance Comparison of SVM and ANN in Predicting Compressive Strength of Concrete. *IOSR Journal of Computer Engineering* **2014**, *16* (5), 88–94.

(226) Zarandi, M. F.; Türksen, I. B.; Sobhani, J.; Ramezanianpour, A. A. Fuzzy Polynomial Neural Networks for Approximation of the Compressive Strength of Concrete. *Applied Soft Computing* **2008**, *8* (1), 488–498.

(227) Atici, U. Prediction of the Strength of Mineral Admixture Concrete Using Multivariable Regression Analysis and an Artificial Neural Network. *Expert Systems with applications* **2011**, *38* (8), 9609–9618.

(228) Kasperkiewicz, J.; Racz, J.; Dubrawski, A. HPC Strength Prediction Using Artificial Neural Network. *Journal of Computing in Civil Engineering* **1995**, *9* (4), 279–284.

(229) Ni, H.-G.; Wang, J.-Z. Prediction of Compressive Strength of Concrete by Neural Networks. *Cement and Concrete Research* **2000**, *30* (8), 1245–1250.

(230) Öztaş, A.; Pala, M.; Özbay, E.; Kanca, E.; Caglar, N.; Bhatti, M. A. Predicting the Compressive Strength and Slump of High Strength Concrete Using Neural Network. *Construction and building materials* **2006**, *20* (9), 769–775.

(231) Rafiei, M. H.; Khushefati, W. H.; Demirboga, R.; Adeli, H. Supervised Deep Restricted Boltzmann Machine for Estimation of Concrete. *ACI Materials Journal* **2017**, *114* (2).

(232) Topcu, I. B.; Sarıdemir, M. Prediction of Compressive Strength of Concrete Containing Fly Ash Using Artificial Neural Networks and Fuzzy Logic. *Computational Materials Science* **2008**, *41* (3), 305–311.

(233) John Lu, Z. Q. The Elements of Statistical Learning: Data Mining, Inference, and Prediction. *Journal of the Royal Statistical Society: Series A (Statistics in Society)* **2010**, *173* (3), 693–694.

(234) Breiman, L. Bagging Predictors. *Machine learning* **1996**, *24* (2), 123–140.

(235) Geurts, P.; Ernst, D.; Wehenkel, L. Extremely Randomized Trees. *Machine learning* **2006**, *63* (1), 3–42.

(236) Pedregosa, F.; Varoquaux, G.; Gramfort, A.; Michel, V.; Thirion, B.; Grisel, O.; Blondel, M.; Prettenhofer, P.; Weiss, R.; Dubourg, V. Scikit-Learn: Machine Learning in Python. *Journal of machine learning research* **2011**, *12* (Oct), 2825–2830.

(237) Fix, E.; Hodges Jr, J. L. *Discriminatory Analysis-Nonparametric Discrimination: Consistency Properties*; California Univ Berkeley, 1951.

(238) Cover, T. Estimation by the Nearest Neighbor Rule. *IEEE Transactions on Information Theory* **1968**, *14* (1), 50–55.

(239) ASTM International. Annual Book of ASTM Standards. 2012.

(240) Irwin, J. O. On a Criterion for the Rejection of Outlying Observations. *Biometrika* **1925**, 238–250.

(241) McLachlan, G.; Do, K.-A.; Ambroise, C. *Analyzing Microarray Gene Expression Data*; John Wiley & Sons, 2005; Vol. 422.

(242) Brownlee, J. Machine Learning Mastery with Python. *Machine Learning Mastery Pty Ltd* **2016**, 100–120.

(243) Krawczyk, B. Learning from Imbalanced Data: Open Challenges and Future Directions. *Progress in Artificial Intelligence* **2016**, *5* (4), 221–232.

(244) Torgo, L.; Branco, P.; Ribeiro, R. P.; Pfahringer, B. Resampling Strategies for Regression. *Expert Systems* **2015**, *32* (3), 465–476.

(245) Garg, N.; Skibsted, J. Dissolution Kinetics of Calcined Kaolinite and Montmorillonite in Alkaline Conditions: Evidence for Reactive Al (V) Sites. *Journal of the American Ceramic Society*.